D I S S E R T A T I O N

# Electron Dynamics in Finite Quantum Systems

Christopher R. McDonald

Thesis submitted to the
Faculty of Graduate and Postdoctoral Studies
in partial fulfillment of the requirements
for a doctoral degree in Physics

Department of Physics
Faculty of Science
University of Ottawa

© Christopher R. McDonald, Ottawa, Canada, 2013

**DISSERTATION**

# Electron Dynamics in Finite Quantum Systems

**Christopher R. McDonald**

**Abstract.**

The multiconfiguration time-dependent Hartree-Fock (MCTDHF) and multiconfiguration time-dependent Hartree (MCTDH) methods are employed to investigate nonperturbative multielectron dynamics in finite quantum systems. MCTDHF is a powerful tool that allows for the investigation of multielectron dynamics in strongly perturbed quantum systems. We have developed an MCTDHF code that is capable of treating problems involving three dimensional (3D) atoms and molecules exposed to strong laser fields. This code will allow for the theoretical treatment of multielectron phenomena in attosecond science that were previously inaccessible. These problems include complex ionization processes in pump-probe experiments on noble gas atoms, the nonlinear effects that have been observed in Ne atoms in the presence of an x-ray free-electron laser (XFEL) and the molecular rearrangement of cations after ionization. An implementation of MCTDH that is optimized for two electrons, each moving in two dimensions (2D), is also presented. This implementation of MCTDH allows for the efficient treatment of 2D spin-free systems involving two electrons; however, it does not scale well to 3D or to systems containing more that two electrons.

Both MCTDHF and MCTDH were used to treat 2D problems in nanophysics and attosecond science. MCTDHF is used to investigate plasmon dynamics and the quantum breathing mode for several electrons in finite lateral quantum dots. MCTDHF is also used to study the effects of manipulating the potential of a double lateral quantum dot containing two electrons; applications to quantum computing are discussed. MCTDH is used to examine a diatomic model molecular system exposed to a strong laser field; nonsequential double ionization and high harmonic generation are studied and new processes identified and explained. An implementation of MCTDHF is developed for nonuniform tensor product grids; this will allow for the full 3D implementation of MCTDHF and will provide a means to investigate a wide variety of problems that cannot be currently treated by any other method. Finally, the time it takes for an electron to tunnel from a bound state is investigated; a definition of the tunnel time is established and the Keldysh time is connected to the wavefunction dynamics.

# Contents

# Preface

To my wife Jamie.

I would like to thank my supervisor Thomas Brabec for his insight, guidance and support throughout this entire process. In addition, thank you to Carlos Destefani, Suren Sukiasyan, Cole Van Vlack, Gianfranco Orlando and Charles Varin; it has been a pleasure to work alongside all of you. I would also like to thank my family for all of their support. Finally, thank you to my faithful canine companion who always kept me company throughout the late nights that I spent writing this thesis.

This document consists of several papers to which I have contributed from 2008 to the present. Chapters 1, 8 and 10 were written entirely by me; chapters $2-7$ and 9 were written with co-authors. Here, I will detail my contributions and the contributions of my co-authors. For each publication, I will give the citation (or the journal name that it is currently submitted to) followed by the list of authors. I will then state the contributions of each author using their initials — this includes my own contributions as well.

Chapter 2 has been published in *Phys. Rev. B* 78, 165331 (2008) by the authors Carlos F. Destefani, Chris McDonald, Ramin M. Abolfath, Pawel Hawrylak and Thomas Brabec. CM developed the computational approach and the necessary software (MCTDHF and TDCI) to perform the time-dependent calculations. CFD performed the calculations and prepared the figures. All authors contributed to the analysis and preparation of the manuscript.

Chapter 3 has been published in *Phys. Rev. B* 79, 155372 (2009) by the authors Carlos F. Destefani, Chris McDonald, Suren Sukiasyan and Thomas Brabec. CM developed the computational approach and the necessary software (MCTDHF) to perform the time-dependent calculations. CFD performed the calculations and prepared the figures. All authors contributed to the analysis and preparation of the manuscript.

Chapter 4 has been published in *Phys. Rev. B* 81, 045314 (2010) by the authors Carlos F. Destefani, Chris McDonald, Suren Sukiasyan and Thomas Brabec. For this publication I developed the tools to perform the four electron calculations. Calculations were performed by CFD and CM; the figures were prepared by CFD. The damped harmonic oscillator model was developed by TB, CFD and CM. All authors contributed to the analysis and preparation of the manuscript. CM and CFD both contributed equally to this publication.

Chapter 5 has been submitted to *Phys. Rev. Lett.* under the authors C. R. McDonald, G. Orlando, J. W. Abraham, D. Hochstul, M. Bonitz and T. Brabec. CRM performed the calculations and prepared the figures. The analytical expressions were derived by CRM, GO and TB. All authors contributed to the preparation of the manuscript.

Chapter 6 has been published in *Phys. Rev. A* 80, 013412 (2009) by the authors Suren Sukiasyan, Chris McDonald, Cole Van Vlack, Carlos Destefani, Thomas Fennel, Misha Ivanov,

and Thomas Brabec. Determination of the system parameters and preliminary calculations were performed by CM. The filtering method developed and the initial observation of the structures in the momentum space two-body density were done by CM. SS performed the MCTDH calculations and the figures were prepared by SS, TB and CV. The complex scaling calculations were performed by CV. The semi-classical model was developed by TB, CM and SS. All authors contributed to the analysis and preparation of the manuscript. Both SS and CM contributed equally to this publication.

Chapter 7 has been published in *Phys. Rev. Lett.* 102, 223002 (2009) by the authors Suren Sukiasyan, Chris McDonald, Carlos Destefani, Misha Yu. Ivanov, and Thomas Brabec. The exploratory work and identification of the system parameters was done by CM. SS performed the MCTDH calculations and prepared the figures. TB, MYI, and SS developed the method of ionic eigenstate resolved wavefunctions. All authors contributed to the analysis and preparation of the manuscript.

Chapter 9 has been published in *Phys. Rev. Lett.* 111, 090405 (2013) by the authors C. R. McDonald, G. Orlando, G. Vampa and T. Brabec. CRM performed the calculations and prepared the figures. CRM, TB and GO developed the analytical theory. All authors contributed to the preparation of the manuscript.

# List of publications

(i) Carlos F. Destefani, Chris McDonald, Ramin M. Abolfath, Pawel Hawrylak and Thomas Brabec, "*Ab initio* approach to the optimization of qubit manipulation", Phys. Rev. B **78**, 165331 (2008).

(ii) Carlos F. Destefani, Chris McDonald, Suren Sukiasyan and Thomas Brabec, "Controlling matrix elements and relaxation in a two-electron double quantum dot", Phys. Rev. B **79**, 155322 (2009).

(iii) Suren Sukiasyan, Chris McDonald, Cole Van Vlack, Carlos Destefani, Thomas Fennel, Misha Ivanov, and Thomas Brabec, "Signatures of bound-state-assisted nonsequential double ionization", Phys. Rev. A **80**, 013412 (2009).

(iv) Suren Sukiasyan, Chris McDonald, Carlos Destefani, Misha Yu. Ivanov, and Thomas Brabec, "Multielectron correlation in high-harmonic generation: A 2D analysis", Phys. Rev. Lett. **102**, 223002 (2009).

(v) Suren Sukiasyan, Chris McDonald, Cole Van Vlack, Carlos Destefani, Charles Varin, Misha Ivanov, and Thomas Brabec, "Correlated few-electron dynamics in intense laser fields", Chem. Phys. **366**, 37 (2009).

(vi) Carlos F. Destefani, Chris McDonald, Suren Sukiasyan and Thomas Brabec, "Plasmon dynamics in strongly driven finite few-electron quantum systems: The role of the surface", Phys. Rev. B **81**, 045314 (2010).

(vii) C. R. McDonald, G. Orlando, J. W. Abraham, D. Hochstul, M. Bonitz and T. Brabec, "Theory and characterization of the quantum breathing mode", Phys. Rev. Lett. (submitted).

(viii) C. R. McDonald, G. Orlando, G. Vampa and T. Brabec, "Tunnel ionization dynamics of bound systems in laser fields: How long does it take for a bound electron to tunnel?", Phys. Rev. Lett. **111**, 090405 (2013).

# Chapter 1

# Introduction

The past few decades have seen rapid development in two particular areas — nanoscience and attosecond science. Finite few-body quantum systems are pervasive in both of these areas. However, a theoretical treatment of the dynamics of these systems is extremely difficult.

In nanoscience quantum dots (artificial atoms) are extremely important. These artifical atoms possess properties that are similar to real atoms and molecules. However, quantum dots (QDs) can be created in a laboratory environment and their electronic properties manipulated. This allows for the effects of electron-electron interactions to be observed. Quantum dots are important in quantum computing as they have the potential to lead to a viable realization of qubits [1,2]. Furthermore, they are used in nanotechnology to create some of the smallest switches and transistors [3, 4]. As electronic devices get smaller they begin to behave more like finite quantum systems [5]; the motion of the electrons within these device becomes important [6]. While there has been much theoretical investigation into the time-independent properties of these finite quantum systems (see Ref. [7] and references therein), very little has been done to address their dynamics.

In attosecond science, significant advances in experimental techniques involving atoms and molecules exposed to strong laser fields have been made over that past decade. The development of molecular tomography and dynamic imaging techniques have made it possible to gain insight about the processes that atoms and molecules undergo during chemical reactions. This has generated a wealth of experimental observation as to the time-dependent behaviour of atoms and molecules exposed to strong-field laser fields [8–21]. Multielectron excitation and relaxation processes in noble gas atoms have been observed with subfemtosecond resolution. More recently, x-ray free-electron laser (XFEL) experiments have shown nonlinear atomic responses in neon atoms [20]. In molecules, it was observed that the structural rearrangement of the cation occurs within a few femtoseconds after ionization [14]. In addition, femtosecond time resolution observations of chemical reactions have been performed [19]. Further, correlated electron spectra seem to indicate complex ionization processes and have shown a molecular alignment dependence in the ionization yield [13]. To understand these phenomena, new theoretical tools are needed.

Solution of the time-dependent Schrödinger equation (TDSE) for multi-electron systems has been limited to the single active electron (SAE) approximation or to systems involving only two electrons such as He [22–25] and $H_2$ [26–31]. The methods employed in these calculations either do not take proper account of correlation (time-dependent Hartree-Fock) or are not viable for more than two electrons (full-dimensional solution of the TDSE, time-dependent configuration interaction). Thus, more advanced methods and tools are needed to analyse and understand the processes that have been observed.

In order to make progress toward solving the above problems we have developed a multiconfiguration time-dependent Hartree-Fock (MCTDHF) code that is capable of performing calculations on multielectron systems in $1-3$D. MCTDHF, as described below (see Sec. 1.1.4), provides an efficient way of representing the multielectron wavefunction and this code will provide a powerful tool that can be used towards making significant advances in the theory surrounding atoms and molecules in strong laser fields. The remainder of this chapter is dedicated to providing an introduction to the numerical methods that will be employed in subsequent chapters. This chapter concludes with a brief outline.

## 1.1 Numerical integration of the time-dependent Schrödinger equation

Here the numerical solution of the TDSE

$$i\hbar\frac{\partial\Psi}{\partial t} = H\Psi, \tag{1.1}$$

is considered. The n-electron Hamiltonian, in SI units and Born-Oppenheimer approximation, is given by,

$$H = \sum_{i=1}^{n}\left\{\frac{1}{2m}\left(\frac{\hbar}{i}\nabla + e\boldsymbol{A}(\mathbf{r}_i,\, t)\right)^2 + U(\mathbf{r}_i,\, t) - e\chi(\mathbf{r}_i,\, t)\right\} + \frac{1}{4\pi\epsilon_0}\sum_{i<j}^{n}\frac{e^2}{|\mathbf{r}_i - \mathbf{r}_j|} \tag{1.2}$$

where $m$ is the mass of the electron, $e$ is the elementary charge, $\epsilon_0$ is the permittivity of free space and $U(\mathbf{r},\, t)$ is the binding potential. An explicit time dependence is included in $U(\mathbf{r},\, t)$ to allow for the manipulation of the trap — as is common in many nanophysics applications. Finally, $\boldsymbol{A}(\mathbf{r},\, t)$ and $\chi(\mathbf{r},\, t)$ are the vector and scalar potentials respectively of an external field; their relation to the electric field $\boldsymbol{E}(\mathbf{r},\, t)$ and magnetic field $\boldsymbol{B}(\mathbf{r},\, t)$ are given by

$$\mathbf{E}(\mathbf{r};\, t) = -\nabla\chi(\mathbf{r};\, t) - \frac{\partial}{\partial t}\mathbf{A}(\mathbf{r};\, t) \tag{1.3}$$

$$\mathbf{B}(\mathbf{r};\, t) = \nabla\times\mathbf{A}(\mathbf{r};\, t). \tag{1.4}$$

The TDSE in Eq. 1.1 is invariant under the quantum gauge transformation

$$\begin{cases}\mathbf{A}(\mathbf{r};\, t) \longrightarrow \mathbf{A}(\mathbf{r};\, t) + \nabla\phi(\mathbf{r};\, t)\\ \chi(\mathbf{r};\, t) \longrightarrow \chi(\mathbf{r};\, t) - \dfrac{\partial}{\partial t}\phi(\mathbf{r};\, t)\\ \Psi(\mathbf{r};\, t) \longrightarrow \exp\left[-i\dfrac{e}{\hbar}\phi(\mathbf{r};\, t)\right]\Psi(\mathbf{r};\, t)\,.\end{cases}$$

For the problems involving external fields considered here, the calculations will be done in dipole approximation — the dimensions of the system are much smaller than the wavelength of the external field. As such, the spatial dependence of the vector and scalar potentials, and consequently the electric and magnetic fields, is dropped so that they are now purely time-dependent. Further, $\mathbf{B}(t) = 0$ as problems involving magnetic fields are also not considered. For problems involving external fields there are two common gauges used: (i) length gauge and (ii) velocity gauge. In the length gauge $\mathbf{A}(t) = 0$ and $\chi(\mathbf{r},\, t) = \mathbf{r}\cdot\boldsymbol{E}(t)$; in the velocity gauge $\chi(\mathbf{r},\, t) = 0$.

For practical computational purposes the Hamiltonian in Eq. 1.2, presented in SI units, is not ideal. As such, in all computations, atomic units (a.u. or at.u.) are used. One exception

is chapter 5 where a unit system specific to a harmonic trap is presented. In the atomic unit system, units of length are given by the Bohr radius,

$$a_0 = \frac{4\pi\epsilon_0\hbar^2}{me^2}, \tag{1.6}$$

units of energy by the Hartree energy,

$$E_h = \frac{me^4}{(4\pi\epsilon_0\hbar)^2} \tag{1.7}$$

and units of time given by $\hbar/E_h$. In this unit system, the Hamiltonian in Eq. 1.2, presented in dipole approximation and length gauge, becomes,

$$H_{\text{lg}} = \sum_{i=1}^{n}\left\{-\frac{1}{2}\nabla^2 + U(\mathbf{r}_i,\, t) - \mathbf{r}_i\cdot\boldsymbol{E}(t)\right\} + \sum_{i<j}^{n}\frac{1}{|\mathbf{r}_i - \mathbf{r}_j|} \tag{1.8}$$

and in dipole approximation and velocity gauge it is

$$H_{\text{vg}} = \sum_{i=1}^{n}\left\{\frac{1}{2}\left(\frac{1}{i}\nabla + \boldsymbol{A}(\mathbf{r}_i)\right)^2 + U(\mathbf{r}_i,\, t)\right\} + \sum_{i<j}^{n}\frac{1}{|\mathbf{r}_i - \mathbf{r}_j|}. \tag{1.9}$$

Unless otherwise specified, atomic units are used throughout.

A solution of the TDSE is easily accessible for most systems containing a single electron. When more than one electron is involved the solution is not so straightforward. First consider a single He atom where each electron is able to move in the three spatial dimensions; the wavefunction is then a 6D function. If we wished to represent the wavefunction on a grid using 100 points for each grid axis, the wavefunction would have $10^{12}$ points. This already stretches the limits of the most powerful supercomputers available. Fortunately, in the case of He a coordinate system can be found that reduces the dimension of the problem and makes the calculation tractable. Now consider Ne, the next noble gas in the periodic table. Unlike He, a convenient coordinate transformation does not exist to simplify the problem. Suppose we wish to be more conservative with the number of points we use and choose 10 points per dimension to model Ne. Then the resulting wavefunction will require $10^{30}$ points to represent the full wavefunction. The amount of memory alone required to store the wavefunction would be $1.6 \times 10^{19}$ TB. Thus, in order to make this problem tractable, approximate methods need to be used. The sections that follow will introduce methods that are used to solve that TDSE and discuss the strengths and weaknesses of each.

### 1.1.1 Split-operator method

The split-operator (SPO) method is a straightforward and easily implemented way of solving the TDSE. Consider a Hamiltonian $\hat{H} = \hat{T} + \hat{V}$ where $\hat{T}$ is diagonal in the momentum space and $\hat{V}$ is diagonal in coordinate space. Let $\hat{U}$ be the unitary operator for a time-step $\Delta t$; this is given by

$$\hat{U} = \mathrm{e}^{-i\hat{H}\Delta t}. \tag{1.10}$$

The SPO method splits the operator $\hat{U}$ into a product of exponential operators whose arguments are diagonal. In order to achieve this the Baker-Campbell-Hausdorff (BCH) theorem [32]

$$\mathrm{e}^{\hat{A}}\mathrm{e}^{\hat{B}} = \exp\left(\hat{A} + \hat{B} + \frac{1}{2}[\hat{A},\, \hat{B}] + \frac{1}{12}([\hat{A},\, [\hat{A},\, \hat{B}]] - [\hat{B},\, [\hat{A},\, \hat{B}]]) + \ldots\right) \tag{1.11}$$

is required. Simple application of the BCH theorem to 1.10 will yield the expression

$$\hat{U} = \mathrm{e}^{-i\hat{T}\Delta t}\mathrm{e}^{-i\hat{V}\Delta t} + \mathcal{O}(\Delta t^2) \tag{1.12}$$

which is correct to first order in $\Delta t$. Generally this first order expression is not good enough and thus a higher order expression is required. By applying the BCH theorem twice it is possible to obtain the second order expression

$$\hat{U} = \mathrm{e}^{-i\hat{T}\Delta t/2}\mathrm{e}^{-i\hat{V}\Delta t}\mathrm{e}^{-i\hat{T}\Delta t/2} + \mathcal{O}(\Delta t^3). \tag{1.13}$$

Eq. 1.13 is the most commonly used SPO method; it provides a good balance between numerical accuracy and computational work load. While it is possible to derive higher order expressions for $\hat{U}$, these forms are generally not desired due to the computational effort required to implement them.

The second order SPO expression is used in Chap. 2 to solve the TDSE for a $2 \times 2D$ system and in Chap. 6 to solve the TDSE for a $2 \times 1D$ system of interacting electrons. For larger systems — more electrons or higher dimensions — the SPO method is not feasible due to the need to represent the two-body Coulomb potential.

### 1.1.2 Time-dependent density functional theory

Density functional theory (DFT) [33] is a widely used approach for solving the time-independent Schrödinger equation; see appendix A for an introduction to DFT. Its time dependent counterpart — time-dependent density functional theory (TDDFT) — is often presented as a viable option for examining non-perturbative multielectron dynamics. While (TD)DFT calculations are not performed here, a brief introduction to the theory and a discussion of some the challenges that face TDDFT will be given in this section.

For time-dependent problems DFT has been extended to TDDFT by the Runge-Gross (RG) theorem. The RG theorem is analogous to the Hohenberg-Kohn (HK) theorem [33] of DFT and states:

**Theorem 1.1.1** (Runge-Gross Theorem)**.** *For every single-particle potential $U(\mathbf{r}, t)$ which can be expanded into a Taylor series in the neighbourhood of $t = t_0$ an invertible map $G : U(\mathbf{r}, t) \to \rho(\mathbf{r}, t)$ is defined by solving the TDSE with a fixed initial state and calculating the corresponding density.*

The original statement of Theorem 1.1.1 and its subsequent proof is given in reference [34]. The RG theorem also holds for piecewise analytical potentials and is a special case of a more general theory [35].

In TDDFT the action integral, can be written as a functional of the density,

$$A[\rho] = F[\rho] - \int_{t_0}^{t_1} dt \int d\mathbf{r}\, U(\mathbf{r};\, t)\rho(\mathbf{r},\, t) \tag{1.14}$$

where $F[\rho]$ is the universal functional of the density defined by,

$$F[\rho] = \int_{t_0}^{t_1} dt \left\langle \Psi(t) \right| i\frac{\partial}{\partial t} - T - V \left| \Psi(t) \right\rangle . \tag{1.15}$$

The exact density of the system is found when $\rho$ satisfies

$$\frac{\delta A}{\delta \rho} = 0 \tag{1.16}$$

that is, at the stationary point of $A[\rho]$. The density can then be computed by solving a set of single-particle time-dependent Schrödinger equations moving in a time-dependent effective potential,

$$i\frac{\partial}{\partial t}\varphi_i(\mathbf{r},\,t) = \left[-\frac{1}{2}\nabla^2 + U_{\text{eff}}(\mathbf{r},\,t)\right]\varphi_i(\mathbf{r},\,t) \tag{1.17}$$

where $i$ runs from 1 to the number of electrons. The time dependent effective potential $U_{\text{eff}}$ is given by

$$U_{\text{eff}}(\mathbf{r},\,t) = U(\mathbf{r},\,t) + \int \frac{\rho(\mathbf{r}',\,t)}{|\mathbf{r}-\mathbf{r}'|}d\mathbf{r}' + U_{\text{xc}}(\mathbf{r},\,t) \tag{1.18}$$

where $U_{\text{xc}}$ is the exchange-correlation potential. $U_{\text{xc}}$ is a functional of $\rho$ and takes account of exchange and correlation effects. The exact density of the system can then be computed from

$$\rho(\mathbf{r},\,t) = \sum_i |\varphi_i(\mathbf{r},\,t)|^2 . \tag{1.19}$$

A significant disadvantage to (TD)DFT is the difficulty associated with the determination of the exchange-correlation functional. Proposed methods to construct $U_{\text{xc}}$ [36, 37] are extremely complicated and it is difficult to gauge their accuracy. So far, exact exchange-correlation terms have only been calculated for a specific two-electron system [38]. Another difficulty with (TD)DFT is that it provides only the density of the system and not the quantum mechanical wavefunction. As well, TDDFT has encountered many other problems [39–41]. One of these [41] being a fundamental flaw in which the entire history of the density enters in the exchange-correlation term; this can cause ambiguities when representing excited states.

### 1.1.3 The time-dependent Hartree-Fock and configuration interaction methods

The most straightforward approach to solving the $f$-electron TDSE is the time-dependent Hartree-Fock (TDHF) method [22]. In TDHF the wavefunction is represented by a single Slater determinant made up of a set of $f$ single-particle spin-orbitals $\varphi_i$; that is,

$$\Psi(\mathbf{q}_1,\ldots,\mathbf{q}_f;\,t) = \sum_\pi \text{sgn}(\pi)\prod_{i=1}^{f}\varphi_{\pi(i)}(\mathbf{q}_i;\,t), \tag{1.20}$$

where $\pi$ runs through all permutations and $\text{sgn}(\pi) = 1(-1)$ for even (odd) permutations. Equations of motion are determined for the $\varphi_i$'s through the use of a variational principle. Since TDHF uses only a single Slater determinant, it is capable of solving the TDSE for large numbers of electrons. However, this single determinant approach only treats the interaction between the electrons in an average way and thus fails to take proper account of electron correlation.

In an effort to improve on the TDHF method, the time-dependent configuration interaction (TDCI) method expands the wavefunction as the sum of many Slater determinants weighted by time-dependent coefficients; that is,

$$\Psi(\mathbf{q}_1,\ldots,\mathbf{q}_f;\,t) = \sum_{J=0}^{N} A_J(t)\Phi_J(\mathbf{q}_1,\ldots,\mathbf{q}_f) \tag{1.21}$$

where J is the composite index for the set of $\{j_i\}$, $\Phi_J$ is the Slater determinant formed from all permutations of $\varphi_{j_1},\ldots,\varphi_{j_f}$, $A_J$ is the weighting coefficient for the Slater determinant J and $N$ is the number of determinants used. The larger number of determinants used allows for the

inclusion of excited configurations into the calculation. This allows, in principle, for full inclusion of electron correlation. In TDCI the time-dependence is carried by the $A_J$; the spin-orbitals remain fixed. As such, many expansion coefficients are needed to properly account for electron correlation. For $f > 3$ the number of weighting coefficients becomes extremely prohibitive and thus limits TDCI's ability to handle most time-dependent problems.

### 1.1.4 Multiconfiguration time-dependent Hartree-Fock

In this section the multiconfiguration time-dependent Hartree-Fock (MCTDHF) method [42] is described in general; details about specific implementations will be given in the relevant chapters. MCTDHF expands the $f$-electron wavefunction $\Psi(\mathbf{q}_1, \ldots, \mathbf{q}_f; t)$ on a set of $n$ time-dependent spin-orbitals $\varphi_i(\mathbf{q}; t)$ and a set of time-dependent linear expansion coefficients $A_{j_1 \ldots j_f}(t)$ as

$$\Psi(\mathbf{q}_1, \ldots, \mathbf{q}_f; t) = \sum_{j_1=1}^{n} \cdots \sum_{j_f=1}^{n} A_{j_1 \ldots j_f}(t) \varphi_{j_1}(\mathbf{q}_1; t) \cdots \varphi_{j_f}(\mathbf{q}_f; t), \tag{1.22}$$

where $\mathbf{q}_i$ represents both the spatial and spin coordinate of the $i^{th}$ electron. The anti-symmetry of the wavefunction is preserved by requiring the expansion coefficients to be anti-symmetric under exchange of any two indicies; that is,

$$A_{j_1 \ldots j_k \ldots j_l \ldots j_f} = -A_{j_1 \ldots j_l \ldots j_k \ldots j_f}. \tag{1.23}$$

This reduces the number of independent expansion coefficients to $\binom{n}{f}$. The ansatz in Eq. 1.22 is invariant under transformations of the form

$$A_{j_1 \ldots j_f} \to \tilde{A}_{j_1 \ldots j_f} = \sum_{k_1=1}^{n} \cdots \sum_{k_f=1}^{n} B^{-1}_{j_1 k_1} \cdots B^{-1}_{j_1 k_1} A_{k_1 \ldots k_f} \tag{1.24}$$

$$\varphi_j \to \tilde{\varphi_j} = \sum_{k=1}^{n} B_{jk} \varphi_k, \tag{1.25}$$

where $B$ is any invertible $n \times n$ matrix. In order to restrict $B$ and ensure orthornormality of the spin-orbital functions, the following constrains are used:

$$\langle \varphi_j | \varphi_k \rangle = \delta_{jk} \tag{1.26}$$

$$i \langle \varphi_j | \dot{\varphi}_k \rangle = g_{jk} \tag{1.27}$$

where $\boldsymbol{g}$ is an arbitrary (possibly time-dependent), single particle, Hermitian operator with matrix elements $g_{ij} = \langle \varphi_i | \, g(t) \, | \varphi_j \rangle$.

Equations of motion for the $A$'s and $\varphi$'s are determined from the Dirac-Frenkel variational principle [43]

$$\langle \delta\Psi | \, i \frac{\partial}{\partial t} - H \, | \Psi \rangle = 0 \tag{1.28}$$

where $\delta\Psi$ is an element of the tangent space $T_\Psi \mathcal{M}$ of the manifold $\mathcal{M}$ in which $\Psi$ is contained. At each time the residual $(i\partial_t - H) \, |\Psi\rangle$ is orthogonal to $T_\Psi \mathcal{M}$, thus ensuring that, within the ansatz, $i\dot{\Psi}$ is closest to its true value. The variational principle also ensures the norm and energy are conserved when $H$ is explicitly time-independent and $\Psi \in T_\Psi \mathcal{M}$ [44]. Performing the variation leads to

$$i\dot{A}_J = \sum_L H_{JL} A_L - \sum_{i=1}^{f} \sum_{k=1}^{n} g_{j_i k} A_{j_1 \ldots j_{i-1} k j_{i+1} \ldots j_f} \tag{1.29}$$

$$i\dot{\boldsymbol{\varphi}} = (1-P)\,\boldsymbol{\rho}^{-1}\langle H\rangle\boldsymbol{\varphi} + P\boldsymbol{g}\boldsymbol{\varphi} \tag{1.30}$$

where $J$ stands for the set of $j_i$'s and similarly for $L$, $H_{JL} = \left\langle \varphi_{j_1}\cdots\varphi_{j_f}\right| H \left|\varphi_{l_1}\cdots\varphi_{l_f}\right\rangle$ and $\boldsymbol{\varphi}$ is the column vector containing the spin-orbital functions. The density matrix $\boldsymbol{\rho}$ is given by

$$\rho_{kl} = \sum_{j_2\cdots j_f} A^*_{kj_2\ldots j_f} A_{lj_2\ldots j_f}, \tag{1.31}$$

and the mean-field operator $\langle H\rangle$ is given by

$$\langle H\rangle_{kl} = \left\langle \Psi^{(k)}\right| H \left|\Psi^{(l)}\right\rangle, \tag{1.32}$$

with

$$\Psi^{(k)} = \frac{\delta\Psi}{\delta\varphi_k} \tag{1.33}$$

the single particle hole-function. The projector P onto the space of spin-orbitals is given by,

$$P = \sum_k |\varphi_k\rangle\langle\varphi_k|. \tag{1.34}$$

The constraint $\boldsymbol{g}$ given above is chosen to be $\boldsymbol{g} = 0$ for all implementations of MCTDHF used here.

To illustrate how MCTDHF accounts for electron correlation consider the case with $f = 2$ and $n = 3$. The MCTDHF wave function can be written as

$$\Psi(t) = \underbrace{A_{12}\mathrm{Det}[\varphi_1(t)\varphi_2(t)]}_{\mathrm{Hartree-Fock}} + \underbrace{A_{13}\mathrm{Det}[\varphi_1(t)\varphi_3(t)] + A_{23}\mathrm{Det}[\varphi_2(t)\varphi_3(t)]}_{\mathrm{CorrelationTerms}} \tag{1.35}$$

where $\mathrm{Det}[\varphi_i(t)\varphi_j(t)] = \varphi_i(t)\varphi_j(t) - \varphi_j(t)\varphi_i(t)$ and the coordinates $\mathbf{q}_i$ have been dropped for simplicity. For the $n = f$ case, MCTDHF reduces to the TDHF method. For $n > f$, MCTDHF is better able to treat the electron-electron interaction because, as with TDCI, it uses a larger number of configurations. However, MCTDHF uses a spin-orbital basis set that is optimized at each time. This allows MCTDHF to be better able to represent the wavefunction using a much smaller basis set than is required by TDCI. The outcome of this is MCTDHF is able to handle time-dependent problems for larger numbers of electrons than can be treated by TDCI. Comparative calculations between MCTDHF and TDCI are done in Chap. 2 for a two-electron system.

### 1.1.5 Multiconfiguration time-dependent Hartree method

The multiconfiguration time-dependent Hartree (MCTDH) [44] approach represents the wavefunction as a product *ansatz* similar to MCTDHF. In fact, the development of MCTDHF was motivated by the MCTDH approach. MCTDH represents the wavefunction as

$$\Psi(Q_1,\ldots,Q_m;t) = \sum_{j_1=1}^{n_1}\cdots\sum_{j_m=1}^{n_m} A_{j_1\ldots j_m}(t)\varphi^{(1)}_{j_1}(Q_1;t)\cdots\varphi^{(m)}_{j_m}(Q_m;t) \tag{1.36}$$

where the $Q_k$ are the individual degrees of freedom and $n_k$ are the number of single-particle functions $\varphi^{(k)}_{j_k}(Q_k;t)$ used for each degree of freedom. Here degree of freedom can be taken to mean the coordinate on which the single-particle function is represented. For instance, if

the single-particle function is represented on the 3D cartesian coordinate, then the coordinate ($x$, $y$, $z$) is taken to be an individual degree of freedom. However, if 1D single-particle functions are used, then each $x$, $y$, $z$ will be a single degree of freedom. The expansion coefficients $A_{j_1 \ldots j_m}(t)$ are time-dependent; however, unlike MCTDHF, they are symmetric under the exchange of any two indicies.

The expansion coefficients and the single particle basis functions must satisfy the same constraint conditions as MCTDHF (see Eqs. 1.26 and 1.27). Their equations of motion are derived in the same way as presented in Sec. 1.1.4 with the final result being

$$i\dot{A}_J = \sum_L H_{JL} A_L - \sum_{i=1}^{m} \sum_{k=1}^{n_i} g^{(i)}_{j_i k} A_{j_1 \ldots j_{i-1} k j_{i+1} \ldots j_f} \tag{1.37}$$

$$i\dot{\boldsymbol{\varphi}}^{(k)} = \left(1 - P^{(k)}\right) (\rho^{(k)})^{-1} \langle H \rangle^{(k)} \boldsymbol{\varphi}^{(k)} + P^{(k)} \boldsymbol{g}^{(k)} \boldsymbol{\varphi}^{(k)} \tag{1.38}$$

where all terms in Eqs. (1.37) and 1.38 are defined in a similar way to those in Sec. 1.1.4. Since the derivation is done using the same variational principle as in Sec. 1.1.4 the statement regarding conservation of norm and energy is also valid for MCTDH.

### 1.1.6 MCTDHF and MCTDH codes

Here we make a few notes about the MCTDHF code used in Chap. 2 through Chap. 5 and the MCTDH code used in Chaps. 6 and 7. The MCTDHF code is written in the C programming language. The development of this code is discussed in reference [45]. The MCTDHF code performs calculations by representing the spin orbitals on a uniform Cartesian grid of $1-3$ dimensions. Derivatives are handled using a fast Fourier transform (FFT) algorithm [46] and the property of Fourier transforms:

$$f^{(n)}(\mathbf{r}) = \mathcal{F}^{-1} \left\{ (i\mathbf{k})^n \mathcal{F} \left[ f(\mathbf{r}) \right] \right\} \tag{1.39}$$

where $\mathcal{F}$ denotes the Fourier operator and $\mathbf{k}$ the momentum coordinates. One-body integrals of the form

$$\mathbf{O}_{\mathrm{ij}} = \int \varphi^*_{\mathrm{i}}(\mathbf{r}) \mathbf{O}(\mathbf{r}) \varphi_{\mathrm{j}}(\mathbf{r}) d\mathbf{r} \tag{1.40}$$

where $\mathbf{O}$ is a one-body operator, are calculated using the trapezoidal method [47]. Two-body integrals of the form

$$\mathbf{V}_{\mathrm{ijkl}} = \int \varphi^*_{\mathrm{i}}(\mathbf{r}) \left( \int \varphi^*_{\mathrm{j}}(\mathbf{r}') \mathbf{V}(\mathbf{r} - \mathbf{r}') \varphi_{\mathrm{l}}(\mathbf{r}') d\mathbf{r}' \right) \varphi_{\mathrm{k}}(\mathbf{r}) d\mathbf{r} \tag{1.41}$$

where $\mathbf{V}(\mathbf{r} - \mathbf{r}')$ is a two-body operator depending on difference coordinates, are evaluated in a special way. First, integration over $\mathbf{r}'$ is done using the convolution theorem and the FFT algorithm. What remains is a one-body integral of the form seen in Eq. 1.40; this is then handled using the trapezoidal rule.

The MCTDH code used is the Heidelberg MCTDH Package provided by Theoretical Chemistry Group Heidlberg [48] and is written in FORTRAN. This code has been modified to handle two-body terms in a similar manner as described above; more detail is given in Chap. 6.

For efficient time propagation, both codes use the constant mean-field (CMF) integration scheme [49]. A brief sketch of the CMF scheme is given here; for full details see reference [49]. The CMF scheme is based on the notion that the matrix elements $H_{JL}$ and the product of the

inverse density with the mean field matrix $\boldsymbol{\rho}^{-1}\langle H\rangle$ evolve much slower than the MCTDH(F) coefficients and the single-particle(spin-orbital) functions. This allows for $H_{JL}$, $\boldsymbol{\rho}^{-1}$ and $\langle H\rangle$ to be calculated on a coarser time mesh. The CMF integrator used in both codes is the second order scheme given in reference [49].

Our implementation of MCTDHF expands the wavefunction using spin-orbitals on the coordinate $\mathbf{q}_i$ defined in Sec. 1.1.4. Our implementation of MCTDH, however, expands the wavefunction on the product of 1D single-particle functions. For a the $2\times 2$D system presented in Chaps. 6 and 7, this expansion allows the MCTDH code to complete the calculations approximately twice as fast as the MCTDHF code. While both codes yield the same results, the MCTDH code is used due to the efficiency gained from expansion into 1D single-particle functions. However, this implementation of MCTDH is limited to 2D problems where the spin part of the wavefunction can be factored out. On the other hand, the MCTDHF code is more general in the sense that it includes the spin state and will be able to handle problems with up to $8-10$ electrons in 3D.

To see why the MCTDH implementation becomes problematic for systems with greater than four dimensions, consider the number of expansion coefficients $N_{\mathrm{h}}$ required. For a system with $f$ electrons each moving in a space of dimension $d$ the number of MCTDH coefficients required is

$$N_{\mathrm{h}} = \prod_{k=1}^{fd} n_k \tag{1.42}$$

where $n_k$ is the number of single particle functions used for the $k^{th}$ degree of freedom. If $n_k = n$ for all $k$ then

$$N_{\mathrm{h}} = n^{fd}. \tag{1.43}$$

By contrast, the number of expansion coefficients $N_{\mathrm{hf}}$ required by MCTDHF is

$$N_{\mathrm{hf}} = \binom{n}{f} \tag{1.44}$$

where $n$ is the number of spin-obritals used. While the expansion of MCTDH into 1D single particle functions is more efficient than our MCTDHF implementation for the 2D system, the scaling of $N_{\mathrm{h}}$ renders our implementation MCTDH unviable for most 3D systems; this is demonstrated in Fig. 1.1. Fig. 1.1 shows the number of coefficients $N_{\mathrm{h}}$ and $N_{\mathrm{hf}}$ as a function of $n$ for two and four electrons in three dimensions ($d = 3$). From Fig. 1.1 it can be seen that for two electrons $N_{\mathrm{h}} \approx 10^8$ at $n = 20$. For four electrtons $N_{\mathrm{h}}$ is already completely unmanageable for $n = 10$. By contrast, $N_{\mathrm{hf}}$ remains completely manageable for both the two and four electrons systems.

Throughout the development phase of the codes they were applied to 2D problems in nanophysics and attosecond science. In the subsequent chapters the MCTDHF code is used for all nanophysics problems due to its ability to handle different spin configurations and go beyond two electron systems. In chapters 6 and 7 our implementation of MCTDH is used due to its efficiency in handling the $2\times 2$D system; however, beyond this system it will not be a viable tool. Since the ultimate goal is to perform calculations on 3D atomic and molecular systems under the influence of strong laser fields, an efficient 3D implementation of our MCTDHF code will be presented in chapter 8.

## 1.2 Outline

This document is divided into three parts. The first part presents a treatment of problems in nanophysics; the second part will deal with problems of strong-field physics. Finally, the third

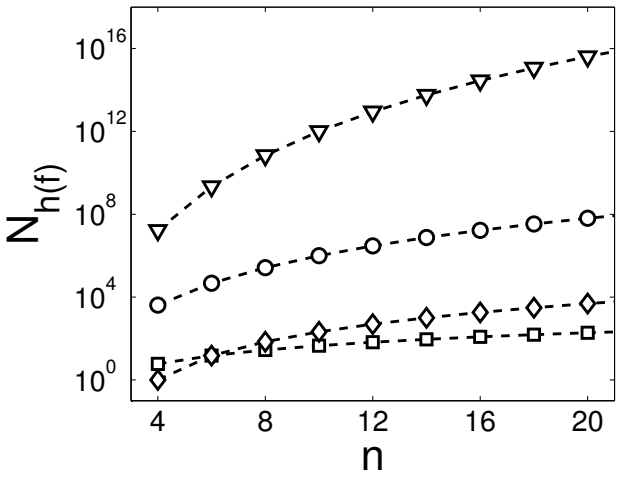


**Figure 1.1.** Scaling of $N_{\mathrm{h}}$ for two ($\circ$) and four electrons ($\triangledown$) with $d = 3$. Shown for comparison is $N_{\mathrm{hf}}$ for two ($\square$) and four ($\lozenge$) electrons in 3D.

part will be the conclusion. Each chapter will have an introduction that will provide some context to the problem being considered along with the relevant literature. This section provides a brief outline of the first two parts.

In Part 1, problems in nanophysics are treated. In chapter 2 MCTDHF is applied to the optimization of the manipulation of a two-electron spin-based coded qubit in a double quantum dot. It is successfully tested against direct integration of the multidimensional time-dependent Schrödinger equation. This investigation presents a basis for the *ab initio* optimization of few-qubit operations. In chapter 3 it is demonstrated theoretically that transition matrix elements between ground and first-excited singlet states of a two-dimensional two-electron lateral double quantum dot can be controlled and changed by orders of magnitude by varying the interdot barrier. As a result, decay arising from system-environment coupling can be controlled. A potential ramp is identified by which the system is nonadiabatically inverted and then frozen by insulating it against environmental decay. In chapter 4 an *ab initio* analysis of laser driven, few electron plasmon dynamics in a finite lateral quantum dot is performed. The results are analyzed by a comparison to a Drude model based on the centre-of-mass motion of the plasmon. It is found that decay and energy absorption during the plasmon-surface interaction do not depend on electron correlation. This suggests that the Kohn theorem — plasmon dynamics in infinite parabolic quantum dots does not depend on electron correlation — is extendable to finite quantum systems. In chapter 5, an analytical operator approach, valid for fermionic and bosonic systems of arbitrary dimension, is developed to calculate the frequency of the quantum breathing mode. This approach is tested by comparison with *ab-initio* numerical calculations for few electron systems confined in two-dimensional (2D) quantum dots. Good agreement is obtained over the whole range from the ideal quantum gas to Wigner crystallization, opening a new route to analyze quantum collective behavior. The analysis reveals that the breathing mode is sensitive to and can be used to diagnose changes in total angular momentum that happens at level crossings. Further, temperature dependence is analyzed and the onset of classical behavior is identified.

Part 2 considers problems in strong-field physics involving atoms and molecules. In chapter 6, an optimized implementation of MCTDH is applied to nonsequential double ionization (NSDI) in a two-electron diatomic model molecule with two-dimensions per electron. The resulting two-electron spectrum exhibits pronounced signatures from which the ionic bound states involved in NSDI are retrieved with the help of a semiclassical model. A mechanism for the ionization dynamics is suggested. In chapter 7, high harmonic generation (HHG) in a two-electron 2D model molecule is calculated exactly. The role of multi-electron dynamics in HHG is analyzed by expanding the two-electron wavefunction in terms of ionic eigenstates. This allows for a systematic way to quantify the importance of correlation and exchange effects. The main source for correlation, along with laser polarization of the neutral molecule and electron exchange, is identified to be the polarization of the ion by the recolliding electron. This effect, which plays an important qualitative and quantitative role, seriously undermines the validity of standard approaches to HHG in multielectron systems. In chapter 8, the MCTDHF method will be extended to nonuniform tensor product grids. This will pave the way to handle strong field ionization problems using three dimensions and larger numbers of electrons. The 3D code in now ready and is being applied to a number of unsolved problems, such as the complex ionization processes observed in Ref. [15], the molecular orbital rearrangement of cations after ionization [14] and electron impact ionization in strong laser fields. In this thesis only preliminary results, such as ground states of complex systems are shown. In chapter 9, a numerical method is developed by which the tunnel ionization dynamics of bound systems in laser fields can be isolated from the total wavefunction, as given by the time-dependent Schrödinger equation. The analysis of the numerical data for a step function field reveals the following definition for the tunnel time. It is the time it takes the ground state to develop the under-barrier wavefunction components necessary for reaching the static field ionization rate. This definition is generalized to time varying laser fields. The tunnel time is found to scale with the Keldysh tunnel time. Chapter 9 establishes the physical meaning of the tunnel time, its relation to the Keldysh tunnel time, and suggests how it can be measured. The treatment of the tunnel time is the only problem presented here that does not examine multielectron effects. Tunneling plays an important role in attosecond science, particularly in HHG, yet questions still remain as to the dynamics of the tunneling process.

# PART 1

# PROBLEMS IN NANOPHYSICS

# Chapter 2

# Ab initio approach to the optimization of qubit manipulation

*C. F. Destefani, C. McDonald, R. M. Abolfath, P. Hawrylak and T. Brabec, Phys. Rev. B* ***78****, 165331 (2008).*

## 2.1 Introduction

Ideally, a qubit is an isolated two-level system, which can be controlled and manipulated for an unlimited time. In practice, qubits are embedded in the spectrum of a host system, which is surrounded by an environment. Leakage, i.e., probability of the system being out of the qubit subspace, to the host spectrum and to the environment leads to information loss and compromises the qubit fidelity. This determines the maximum time, $\tau_q$, over which quantum computation can be performed.

Leakage to the host spectrum can be kept small by performing qubit operations close to the adiabatic limit. However, this limits the time required for one operation to $\tau \gg 1/\Delta^2$, where $\Delta$ is the energy difference between the qubit subspace and the next closest level of the host spectrum. As a result, the number of maximum qubit operations is $N_m \propto \tau_q/\tau$. A lot of effort has been put into maximizing $N_m$ by minimizing both, the leakage to the host spectrum [50] and to the environment [51].

Our work focuses on controlling the coupling between qubit and host spectrum. In the absence of an environment, $N_m$ is maximized by shortening $\tau$ and by minimizing the leakage to the host system, $L_1$. When $\tau$ is reduced, the qubit manipulation takes place in the nonadiabatic regime, i.e. an increasingly broader band of the host spectrum is populated. In order to regain the leaked population at the end of the manipulation, optimum coherent control theory has to be used [52].

Usually, qubit dynamics are modelled using various degrees of approximations based on a reduced Hilbert space, such as by a Hund-Mulliken picture [53], by a multi-level expansion based on adiabatic eigenfunctions [54], or by reducing the spatial dimensions per electron to 1D [55]. Whereas these approximations are sufficient for a qualitative analysis of the dynamics, it is often not clear how close they are to the exact result.

For quantum computation to work, a leakage per operation of $L_1 < 10^{-4}$ is required [56]. As a result, computational approaches with corresponding accuracy are required to quantitatively assess the effectiveness and limits of coherent control methods. To date, little work exists in this direction, and quantitative data of $N_m$ is scarce. The main reason for this shortcoming is a lack of efficient methods that can integrate the multi-dimensional time-dependent Schrödinger equation (TDSE) numerically. Exact calculation of the multi-dimensional wavefunction is prohibitively difficult, as computational demands increase exponentially with the number of qubits.

We report here progress on this challenge. We investigate the Multi-Configuration Time-Dependent Hartree-Fock (MCTDHF) approach [42,44,57] and show that it relaxes computational requirements and opens the door to accurate ($10^{-4} - 10^{-5}$) modeling and optimization of few-electron dynamics in nano-devices and in a broad range of other host systems.

The MCTDHF approach builds on the time-dependent configuration-interaction (TDCI) method [58]. We find that TDCI is in general not ideally suited for modeling few-electron qubit dynamics for two reasons. (i) In the nonadiabatic limit, where a significant fraction of the host spectrum becomes populated, convergence to accuracies better than $10^{-2}$ is extremely slow, and therefore difficult to achieve. (ii) As the complexity of the spectrum increases rapidly with the number of qubits, the required number of configurations quickly becomes unmanageable. MCTDHF relaxes these constraints by optimizing the basis functions in addition to the TDCI coefficients, reducing the size of the required Hilbert space.

In this chapter, MCTDHF is tested and used to optimize the initialization of two-electron spin-based coded qubits in a two-dimensional double quantum dot (DQD) [1, 59–65]. MCTDHF is successfully tested against direct integration of the four-dimensional TDSE. Optimization is performed in the strongly nonadiabatic limit on a simple class of potential ramps, consisting of three linear ramps with variable gradients.

## 2.2 Qubit Subspace

Figure 2.1(a) shows a schematic of the two-electron DQD potential, given by $V(\mathbf{r},t) = V_l(\mathbf{r},t) + V_b(\mathbf{r},t) + V_r(\mathbf{r},t)$. The potentials of the left, right dot and of the barrier ($i = l, r, b$) are given by $V_i(\mathbf{r},t) = W_i(t)U_i(\mathbf{r})$, where $U_i(\mathbf{r}) = \exp[-(\mathbf{r} - \mathbf{d}_i)^2/\Delta_i^2]$; the left, right dot is centered at $\mathbf{d}_{l,r} = (\mp d, 0)$, while the barrier is located at $\mathbf{d}_b = (0, 0)$. The widths and heights of the dots and the barrier are given by $\Delta_i$ and $W_i(t)$, respectively. Only the right dot potential $W_r(t) = W + \epsilon(t)$ is assumed to be biased with time, while $W_l(t) = W$ and $W_b(t) = W_b$ are held constant. The potential detuning is $\epsilon(t) = W_r(t) - W$, which is varied in the range $-2 \leq \epsilon \leq 0$. In the symmetric DQD limit, $\epsilon = 0$, shown in Fig. 2.1(a), each dot has one electron spin, $S_{l,(r)}$; in the asymmetric limit, $\epsilon = -2$, both electrons occupy the right dot.

The DQD parameters used here are $\Delta_l = \Delta_r = 2.5$, $\Delta_b = 1.5$, $W = -5$, $W_b = 1.5$, and $d = 2$. We use effective atomic units throughout the paper; energy, size, and time, are given in terms of effective Bohr radius $R^*$, effective Hartree energy $E^*$, and effective natural time $T^*$, which in GaAs are $R^* = 9.80$ nm, $E^* = 11.85$ meV, and $T^* = 55.55$ fs, respectively.

The operation of a spin-based coded qubit [63] in a DQD is summarized in Fig. 2.1(b). The qubit is encoded in the two lowest levels of the DQD spectrum, which are the singlet ground state $|1> \equiv S$ and the triplet $T_0$. The qubit operation is a three-stage process: (i) Initialization: after starting in the asymmetric ($\epsilon \ll 0$) singlet ground state $S$ with left, right charge $(Q_l, Q_r) = (0, 2)$, the bias is switched off ($\epsilon \to 0$) adiabatically. This transfers the system into the ground state $S$ of the symmetric DQD with $(1, 1)$ charge configuration. (ii) Manipulation: the spin qubit is encoded in the $S - T_0$ states, and can be addressed due to the small singlet-triplet splitting $J$ at $\epsilon = 0$. (iii) Measurement: the DQD is adiabatically biased back to its initial state. By assuming spin-to-charge conversion the charge measured on the right dot can be directly related to the population of the qubit singlet state at the end of stage (ii).

The assumption that the remaining Hilbert space in Fig. 2.1(b) does not play a role in any of those three stages stays valid as long as the biasing occurs adiabatically. We define the adiabatic regime by the (stage (i)) initialization time $\tau_a$ for which the leakage $L_1 = 10^{-4}$; for the parameters used here $\tau_a \simeq 600$. For nonadiabatic time scales $< \tau_a$, charge leaks to excited

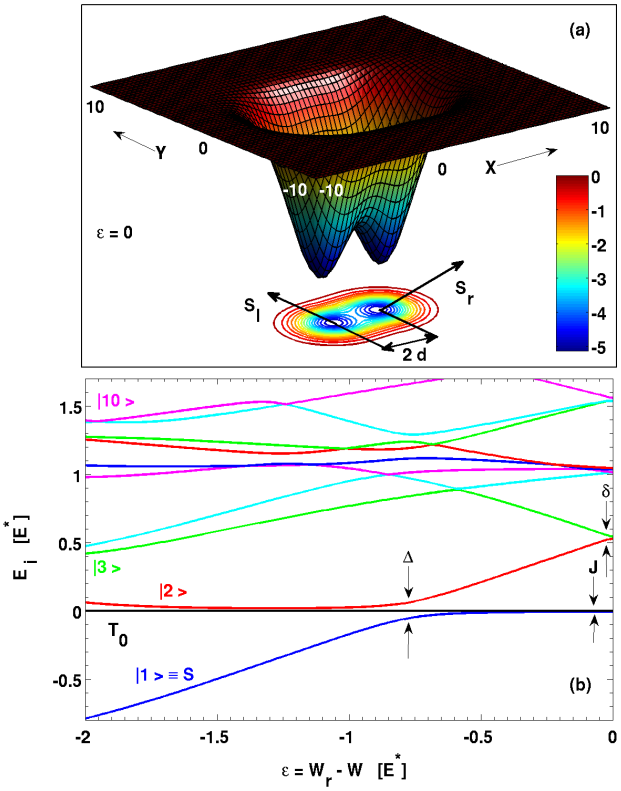


**Figure 2.1.** Panel (a). schematic of the 2D symmetric DQD potential profile with one electron in each dot, $S_{l(r)}$; the grid lines depict the numerical grid used in our simulations: 64 points per dimension in a box ranging from $-10$ to 10; the dots are centered at $(x, y) = (\pm d, 0)$. The detuning between left and right dot is given by $\epsilon = W_r - W$. Panel (b). two-electron spectrum $E_i$ as function of $\epsilon$ for the lowest 10 singlets; energy is plotted with reference to the lowest triplet $T_0$. $\Delta$, $\delta$, and $J$ denote respectively the tunneling splitting between singlets $|1> \equiv S$ and $|2>$, between singlets $|2>$ and $|3>$, and the exchange splitting between $S$ and $T_0$, which depend on $\epsilon$ and $W_b$; the arrows indicate the values $J(\epsilon = 0) = 0.007$, $\Delta(\epsilon = -0.77) = 0.116$, and $\delta(\epsilon = 0) = 0.017$. The triplets $T_+, T_-$ are not shown, as they are usually split off by an additional magnetic field, which isolates the $S_z = 0$ two-level subspace formed by $S$ and $T_0$. Two-electron spectrum calculated from CI diagonalization by using the one-electron basis at each given value of $\epsilon$.

singlet states, compromising the gate fidelity; if some population remains in state $|2>$ once the manipulation stage (ii) is reached, further leakage will happen to state $|3>$ due to the smallness of the $|2> - |3>$ splitting $\delta$ at $\epsilon = 0$, and from there to higher states during the ramp-down stage (iii).

## 2.3 Multi-Configuration Time-Dependent Hartree-Fock Approach

The two-electron dynamics of the spin-based coded qubit is described by the Schrödinger equation

$$i\frac{\partial}{\partial t}\Psi = H(\mathbf{r}_1, \mathbf{r}_2, t)\Psi = \left[\sum_{i=1}^{2} H_1(\mathbf{r}_i, t) + H_2(\mathbf{r}_1, \mathbf{r}_2)\right]\Psi, \tag{2.1}$$

where the wavefunction is $\Psi = \Psi(\mathbf{r}_1, \mathbf{r}_2, t) \otimes |S\rangle$, $\mathbf{r} = (x, y)$ is the 2D space vector, and the spin singlet state is $|S\rangle = |\uparrow\downarrow\rangle - |\downarrow\uparrow\rangle$, which is conserved throughout our analysis. The one-electron Hamiltonian is $H_1 = T + V(\mathbf{r}, t)$, with $T = -\nabla^2/2$ the kinetic energy operator, and the two-electron Hamiltonian is $H_2 = 1/\sqrt{(\mathbf{r}_2 - \mathbf{r}_1)^2 + a^2}$, with parameter $a$ arising from the finite thickness of the 2D DQD (we use $a = 0.5$).

Equation (2.1) is solved by the MCTDHF approach which, for our two-electrons case, uses the ansatz,

$$\Psi(\mathbf{r}_1, \mathbf{r}_2, t) = \sum_{j_1 \neq j_2 = 1}^{n} A_{j_1 j_2}(t)\varphi_{j_1}(\mathbf{r}_1, t)\varphi_{j_2}(\mathbf{r}_2, t)\,|s_{j_1}\rangle\,|s_{j_2}\rangle\,. \tag{2.2}$$

The $n$ single-particle basis functions are characterized by a spin $s_j = \uparrow, \downarrow$ and by an orbital part $\varphi_j$. We use restricted MCTDHF with $n/2$ different orbital basis functions; the resulting number of configurations is $\binom{n}{2}$. The antisymmetry of the wavefunction $\Psi$ is ensured by imposing the constraint $A_{j_1 j_2} = -A_{j_2 j_1}$ on the expansion coefficients; both $A_{j_1 j_2}(t)$ and $\varphi_j(\mathbf{r}, t)$ are time-dependent.

The set of time-dependent nonlinear coupled integro-differential equations for $A_{j_1 j_2}(t)$ and $\varphi_j(\mathbf{r}, t)$ is given by,

$$i\frac{\partial}{\partial t}A_{j_1 j_2}(t) = \sum_{l_1 \neq l_2 = 1}^{n} H_{j_1 j_2 l_1 l_2}(t)A_{l_1 l_2}(t), \tag{2.3}$$

$$i\frac{\partial}{\partial t}\varphi_j(\mathbf{r}, t) = (1 - P(\mathbf{r}, t))\sum_{k,l=1}^{n} R_{jlk}(\mathbf{r}, t)\varphi_k(\mathbf{r}, t), \tag{2.4}$$

where $R_{jlk}(\mathbf{r}, t) = \rho_{jl}^{-1}(t)\langle H\rangle_{lk}(\mathbf{r}, t)$, with $\rho_{jl}(t) = \sum_{i=1}^{n} A_{ji}^{\star}(t)A_{li}(t)$ the density matrix. Further, the projector is $P(\mathbf{r}, t) = \sum_{i=1}^{n} |\varphi_i(\mathbf{r}, t)\rangle\,\langle\varphi_i(\mathbf{r}, t)|$, the mean-field is given by

$$\langle H\rangle_{lk}(\mathbf{r}, t) = \sum_{i=1}^{n} \langle A_{li}(t)\varphi_i(\mathbf{r}_2, t)|H|A_{ki}(t)\varphi_i(\mathbf{r}_2, t)\rangle\,, \tag{2.5}$$

while the two-electron matrix elements are given by

$$H_{j_1 j_2 l_1 l_2}(t) = \langle\varphi_{j_1}(\mathbf{r}_1, t)\varphi_{j_2}(\mathbf{r}_2, t)|H|\varphi_{l_1}(\mathbf{r}_1, t)\varphi_{l_2}(\mathbf{r}_2, t)\rangle\,. \tag{2.6}$$

The ground state at $t = 0$ is found via imaginary time propagation. This converged set of orbitals and coefficients is then taken as the initial state in the propagation of Eqs. (2.3)-(2.4), which yields the many-particle wavefunction in Eq. (2.2) at any time instant.

We compare MCTDHF with two other approaches: (i) TDCI, which is a special case of MCTDHF, where the basis functions are kept fixed in time, that is, $P = 1$ in Eq. (2.4); (ii) a direct split-step integration [66] of the 4D TDSE.

## 2.4 Qubit Dynamics

In the following, we first investigate the nonadiabatic [67] dynamics of the orbital degrees of freedom in the three-stage qubit operation described above. Spin manipulation of the $S - T_0$ qubit, which occurs during stage (ii), and coupling to the environment, are not regarded here. Then, MCTDHF is used to optimize $L_1$ for the nonadiabatic initialization pulse.

### 2.4.1 Convergence of MCTDHF compared with TDCI and exact approaches

In Fig. 2.2, we show the ground state probability $P_1(\tau) = |\langle\Psi_1(0)|\Psi_1(\tau)\rangle|^2$, at the end ($t = \tau$) of the biasing pulse $\epsilon(t)$ shown in the inset, as a function of the number of orbitals (bottom) and configurations (top). The chosen ramping and plateau times, $t_r = t_p = 50$, reflect a worst case scenario that requires a large number of orbitals to converge the highly nonadiabatic dynamics. We have plotted the MCTDHF (circles) and TDCI (squares) results, and for comparison, the exact result from the integration of the 4D TDSE (line). For $n = 50$, the difference between MCTDHF and the exact result is $\simeq 3.1 \times 10^{-4}$. For all other test calculations the agreement was even better, between $10^{-4}$ and $10^{-5}$. As a result, $n \approx 50$ yields the accuracy required for modeling and optimizing qubit dynamics.

On the other hand, TDCI converges much slower. Its convergence depends strongly on the chosen basis. We have tested different basis sets and found fastest convergence for the one-electron basis of the initially biased ($\epsilon = -2$) DQD. Although TDCI converges quickly to an accuracy of $\simeq 1.1 \times 10^{-2}$ for $n = 100$, convergence to higher accuracies is slow and requires unmanageably large basis sizes. This demonstrates the advantage of the MCTDHF basis set optimization during each time step. However, it has to be emphasized that in the adiabatic regime the convergence issues of TDCI disappear.

The computation time on a Xeon E8400 2.8 GHz single core processor is 27 hours for MCTDHF ($n = 50$), 15 hours for TDCI ($n = 100$), while the 4D exact integration takes 16 hours. Although the exact approach is more efficient than MCTDHF in our test calculation, this changes for a larger number of electrons, and for a higher number of grid points (larger DQDs), as the number of points of the exact wavefunction grows as $(N_x N_y)^f$. Here, $N_{x(y)}$ is the number of grid points in $x$ ($y$) direction and $f$ is the number of electrons. When $N_x, N_y$ are doubled for $f = 2$, the exact wavefunction increases by a factor of 16, while MCTDHF ansatz increases only by a factor of 4. Further, the more favorable scaling of MCTDHF with $f$ makes it possible to calculate few-electron dynamics.

For TDCI, the workload goes into the calculation of the time-dependent coefficients, which scales with $\binom{n}{f}$; for $n = 100$, the number of configurations for $f > 2$ electrons explodes, e.g. for $f = 5$ one has $\approx 10^8$ configurations. MCTDHF trades off a lower number of orbitals against the solution of partial differential equations for orbital optimization. For $f = 2$ the main computational effort goes into the optimization of the orbitals; even there the optimized basis gives MCTDHF a clear gain over TDCI, as Fig. 2.2 shows. The gain will become far more pronounced for an increasing number of electrons, where the workload shifts more toward the calculation of the configuration coefficients.

### 2.4.2 Non-adiabatic Qubit Initialization

With the validity of the MCTDHF method established, we can now use it to optimize the bias pulse of Fig. 2.2. We focus here on the qubit initialization, which occurs during the linear ramp-up. For demonstration purposes, a simple class of optimization functions is used, consisting of

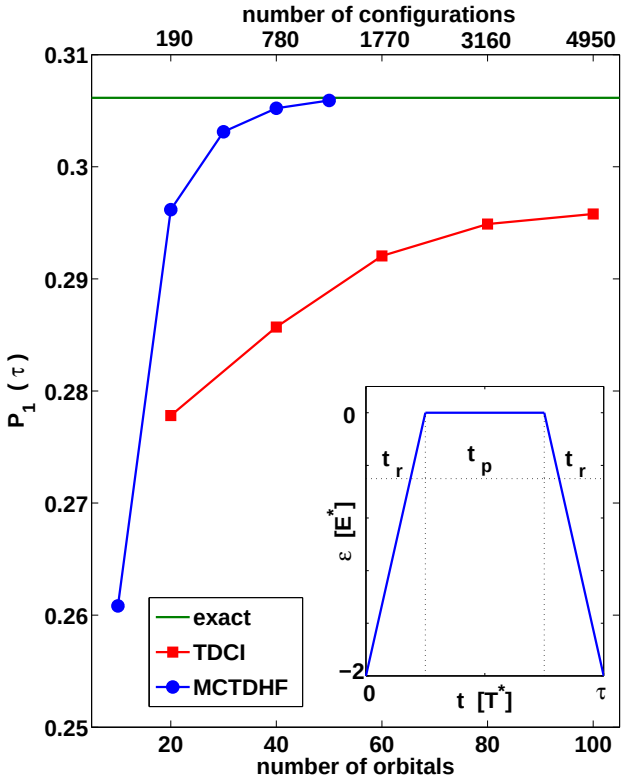


**Figure 2.2.** Ground state probability $P_1(\tau)$ after a completed gate cycle (see inset, for $t_r = t_p = 50$) versus number of orbitals/configurations (bottom/upper $x$-axis). Results from MCTDHF (TDCI) approach are shown with circles (squares), while result from the exact solution of the 4D TDSE is shown as solid line. Inset. Three-stage symmetric bias pulse applied to the right dot: ramp up ($t_r$) from $(0, 2)$ to $(1, 1)$ charge configuration; symmetric DQD maintained during plateau ($t_p$); ramp back to the initial configuration ($t_r$). The full cycle takes $\tau = 2t_r + t_p$.

three linear ramps (see dotted line in Fig. 2.3). Optimization is done in the following way. We first solve the multi-level [54] equations for the first 10 adiabatic eigenstates of the DQD to scan the parameter space. Then, MCTDHF in combination with a Newton algorithm is used for finding the local maximum for $P_1$.

The result is shown in Fig. 2.3, where $P_1$ is plotted as a function of time. The result for the single ramp-up of Fig. 2.2 (dashed line) is compared with the optimized triple ramp-up (solid line). The leakage $L_1 \equiv 1 - P_1$ is improved by $\approx 2$ orders of magnitude, from $\simeq 4.6 \times 10^{-1}$ to $\simeq 1.4 \times 10^{-3}$, for the same initialization time of $t_r = 52$, which is one order of magnitude smaller than the adiabatic time $\tau_a$. In order to reach the threshold of $L_1 < 10^{-4}$ required for quantum computation, $L_1$ has to be further improved by using a more refined set of optimization functions [68].

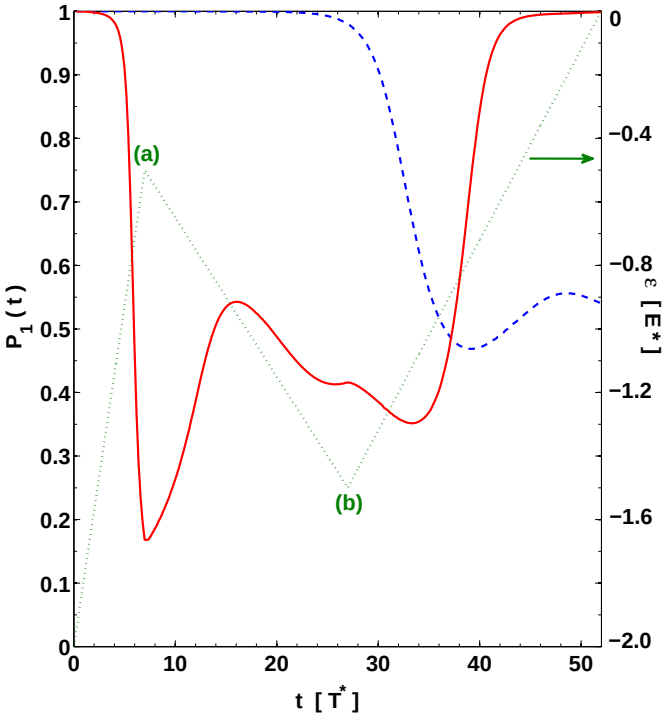


**Figure 2.3.** Time-evolution of ground state probability $P_1$ during the qubit initialization stage for $t_r = 52$. Solid line is for the optimized triple linear ramp-up, shown as dotted lines. The optimum values are $(t_a, \epsilon_a) = (7.0, -0.5)$ and $(t_b, \epsilon_b) = (27.0, -1.5)$. A similar shape can be used for the ramp-down (measurement) stage. Dashed line considers the single linear ramp-up (see inset of Fig. 2.2).

## 2.5 Conclusion

We have demonstrated that MCTDHF is capable of quantitatively describing few-electron dynamics and to predict parameters such as leakage, which are of fundamental importance for quantum computation. We believe that MCTDHF is currently the most viable approach for the analysis of the reliability and optimization of few-qubit operations.

MCTDHF was applied to nonadiabatically accelerate spin-based coded qubit operation in a two-electron DQD. Only the orbital degrees of freedom were considered. Although coupling to the environment was not considered here, speeding up of qubit operations is a powerful way to reduce the influence of the environment, since shorter operation times result in a reduced leakage per operation to the environment. The extension to include spin and coupling to the environment will need to be considered in future work.

# Chapter 3

# Controlling transition matrix elements and relaxation in a two-electron double quantum dot

*C. F. Destefani, C. McDonald, S. Sukiasyan and T. Brabec, Phys. Rev. B* ***79****, 155322 (2009).*

## 3.1 Introduction

Our ability to manipulate matter on a microscopic level rests on creating transitions between eigenstates of a system by introducing a perturbation. The resulting quantum dynamics of the system and between the system and the environment is governed by transition matrix elements (TMEs). For a given perturbation, they are an inherent property of the microscopic system under investigation and can only be changed when the confining potential is changed. Whereas this is very difficult in atomic and molecular physics, tools exist in semiconductor physics by which the confining potential can be changed. [69, 70]

Our theoretical analysis shows that a two-dimensional (2D) two-electron lateral double quantum dot [62,63,71,72] (DQD) is particularly suitable for this purpose. The TME between ground and first excited state, with regard to a general perturbation, can be controlled over orders of magnitude by exploiting the different charge correlation properties of these two states. In the limit of an infinitely high interdot barrier, the ground state of a highly biased DQD has a $(0, 2)$ charge configuration, with two electrons in one dot. The first excited state is in a $(1, 1)$ configuration with one electron in each dot. Due to the different charge distribution character, the wavefunctions of these two states have no overlap; therefore, TMEs between them are zero. As a result, environmentally induced relaxation is turned off and the population of the two-level system is frozen. This is explicitly demonstrated here for coupling to phonon and photon baths. When the interdot barrier is ramped down, the $(0, 2)$ and $(1, 1)$ charge configurations start to mix and the TMEs are switched on, so that the two-level system can be manipulated.

We identify an electric pulse that inverts and freezes the population of the two-level system by modifying the bias and the barrier between the two quantum dots. The capacity to control decay over orders of magnitude is mostly of fundamental interest. Potential applications are discussed at the end of the chapter.

## 3.2 Hamiltonian and two-electron spectrum

The two-electron dynamics in the DQD is described by the Schrödinger equation in effective atomic units

$$i\frac{\partial}{\partial t}\Psi = H(\mathbf{r}_1, \mathbf{r}_2, t)\Psi = \left[\sum_{i=1}^{2} H_1(\mathbf{r}_i, t) + H_2(\mathbf{r}_1, \mathbf{r}_2)\right]\Psi, \tag{3.1}$$

where $\mathbf{r} = (x, y)$, and the in-plane wavefunction is $\Psi = \Psi(\mathbf{r}_1, \mathbf{r}_2, t) \otimes |S\rangle$. The spin singlet state $|S\rangle = |\uparrow\downarrow\rangle - |\downarrow\uparrow\rangle$ is conserved throughout our analysis. The one-electron Hamiltonian is $H_1 = T + V(\mathbf{r}, t)$, with $T = -\nabla^2/2$ the kinetic energy operator and $V(\mathbf{r}, t)$ the potential of the DQD. Further, the two-electron Hamiltonian is $H_2 = 1/\sqrt{(\mathbf{r}_2 - \mathbf{r}_1)^2 + a^2}$, where the parameter $a$ arises from the finite thickness of the 2D DQD. For the calculation of phonon decay below, 3D bulk properties are required. For that we consider the $z$-direction to be confined by a quantum well of size $a$, centered at $z = 0$; the confinement is strong enough that only the lowest vertical sub-band is populated. The resulting 3D wavefunction is $\Psi(\mathbf{r}_1, \mathbf{r}_2, t) \otimes Z(z_1, z_2)$, with $Z(z_1, z_2) = \varphi(z_1) \otimes \varphi(z_2)$ and $\varphi(z) = \sqrt{2/a} \cos(\pi z/a)$.

In our analysis, we consider a GaAs DQD with effective mass $m = 0.067$ and dielectric constant $\nu = 12.4$. The effective atomic units used throughout the paper are then: size in effective Bohr radius $R^* = 9.80$ nm, energy in effective Hartree energy $E^* = 11.85$ meV, and time in effective natural time $T^* \equiv \hbar/E^* = 55.55$ fs.

The lateral DQD potential $V(\mathbf{r}, t) = V_l(\mathbf{r}, t) + V_b(\mathbf{r}, t) + V_r(\mathbf{r}, t)$ consists of the left dot, right dot, and central barrier contributions $V_i(\mathbf{r}, t) = W_i(t) U_i(\mathbf{r})$ $(i = l, r, b)$ with Gaussian shape $U_i(\mathbf{r}) = \exp[-(\mathbf{r} - \mathbf{d}_i)^2/\Delta_i^2]$, width $\Delta_i$ and depth $W_i(t)$. The left dot, right dot, and barrier are centered at $\mathbf{d}_l = (-d, 0)$, $\mathbf{d}_r = (+d, 0)$, and $\mathbf{d}_b = (0, 0)$, respectively, with $2d$ the distance among the dots. In our analysis, $W_r(t) = W + \epsilon(t)$ and $W_b(t)$ are biased with time, while $W_l(t) = W$ is held constant. The potential detuning between the two dots is $\epsilon(t) = W_r(t) - W$; notice that the bias is applied to the right dot, and that $\epsilon = 0$ ($\epsilon < 0$) stands for a symmetric (asymmetric) potential profile. The DQD parameters $\Delta_l = \Delta_r = 2.5$, $\Delta_b = 1.5$, $W = -5$, $d = 2$, and $a = 0.5$ remain fixed throughout the paper.

The size of our DQD is smaller than the size used in GaAs DQD experiments. [62,63,71,72] This choice is driven by numerical convenience. Larger dots have a more closely spaced spectrum and require a much finer grid resolution, which is difficult to handle numerically. However, we would like to stress that the results derived in the following are general and do neither depend on the size of our DQD nor the choice of Gaussian [54,73] potentials $V(\mathbf{r}, t)$. Calculations with somewhat larger dots and different potentials, e.g. a harmonic potential, [53, 74] have given similar results.

The parameters used here were chosen to achieve a two-electron spectrum, see Fig. 3.1, qualitatively similar to the experimental spectra of such systems. [63, 71] Panel (a) shows the spectrum as function of $\epsilon$ at fixed $W_b = 1.5$, while panel (b) does the same but as function of $W_b$ at fixed $\epsilon = -2$; the energy levels (singlets in blue, triplets in red) are plotted with reference to the lowest triplet $|T\rangle$; only the lowest five (three) singlets (triplets) are shown. The two-electron energies $E_i$ and eigenstates $\Psi_i$ are obtained by diagonalizing the configuration interaction (CI) matrix of the Hamiltonian $H$ in Eq. (3.1) with respect to the eigenstates of $H_1$ for each related set of DQD parameters. A basis of 50 spatially distinct one-electron orbitals ($n = 100$ spin orbitals), yielding 4950 two-electron configurations, is sufficient to converge the first few singlet and triplet states.

In the following the properties of the lateral DQD used in our investigation are further specified: i) the distance among the dots is $2d \approx 40$ nm, and $a = 0.5 \approx 5$ nm. If we define the lateral/vertical ratio as $2d/a$, it amounts to 8 in our system; ii) the single-electron lowest energy spacing $\omega_0$ of the isolated (e.g. right) dot can be inferred from $\sqrt{2|W_r|/\Delta_r}$, ranging from $\approx 14.99$ meV at $W_r = -5$ to $\approx 17.73$ meV at $W_r = -7$; further, the one-electron bonding and anti-bonding lowest energy spacing $\omega_{SAS}$ of the coupled double dot is a function of both $\epsilon$ and $W_b$; at e.g. $W_b = 1.5$, such splitting is $\approx 14.6$ meV at $\epsilon = -2$ and $\approx 0.89$ meV at $\epsilon = 0$. iii) the transition energies between the two-electron states in Fig. 3.1(a), which are relevant for our analysis, are: for $\epsilon = 0$, $\delta_{|1\rangle - |T\rangle} = 0.0070 \approx 0.083$ meV, $\delta_{|2\rangle - |T\rangle} = 0.5269 \approx 6.244$ meV,

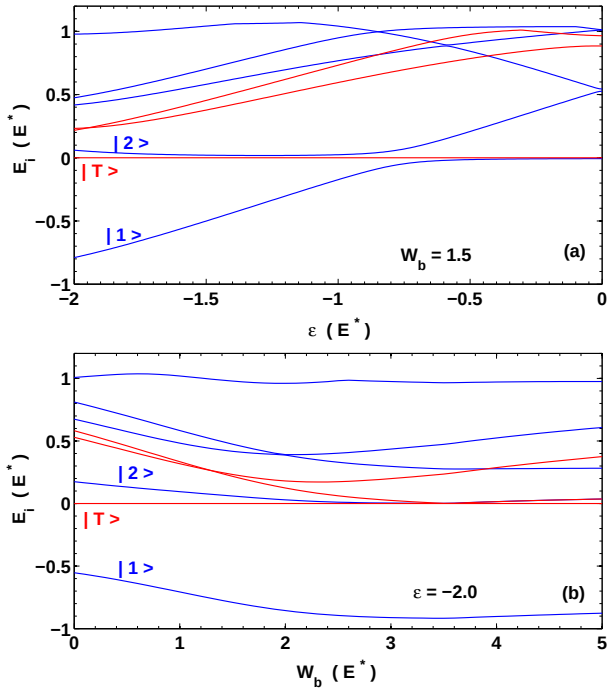


**Figure 3.1.** DQD two-electron energy spectrum $E_i$ as function of the detuning $\epsilon$ between the dots ($W_b = 1.5$, panel (a)), and as a function of the interdot barrier $W_b$ ($\epsilon = -2$, panel (b)). The spectrum (singlets in blue and triplets in red) is shown with reference to the lowest triplet $|T\rangle$. Only the lowest five (three) singlets (triplets) are shown.

and $\delta_{|2\rangle-|3\rangle} = 0.0167 \approx 0.198$ meV; for $\epsilon = -2 \approx 23.7$ meV, $\delta_{|1\rangle-|T\rangle} = 0.7852 \approx 9.305$ meV, $\delta_{|2\rangle-|T\rangle} = 0.0582 \approx 0.690$ meV, and $\delta_{|2\rangle-|3\rangle} = 0.3575 \approx 4.236$ meV. As the barrier is increased in Fig. 3.1(b) for $\epsilon = -2$, among other features, the singlet $|\,2\rangle$ becomes quasi-degenerated with the next excited triplet.

Equation (3.1) is solved by the MCTDHF approach using equations similar to those defined in Section 2.3 of Chapter 2. The singlet ground state at $t = 0$ is found via imaginary time propagation.

## 3.3 Control of transition matrix element

Lateral DQDs are a promising medium for quantum computation. In contrast to spin qubit implementations, [63,71] where the subspace under study is formed by the lowest singlet $|\,1\rangle$ and triplet $|\,T\rangle$ states, our analysis focuses on the subspace formed by the two lowest singlets $|\,1\rangle$ and $|\,2\rangle$.

Figure 3.1(a) shows that it is difficult to address such a two-level singlet subspace at $\epsilon = 0$, because the third singlet state is too close. For that reason, we focus on the asymmetric limit of $\epsilon = -2$. Figure 3.1(b) shows how the transition energies at $\epsilon = -2$ evolve, when the interdot

barrier $W_b$ is increased from 1.5 (17.7 meV) to 5.0 (59.25 meV).

The basic concept underlying the control of TMEs between ground ($\mid \Psi_1\rangle \equiv \mid 1\rangle$) and first excited ($\mid \Psi_2\rangle \equiv \mid 2\rangle$) singlet of a two-electron DQD can be understood from Fig. 3.2, where the possible charge configurations $(N_l, N_r)$ of the lowest three singlets are plotted in panels (a)-(c) as a function of $W_b$, for an asymmetric DQD with $\epsilon = -2$. The charge configuration is determined by first integrating $\mid \Psi_i \mid^2$ over the whole $y_1, y_2$ simulation box; then, $(N_l, N_r)$ is determined by integrating over the respective $x_1, x_2$ integration areas depicted in panel (d). Whereas for a low interdot barrier the eigenstates contain a mix of the different charge configurations, for increasing $W_b$ the eigenstates go over into pure charge configurations. In the limit of an infinitely high $W_b$, all eigenstates take a pure charge configuration. Figure 3.2 shows how the first three singlet states acquire pure $(0,2)$, $(1,1)$, and $(0,2)$ charge character, respectively; in a highly asymmetric DQD, singlets with $(2,0)$ character can only occur at very high excitation energies.

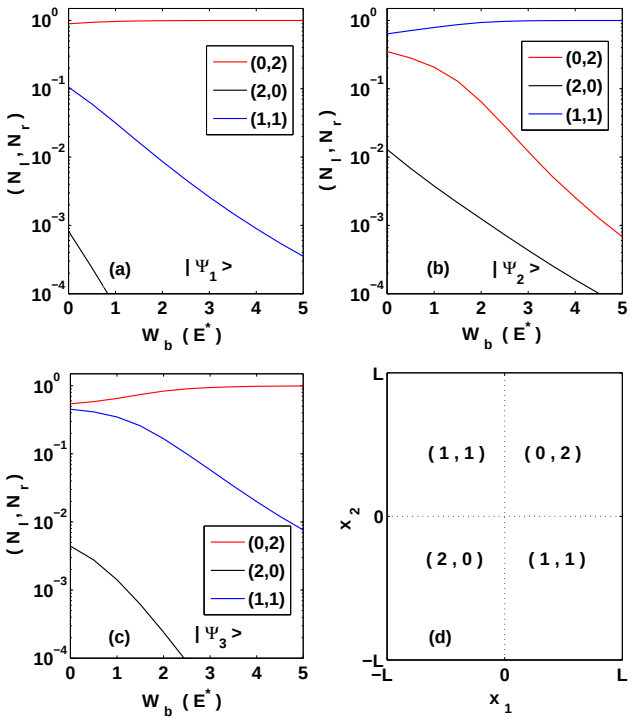


**Figure 3.2.** (a)-(c) Two-electron charge configurations $(N_l, N_r)$ of the lowest three singlets as a function of the interdot barrier $W_b$. (d) $x_1, x_2$ integration areas for the various charge configurations; a square simulation box is employed, with $L = 10$ and $N = 64$ points per dimension.

As two eigenstates with different two-electron charge configurations are in disjoint parts of the simulation volume, their overlap and hence, their product, is zero, e.g. $\Psi_1^*(\mathbf{r}_1, \mathbf{r}_2)\Psi_2(\mathbf{r}_1, \mathbf{r}_2) = 0$ for all $\mathbf{r}_1$ and $\mathbf{r}_2$. Therefore, the TME with respect to a general one- or two-electron operator $\hat{\mathbf{O}}$ vanishes, $\hat{\mathbf{O}}_{12} = \langle 1 \mid \hat{\mathbf{O}} \mid 2\rangle = 0$. In this limit, transitions between these two states are disabled, and the first excited singlet state is preserved against environmentally-induced decay. Note that because all eigenstates are in a pure charge configuration at high $W_b$, all transition

channels between $\mid 1\rangle$ and $\mid 2\rangle$ are suppressed, including higher order transitions taking place via intermediate excited states. When $W_b$ is decreased, the $(0,2)$ and $(1,1)$ configurations in $\mid 1\rangle$ and $\mid 2\rangle$ start to mix, and the TME $\hat{\mathbf{O}}_{12}$ is switched on. On the other hand, the TME among $\mid 1\rangle$ and $\mid 3\rangle$ is always on, since these states have the same predominant charge configuration at any $W_b$.

It is worth to mention that such vanishing of the TME is of fundamental nature in two- or few-electron DQDs, being stable with regard to the specific choice of the single-particle confining potential.

### 3.3.1 Freezing of the two-level singlet subspace

Freezing the population in the first excited state by switching off environmentally-induced decay is demonstrated in Fig. 3.3, where phonon ($\tau_{phonon} = 1/\Gamma$) and spontaneous photon ($\tau_{photon} = 1/\gamma$) emission times from $|2\rangle$ to $|1\rangle$ are plotted as function of $W_b$ for the highly biased DQD with $\epsilon = -2$. Both photon and phonon interactions take place in the THz frequency regime. For the phonon emission rates, we take into account deformation acoustic phonons [75, 76] in polar zincblende structures; the influence of piezoelectric acoustic phonons and higher energetic optical phonons were found to be three orders of magnitude smaller, and therewith negligible in our system. Further, we assume that no excitons and holes exist, so that decay by optical inter-band transitions can be excluded.

The phonon emission rate is given by [77–80]

$$\Gamma = \frac{2\pi}{\hbar} \sum_{\mathbf{Q}} \left| \sum_{i=1,2} F_{21}^{(i)}(\mathbf{q}) \right|^2 |G(q_z)|^2 \, |M(\mathbf{Q})|^2 \, \delta\left(W_{21}\right), \tag{3.2}$$

where $\mathbf{Q} = (\mathbf{q}, q_z)$ and $\mathbf{q} = (q_x, q_y)$. The argument of the delta-function is $W_{21} = (\mid \Delta E_{21} \mid - \hbar v \, |\mathbf{Q}|)$, while the coupling term is $M(\mathbf{Q}) = |\mathbf{Q}| \, \hbar g^2/(2v\rho V)$, with $g = 8.6$ eV the GaAs potential constant and $v = 4.72 \times 10^3$ m/s the longitudinal sound velocity; further, $\rho = 5.31 \times 10^3$ kg/m$^3$ and $V$ are the crystal electronic density and volume, respectively. The in-plane form factor is

$$F_{21}^{(i)}(\mathbf{q}) = \langle \Psi_2(\mathbf{r}_1, \mathbf{r}_2) | \, e^{i\mathbf{q}\cdot\mathbf{r_i}} \, | \Psi_1(\mathbf{r}_1, \mathbf{r}_2) \rangle \, , \tag{3.3}$$

while the perpendicular form factor is

$$G(q_z) = \langle \varphi(z) | \, e^{iq_z z} \, | \varphi(z) \rangle \, . \tag{3.4}$$

The spontaneous photon emission rate in the host material with refraction index $\eta = \sqrt{\nu}$ is given by [81]

$$\gamma = \eta \frac{\Delta E_{21}^3 \mu_{21}^2}{3\pi\epsilon_0 \hbar^4 c^3}, \tag{3.5}$$

where $\epsilon_0$ is the free space permittivity, $c$ is the vacuum light speed, and the dipole moment is

$$\mu_{21} = e \left\langle \Psi_2(\mathbf{r}_1, \mathbf{r}_2) \left| \sum_{i=1,2} x_i \right| \Psi_1(\mathbf{r}_1, \mathbf{r}_2) \right\rangle . \tag{3.6}$$

The dipole matrix elements in $y$ and $z$ are zero due to symmetry reasons.

Figure 3.3 shows that both emission times increase by about three orders of magnitude when going from $W_b = 1.5$ to $W_b = 5$, so that the respective relaxation rates will completely

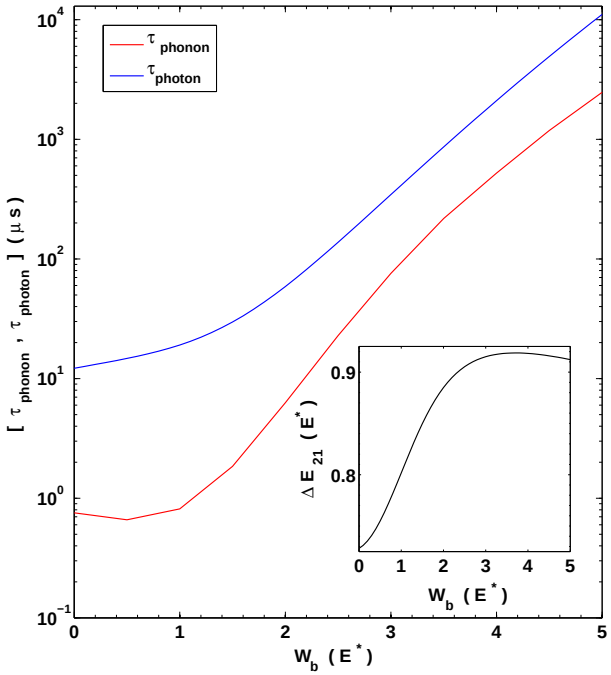


**Figure 3.3.** Phonon relaxation time $\tau_{phonon}$ (red) and spontaneous photon relaxation time $\tau_{photon}$ (blue) from state $|2\rangle$ to state $|1\rangle$ as function of the interdot barrier $W_b$. Inset: energy splitting $\Delta E_{21}$ versus $W_b$.

vanish in the limit of an infinitely high interdot barrier. In the parameter range investigated here, decay can be controlled from the $\mu$s to the ms time scales; when the barrier is further increased, population can be frozen over time scales relevant for the macroscopic world. Since the $W_b$-variation of the level splitting $\Delta E_{21}$ is small (see inset), the change in decay rates from Eqs. (3.2) and (3.5) is mainly due to the decreasing overlap between states $\mid 1\rangle$ and $\mid 2\rangle$, as discussed above. The resonant photon emission wavelength is $2\pi\hbar c/\Delta E_{21} \approx 130$ $\mu$m, while the acoustic phonon emission wavelength is $2\pi\hbar v/\Delta E_{21} \approx 2$ nm, the latter being smaller than both lateral and vertical sizes of the DQD. Both wavelengths yield a frequency of $\approx 15$ THz.

Note that control of the TMEs in a two-electron DQD comes from controlling the tunneling between the dots, which is a single-electron property. Therefore, in principle, the TMEs could also be controlled between states with $(1,0)$ and $(0,1)$ charge configurations in a one-electron DQD. However, in practice, it is much more difficult to address and manipulate pure $(1,0)$ and $(0,1)$ configurations, since they remain superpositions of bonding and anti-bonding states at any $W_b$. In the following, we show that manipulation of a two-electron DQD is, on the other hand, straightforward.

### 3.3.2 Dynamical manipulation of the two-level singlet subspace

Figure 3.4 demonstrates how the inversion of the two-level system is initially induced, and then how this two-singlet subspace is preserved against decay. The manipulation starts from the ground state $|\,1\rangle$ of the strongly coupled, highly biased DQD with $\epsilon = -2$ and $W_b = 1.5$. First, the population is inverted by changing the bias from $\epsilon = -2$ to $\epsilon = -0.2$ and then back to $\epsilon = -2$ (at $W_b = 1.5$), as depicted in panel (a). We use a nonadiabatic technique to invert the system from the ground state $|\,1\rangle$ to the excited singlet $|\,2\rangle$. The avoided crosing between $|\,1\rangle$ and $|\,2\rangle$ in Fig. 3.1 (a) is traversed fast enough to cause a nonadiabatic population transfer. In order to invert the system, the ramp up and the ramp down have to be chosen in a way that the population transfer during the up-down stages adds coherently. After inversion the first-excited state $|\,2\rangle$ is frozen by ramping up the interdot barrier from $W_b = 1.5$ to $W_b = 5$ (at $\epsilon = -2$), as shown in panel (b). A one-dimensional (1D) schematic of DQD potential profile is plotted in the insets for selected positions along the pulse profile. The pulse avoids the symmetric potential $\epsilon = 0$, where state $|\,2\rangle$ becomes quasidegenerate with state $|\,3\rangle$.

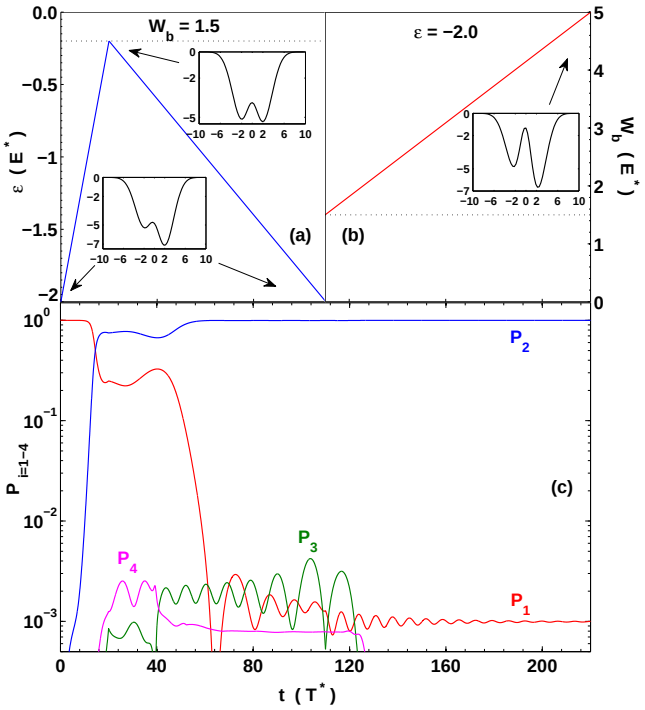


**Figure 3.4.** (a)-(b) Three-stage pulse profile driving the dynamics: (a) $\epsilon$ is increased and decreased back to its initial $\epsilon = -2$ value at $W_b = 1.5$, without reaching $\epsilon = 0$; (b) $W_b$ is increased from 1.5 to 5.0 at $\epsilon = -2$. The insets show a 1D view of the DQD potential at the turning points of the pulse, indicated by arrows. (c) Time evolution of the occupation probabilities of the lowest four singlets, $P_{i=1-4}$, as driven by the pulse in (a)-(b). The $x$-axis in (a)-(b) is the same as in (c).

In panel (c) the time-evolution of the population $P_i$ of the four lowest singlets is plotted, as

driven by the pulse shape in panels (a) and (b); the time-axis in (a) and (b) is the same as in (c). Note that our MCTDHF analysis is converged and therefore accounts for all singlet states involved in the dynamics. In dependence of the ramp parameters, many more than four states can be populated; however, for the parameters chosen here, the lowest two singlets are sufficient. The next two excited states are shown to demonstrate that there is very little leakage (below $10^{-4}$) from the lowest two-level Hilbert subspace to higher singlet states.

During ramping of the bias ($0 \leq t \leq 110$), the system crosses the avoided crossing between singlets $\mid 1\rangle$ and $\mid 2\rangle$ twice (check Fig. 3.1(a)). This is where most of the population transfer takes place. The ramp parameters were chosen to invert the system; the final population of state $\mid 2\rangle$ reaches $P_2 = 0.999$, and could be further enhanced via optimum control theory [82]. The population exchange mainly depends on the phase acquired by the system between the two (avoided) crossings [67]. By small changes in the ramp slopes or ramp times, a wavefunction consisting of arbitrary mixtures of ground and first excited state can be addressed.

Following our pulse, decay of state $\mid 2\rangle$ is then switched off by ramping up the barrier ($110 \leq t \leq 220$), where the splitting $\Delta E_{21}$ follows a smooth behavior (see Fig. 3.1(b) or inset in Fig. 3.3); it change form $\approx 0.75$ to $\approx 0.9$ from the low barrier to the high barrier limit. The smallest energy splitting determines the adiabatic time, $t \gg 2\pi/\Delta E_{21} \approx 8.5$, in which the barrier can be ramped up and down with only minor population losses to the other eigenstates. Our time interval is chosen so that less that $10^{-4}$ of state $\mid 2\rangle$ is lost to other states. It can be seen in Fig. 3.4(c) that the population of state $\mid 2\rangle$ remains unchanged as $W_b$ is increased. This shows that freezing of the quantum state is possible without changing its nature by leakage to other bound states. The time for addressing and freezing the system in Fig. 3.4 is 220 ($\approx 12$ ps). Over this time, phonon and spontaneous photon decays ($\mu$s to ms in Fig. 3.3) are negligible.

## 3.4 Discussion and conclusion

When the interdot barrier in a two-electron DQD is low, the population of ground and first excited singlet states can be controlled by time-dependent biasing of the two dots. The population can be insulated against environmentally-induced decay by ramping up the interdot barrier, which determines the magnitude of the tunneling between the dots. In the limit of an infinitely high barrier, single-electron tunneling is suppressed and the bound states of the two-electron DQD take pure charge configurations. As a result, there remains no overlap between ground and first excited state, so that all one and two-electron TMEs and, therewith, coupling to the environment, vanishes.

We believe that the ability to control TMEs and relaxation is of fundamental importance. An immediate application of this idea to the areas of quantum computation and quantum optics is not trivial and is impeded by obstacles. We would like to discuss some of these difficulties.

First, the two-level singlet subspace investigated here could be used for encoding a two-electron charge [72, 83] qubit. Coupling to the environment is a main obstacle in quantum computation. [59] However, freezing the decay allows us only to control the population of such two-level system, but control over dephasing is very limited. Although there is a dephasing component that accompanies decay and that can be eliminated by switching it off, usually the pure dephasing component is dominant. [84] Pure dephasing depends on matrix elements of the type $\langle 1 \mid \hat{O} \mid 1\rangle$ and $\langle 2 \mid \hat{O} \mid 2\rangle$, which do not depend on $W_b$ and cannot be controlled. These matrix elements cause dephasing by randomly changing the energy spacing of the two-level system, $\Delta E_{21}$. An estimation of the pure dephasing time for our system, following Ref. [84], lies in the ns range. This is orders of magnitude faster than the fastest phonon and spontaneous

photon decay times in Fig. 3.3. Therefore, only in combination with control over pure phonon dephasing, our method can be used to create a decoherence-free subspace [85] for quantum computation. Recently, a couple of methods for the control of phonon-induced dephasing were suggested [86–88].

Second, control over relaxation opens the opportunity to control single photon emission on demand [89]. However, for the DQD parameters used here, single photon THz emission is difficult to observe, as relaxation by phonon emission is more efficient by about one order of magnitude in Fig. 3.3, at any interdot barrier. But there exist several ways to enhance photon emission. For example, $\Delta E_{21}$ can be increased: (i) by increasing the biasing between the two dots to $\epsilon < -2$ in Fig. 3.1(a); (ii) by replacing the first excited $(1,1)$ state of the two-level subspace with the lowest lying singlet state with $(2,0)$ charge character, at $\epsilon = -2$. All the states lying below such highly energetic $(2,0)$ state are of $(1,1)$ or $(0,2)$ character, so that TMEs to these states can be controlled by the interdot barrier. This would give an increase of $\Delta E_{21}$ by a factor of $2-3$; from Eq. (3.5) one finds that an increase of $\Delta E_{21}$ by such amount would already make $\tau_{phonon}$ and $\tau_{photon}$ comparable. Alternatively, one could also use phonon cavities to suppress phonon emission [86].

# Chapter 4

# Plasmon dynamics in strongly driven finite few-body quantum systems: The role of the surface

*C. F. Destefani, C. McDonald, S. Sukiasyan and T. Brabec, Phys. Rev. B **81**, 045314 (2010).*

## 4.1 Introduction

Many-body physics in infinite systems is relatively well understood. Much progress has been made lately in the analysis and understanding of finite many-body quantum systems via approaches such as Configuration Interaction [90–92], Monte Carlo [93, 94], and Unrestricted Hartree-Fock [95–97]. However, most of these static theoretical methods work well only for the calculation of the ground and first few excited states. In terms of dynamics, this means that only weakly perturbed systems can be calculated [98]. Due to the lack of theoretical tools not much is known about strongly driven finite many-particle quantum systems.

This chapter presents a first step towards closing this gap. The recent development of the multi-configuration time-dependent Hartree Fock (MCTDHF) method [42, 57, 99, 100] allows the investigation of the dynamics of strongly driven few-body quantum systems, fully accounting for electron correlation. The investigation of the dynamics in a resonantly driven few-electron, lateral parabolic quantum dot (QD) is the focus here. More specifically, the Schrödinger equation for four electrons with two spatial dimensions per electron (4x2D) is solved for a broad range of QD sizes and therewith electron correlations, covering the phase transition from an electron liquid [101] to a Wigner crystal [102].

In an infinite parabolic QD, with confining frequency $\omega_0$, radiation only couples to the center of mass of the multi-electron system [103,104], which moves collectively as a plasmon with frequency $\omega_p = \omega_0$ (Kohn mode). In the presence of a surface, ionization and dissipation and dephasing of the plasmon dynamics take place. The goal of this investigation is to understand and characterize these surface effects as a function of electron correlation and electric field strength. The relevance of this investigation is not confined to QDs, but relates to all finite quantum systems with collective plasmon-like response, such as clusters nano-particles, large molecules, and harmonic traps. A proof-of-principle *ab-initio* calculation of this ubiquitous process presents the first main result of this chapter.

A comparison between a Drude model [105] and *ab-initio* results is used to analyze the plasmon dynamics in a finite QD. This comparison reveals the second main result of this chapter. The Kohn theorem states that the plasmon motion in an infinite QD does not depend on electron correlation. It is found that energy absorption and dissipation of the plasmon do not depend on electron correlation either. This numerical evidence suggests that the Kohn theorem is extendable

from infinite to finite QDs. The corroboration of this result for larger numbers of electrons requires further tuning and optimization of MCTDHF, which is subject to future research.

Finally, the Drude model works well even in the non-perturbative limit of plasmon-surface interaction, where substantial ionization takes place. Ionization sets a limit to the ultimate field strengths to which the QD can be exposed. A simple picture for the ionization process is developed, from which ionization saturation field strengths can be determined.

## 4.2 Theoretical approach

The few-electron dynamics in the QD is described by the Schrödinger equation in effective atomic units

$$i\frac{\partial}{\partial t}\Psi = H\Psi = \left[\sum_{i=1}^{f} H_1(\mathbf{r}_i,t) + \sum_{i=1}^{f}\sum_{j>i}^{f} H_2(\mathbf{r}_i,\mathbf{r}_j)\right]\Psi, \tag{4.1}$$

where $\mathbf{r}=(x,y)$ is the 2D vector, $f=4$ is the number of electrons, and the in-plane 4x2D wavefunction is $\Psi = \Psi(\mathbf{r}_1,...,\mathbf{r}_f;t)\otimes\Upsilon(\mathbf{s}_1,...,\mathbf{s}_f)$. Here, $\Upsilon$ labels the spin part of the wavefunction, with $\mathbf{s}$ the spinors. The spin state $\Upsilon$ remains conserved during the dipole light-QD interaction investigated here. The one-electron Hamiltonian is $H_1 = T+V(\mathbf{r})+\mathbf{F}(t)\cdot\mathbf{r}$, with $T=-\nabla^2/2$ the kinetic energy operator, and $\mathbf{F}(t)\cdot\mathbf{r}$ the electron-laser interaction term in dipole approximation and in length gauge. The finite QD parabolic confinement is $V(\mathbf{r}) = -\omega_0^2\left(r_c^2-r^2\right)\Theta\left(r_c-r\right)/2$, where $\Theta$ is a step function and $\omega_0$ the confining frequency; the QD boundaries are at $r=r_c=\sqrt{x_c^2+y_c^2}$, so that $V$ is non-zero only for $r\le r_c$ (see 1D profile in inset of Fig. 4.1(d)). The depth of the QD is given by $V_{min}=-\omega_0^2 r_c^2/2$, and the number of single electron bound states contained in the finite QD is given by $s=V_{min}/\omega_0$. The small fluctuations of $V$ due to the host matrix are neglected here, as our emphasis is on the investigation of surface effects. The two-electron Hamiltonian is $H_2 = 1/\sqrt{(\mathbf{r}_2-\mathbf{r}_1)^2+a^2}$, with the parameter $a$ arising from the finite thickness of the 2D QD. Effective atomic units are used throughout the paper, which for a GaAs QD with effective mass $m=0.067$ and dielectric constant $\epsilon=12.4$ reads $R^*=9.80$ nm (Bohr radius), $E^*=11.85$ meV (Hartree energy), $T^*=55.55$ fs (natural time), and $F^*=1.21\times10^4$ V/cm (electric field).

Equation (4.1) is solved by the MCTDHF approach; the initial ground state at $t=0$ is obtained via imaginary time propagation. A basis set with $n=30$ spin-orbitals, yielding $\approx 3\times10^5$ configurations was found sufficient for convergence. The size of the simulation boxes is $5\mathbf{r_c}$, and 512 points per dimension are used. Although the number of orbitals $n=30$ was kept constant in all simulations, it should be noted that in the weakly correlated, low field limit $n=20$ would be sufficient.

The laser driven QD dynamics is investigated as a function of the electron correlation, $r_s = \left[e^2/(\varepsilon l_0)\right]/(\hbar\omega_0)$, which is the ratio of electron-electron interaction energy to kinetic energy. In effective units, $r_s=l_0$, with $l_0=1/\sqrt{\omega_0}$ the radius of the QD ground state. Correlation is varied in the range $r_s=1-10\ R^*$, which covers the transition from an electron liquid in a tightly confined QD at $r_s=1\ R^*$ to the initial stages of Wigner electron crystallization in a wide QD at $r_s=10\ R^*$. Throughout this range, the ground state has total spin $S=1$. The shielding parameter is $a=0.1\ r_s$.

The phase transition can be visualized by looking at the conditional probability distribution, $P_c(\mathbf{r},t) = \int d\mathbf{r}_3 \int d\mathbf{r}_4 \left|\Psi^*(\mathbf{r},\mathbf{r}_2=\mathbf{r}_a,\mathbf{r}_3,\mathbf{r}_4;t)\right|^2$, where one electron is fixed at a position $\mathbf{r}_a$ with a given spin. Figure 4.1 shows $P_c(\mathbf{r},0)$ for three distinct QD ground states, at $r_s=1\ R^*$ (a), 5 $R^*$ (b), and 10 $R^*$ (c), where the fixed $\uparrow$-electron at $\mathbf{r}_a$ is explicitly shown only in (c). Whereas

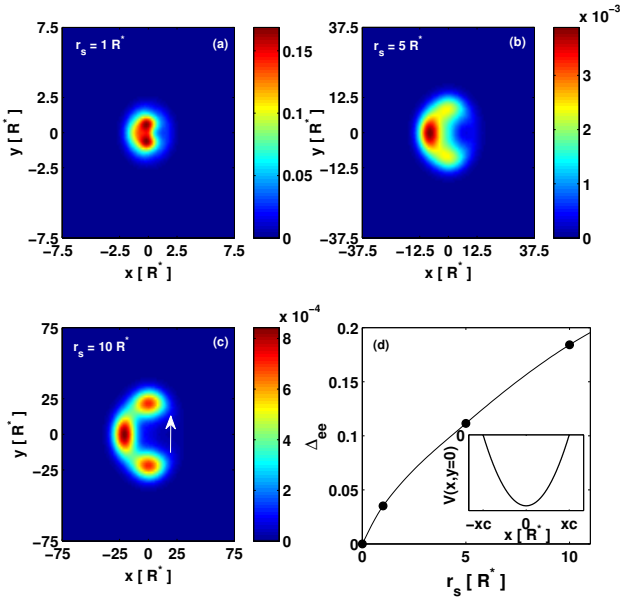


**Figure 4.1.** Ground state conditional probability distribution, $P_c(\mathbf{r}, t = 0)$, for the three $r_s$ values considered in our work, as given by MCTDHF: $r_s = 1$ $R^*$ (liquid phase, (a)), $r_s = 5$ $R^*$ (b), and $r_s = 10$ $R^*$ (solid phase, (c)). The limits of the plot range in each panel are equal to the extension of the finite parabolic potential, $r_c$, whose 1D profile is shown in inset in (d). The parameters $r_s$ and $r_c$ are changed in a way leaving $s = \omega_0 r_c^2/2 = const.$ The full simulation box is five times larger than $(x_c, y_c)$ to capture all of the electron dynamics. (d) shows the normalized correlation energy, $\Delta_{ee}$, as a function of $r_s$. In all panels, $\int d\mathbf{r} P_c(\mathbf{r}, t = 0) = 1$.

the remaining three electrons are more uniformly distributed about QD in the liquid phase (a), the dominant electron-electron repulsion results in crystallization and in three distinct maxima in the solid phase (c), while (b) presents an intermediary case. The ground state energies are $E_0 = -102.2856$ $E^*$, $E_0 = -3.6445$ $E^*$, and $E_0 = -0.8103$ $E^*$ for (a), (b), and (c), respectively. In Fig. 4.1(d), the ratio $\Delta_{ee} = \left(E_0 - \bar{E}_{0)}\right) / \left|\bar{E}_0\right|$ is plotted as a function of $r_s$, where $\bar{E}_0$ is the bound state energy in the non-interacting limit. This ratio increases almost linearly with $r_s$, as a result of the increasing correlation and electron repulsion.

This study focuses on the resonant dynamics, with laser frequency $\omega_l = \omega_0 = \omega_p$, where $\omega_p$ is the plasmon (Kohn) frequency of an infinite harmonic potential. The laser pulse, $F(t) = F_0 \sin(\omega_0 t) f(t/\tau)$ is polarized along $\widehat{x}$. The envelope is a half-cycle $\sin^2$ pulse, $f = \sin^2(\pi t/(n_c \tau))$, which is $n_c = 3$ optical cycles long; $\tau = 2\pi/\omega_0$ is the optical cycle and $F_0$ the peak field strength. The simulation is run for another cycle after the end of the pulse, see inset of Fig. 4.2(c).

## 4.3 Analysis of plasmon surface dynamics

In order to isolate the effect of electron correlation on the plasmon dynamics in a finite QD, care has to be taken with the variation of the parameters. A change of the electron correlation, $r_s = 1/\sqrt{\omega_0}$, also changes the single electron properties of the QD, which is undesirable. Therefore,

to isolate the role of correlation, both QD parameters $r_s$ and $r_c$ have to be varied in a way that the resulting changes of the single electron properties of the QD are trivial. This can be achieved by using the transformation $T = t\omega_0$, $(\xi, \eta) = \sqrt{\omega_0}(x, y)$, and $\rho = \sqrt{\omega_0}r$, which renders the Schrödinger equation for the single electron QD into

$$i\frac{d}{dT}\Psi = -\frac{1}{2}\left(\frac{d^2}{d\xi^2} + \frac{d^2}{d\eta^2}\right)\Psi + V(\rho)\Psi - \xi F(T)\Psi. \tag{4.2}$$

Here, $F(T) = F_s f(2\pi T)\sin(T)$, $F_s = F_0/\omega_0^{3/2}$, $\rho_c = r_c/\sqrt{\omega_0}$, and $V = (-s + \rho^2/2)\Theta(\rho_c - \rho)$. In our simulations, see Fig. 4.1, $r_s$ and $r_c$ are changed in a way leaving the number of single-particle eigenstates contained in the QD constant, $s = \omega_0 r_c^2/2 = 28$. As a result, Eq. 4.2 becomes scaling invariant with regard to changes in $\omega_0$ ($r_s$), and the surface induced decay of the laser driven single electron motion is proportional to $\exp(-\gamma_0 T)$. From a solution of the single electron Schrödinger equation (4.2) for various field strengths $F_0$ we obtain $\gamma_0 = 0.5$. Transformation back to effective units yields a decay $\exp(-\gamma t)$ with surface collision frequency $\gamma = \omega_0\gamma_0$. As a result, the decay constant measured in units of oscillation periods is constant, $\gamma\tau = 2\pi\gamma_0$. When the *ab-initio* few-electron plasmon decay follows this relation, it can be modeled by an effective single-particle, uncorrelated, center-of-mass Hamiltonian. Any deviation from this relation must be attributed to electron correlation.

The plasmon surface dynamics is analyzed by comparing the ab-initio results with a classical damped harmonic oscillator (HO) Drude model,

$$\ddot{x} = F(t) - \omega_0^2 x(t) - 2\gamma\dot{x}(t), \tag{4.3}$$

where $\gamma$ is the surface collision frequency. In order to get good agreement with the quantum results, the Drude model must be modified for surface collisions. First, in the strong field limit, the bound wavefunction is driven over the surface which modifies the plasmon frequency $\omega_0 = \omega_p$. This is accounted for by substituting $\omega_0^2 \to \omega_0^2(1 - \beta^2)$. In a more detailed model, the frequency shift should appear only during the times in the laser cycle where the wavefunction is strongly deflected by the surface. Second, surface dissipation does cutoff at a velocity $v_c$, below which the plasmon does not reach the surface anymore. This is accounted for by cutting dissipation for plasmon velocities $v \leq v_c$. The phenomenological modifications identified here present a starting point for developing a generalized Drude model for plasmon surface collisions, which is beyond the scope of what is being considered here. It should be emphasized that they are needed to obtain fair agreement with the quantum result over the whole simulation range in Fig. 4.2. However, they are not needed to determine $\gamma$, which can be obtained from fitting the plasmon decay in the time interval in which $v \geq v_c$.

The time evolution of the kinetic energy in $\widehat{x}$-direction is shown in Fig. 4.2 as determined by the MCTDHF analysis (full), the classical damped HO of Eq. (4.3) (dotted), and the classical undamped HO model (dashed); (a), (b), and (c) show the results for $r_s = 1$ $R^*$ ($F_s = 1.5$), $r_s = 5$ $R^*$ ($F_s = 1.375$), and $r_s = 10$ $R^*$ ($F_s = 1.25$), respectively. The MCTDHF plasmon expectation values are calculated by using the part of the wavefunction in the box circumscribing the QD; as for some of the parameters substantial ionization takes place, the total wavefunction has to be split into a plasmonic, bound part and an ionized part.

The main result obtained from the Drude model fit is the relation for the collision frequency, $\gamma = \omega_0/2$, see inset in 4.2(a). Many more calculations in the parameter range $r_s = 1 - 10$ $R^*$ and $F_s = 0.5 - 1.5$ have been performed. In the whole range, $\gamma$ is independent of $F_s$. The $\omega_0$ dependence of $\gamma$ is identical with the scaling in the single electron limit, derived above. As a result, the influence of correlation on the surface induced plasmon decay is negligible. In terms

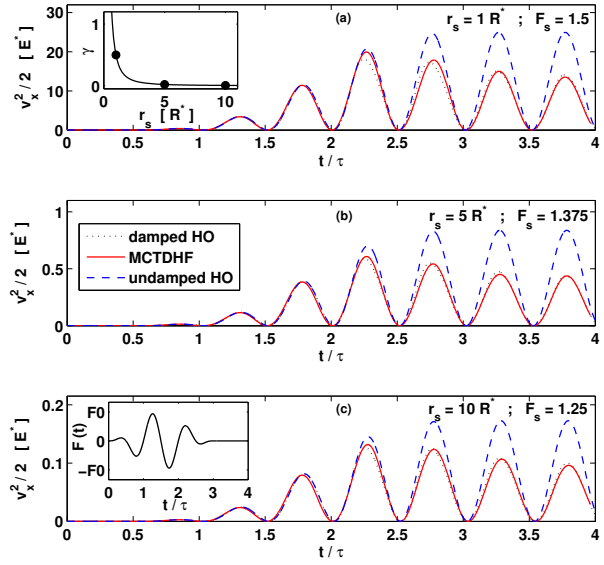


**Figure 4.2.** Time evolution of the kinetic energy, $v_x^2/2$, in the $\hat{x}$-direction of the external pulse $F(t)$, for each $r_s$ value considered in Fig. 4.1. The plots are for the highest $F_s$ values used in our simulation. In all panels, dashed, solid, and dotted lines respectively stand for undamped HO, MCTDHF, and damped HO results. The simulation time extends over the 3-cycle pulse plus an extra cycle, as shown in inset in (c); $\tau$ is the laser oscillation period. Inset in (a) shows the collision frequency $\gamma$ as a function of $r_s$. The Drude model parameters $v_c$ and $\beta$ (see text) depend smoothly on $r_s$ and weakly on $F_s$. We use $v_c \approx 5.0, 0.85, 0.38$, and $\beta \approx 0.005, 0.01, 0.015$, for $r_s = 1, 5, 10\ R^*$, respectively.

of the energy spectrum, surface dissipation comes from a coupling between plasmon and highly excited electronic states, close to the continuum threshold.

In Fig. 4.2 the highest field dynamics are displayed, to demonstrate that the Drude model works well even in the non-perturbative limit, where substantial ionization takes place, see Fig. 4.4. All fits, in the whole simulation range defined above, show an agreement comparable to or better than the ones in Fig. 4.2. At weaker fields, not shown here, where the interaction with the surface is negligible, the classical undamped model reproduces exactly the MCTDHF result, in agreement with the Kohn theorem.

Besides dephasing the plasmonic motion, the surface also modifies the energy absorption process. In Fig. 4.3 the total energy absorbed during the QD-laser interaction given by,

$$E_{abs} = \int_0^{4\tau} dt' \sum_{i=1}^{f} F_i(t') \langle \Psi(t') | \mathbf{v}_i | \Psi(t') \rangle, \tag{4.4}$$

is plotted versus $F_s$. Integration is again performed over the box circumscribing the QD. In the classical analysis $\langle \Psi(t') | \mathbf{v}_i | \Psi(t') \rangle$ is replaced by $\dot{x}_i(t)$ from Eq. (4.3). $E_{abs}/|E_0|$, the absorbed energy over the ground state binding energy, for $r_s = 1$, 5, and 10 $R^*$ has been plotted.

Figure 4.3 shows that even at high $F_s$ values, the influence of the surface is weak and energy

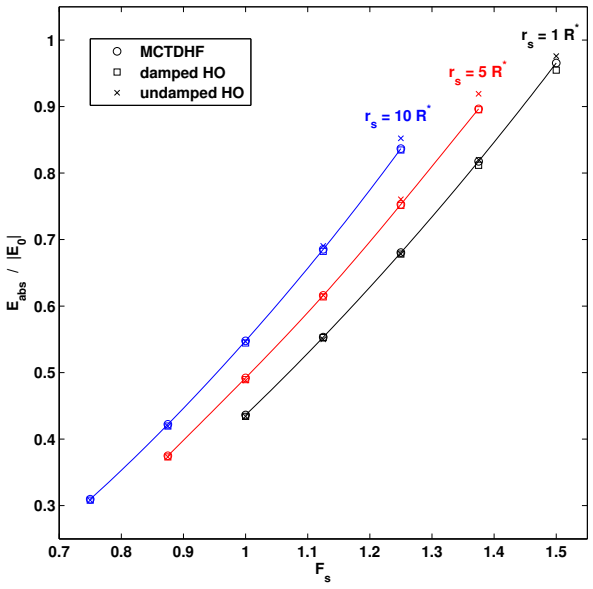


**Figure 4.3.** Total absorbed energy scaled by (4-electron) QD ground state energy, $E_{abs}/|E_0|$, as a function of $F_s$ at the end of the laser pulse for $r_s = 1\ R^*$, $5\ R^*$, and $10\ R^*$; quantum MCTDHF (circles), classical damped HO (squares), and classical undamped HO (crosses) calculations.

absorption is always dominated by the plasmon resonance. As a result, both, plasmon dissipation and energy absorption in the presence of a surface do not depend on electron correlation. Note that the highest $F_s$ values used here at each $r_s$ are the highest values that can be applied to the neutral QD; as ionization of the first electron is already substantial, higher values of $F_s$ would lead to its complete ionization, see Fig. 4.4.

## 4.4 Plasmon-assisted single and double ionization

Plasmon assisted ionization can be understood in terms of a simple picture. The ionization potential of the weakest bound electron is given by $I_p$, which denotes the energy required to remove it from the QD. As the plasmon dynamics is a collective effect, each of the electrons carries on average the same amount of energy, $E_{abs}/4$. When $E_{abs}/4 = I_p$, the weakest bound electron has absorbed sufficient energy to leave the QD by above barrier ionization. Around the onset of above barrier ionization the probability of ionization of the weakest bound electron approaches unity and ionization saturates.

This picture is quantitatively corroborated by Fig. 4.4(a), where the one-electron ionization probability, $I_{1e}$, is shown versus $F_s$. The values of $I_p$ are 24.66, 0.76, and 0.14 for $r_s = 1\ R^*$, $5\ R^*$, and $10\ R^*$, respectively. Using Fig. 4.3 we find the $F_s$ values at which $E_{abs}/4 = I_p$ to be respectively 1.49, 1.32, and 1.14. At these $F_s$ values, close to 50% of the first electron has been ionized, i.e. ionization is starting to saturate, in agreement with the picture developed above. These $F_s$ values present the saturation field strengths for one-electron ionization, which is the

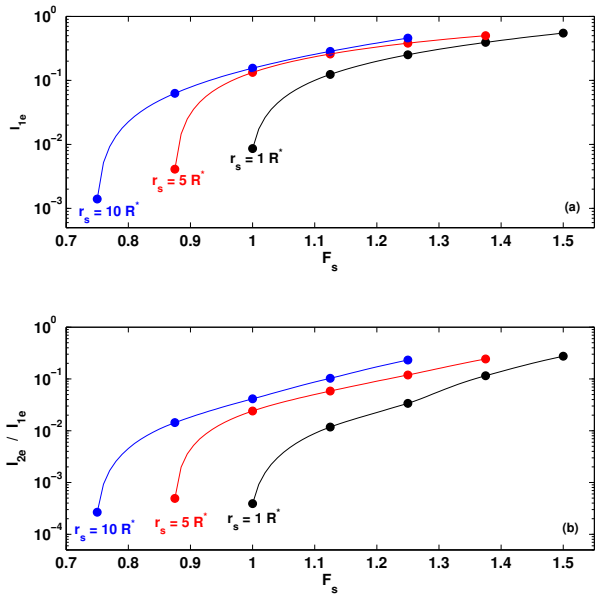


**Figure 4.4.** MCTDHF results for ionization at the end of the laser pulse for $r_s = 1\ R^*$, $5\ R^*$, and $10\ R^*$, as a function of $F_s$. (a) one-electron ionization probability, $I_{1e}$; (b) ratio of two-electron ionization to one-electron ionization probability, $I_{2e}/I_{1e}$.

ultimate field strength the (neutral) QD can be exposed to.

As the plasmon oscillation is a collective motion and the gained energy is shared between the electrons, not only the ionization of the first electron is accelerated but also correlated tunnel ionization of two or more electrons can take place. The ratio of one- to two-electron ionization probability, $I_{2e}/I_{1e}$, is shown in Fig. 4.4(b). Whereas at small $F_s$ this ratio is small, $I_{2e}/I_{1e} \simeq 0.25$ becomes substantial for the highest $F_s$ values at each correlation $r_s$.

## 4.5 Concluding remarks

An *ab-initio* analysis of a laser-driven plasmon in a finite lateral quantum dot was performed for the special case of four electrons. The correlation of the electrons was tuned from the weakly correlated electron liquid to the strongly correlated limit of Wigner crystallization. It was found that the influence of correlation on the surface-induced plasmon decay is negligible. This suggests that the Kohn theorem — plasmon dynamics in infinite parabolic quantum dots does not depend on electron correlation — can be extended to finite quantum dots. This assertion will need to be tested by performing calculations involving larger numbers of electrons.

# Chapter 5

# Theory and characterization of the quantum breathing mode

*C. R. McDonald, G. Orlando, J. W. Abraham, D. Hochstul, M. Bonitz and T. Brabec, Phys. Rev. Lett. (submitted).*

## 5.1 Introduction

Physics is replete with systems of trapped interacting particles. Collective modes, which can be measured experimentally [106], are an important component of the response and dynamics of these finite many-body systems. In terms of a multipole expansion, the first two modes are the breathing (monopole) and Kohn (dipole) mode [107]. Whereas the dipole mode can be treated analytically [108], the situation is more complex for breathing and higher-order modes. In this chapter the quantum breathing mode (QBM) is investigated.

For systems that can be treated classically — confined plasmas [109], trapped ions [110], and colloidal particles [111] — the breathing mode is well understood [112, 113]; however, for quantum systems — Fermi [107, 114] and Bose [114, 115] gases, correlated electrons in quantum dots [7] and low dimensional Bose-Einstein condensates [116, 117] — the QBM still poses many theoretical challenges. First, exact numerical solutions going beyond two electrons [118] are extremely difficult and have only recently been investigated for 1D systems [119]. Second, existing analytical approaches utilize linear response theory and the sum rule formalism, see for example [120–122]. These methods give a rigorous upper bound to the QBM frequency and the correct values in the limits of a free electron gas and Wigner crystallization [121, 122]; however, in the range between these two limits it is not known how well the QBM frequency can be approximated.

The goal here is to close these gaps. First, an analytical theory of the QBM is developed that is valid for fermionic and bosonic systems of any particle number and arbitrary dimension. Second, this theory is tested by comparing it to ab-initio numerical calculations for the special case of electrons confined in a 2D quantum dot (QD). The results are used for characterizing the QBM. QDs have been chosen due to their importance for practical applications in nano-science and technology [6] and in other phenomena of condensed matter physics, such as the quantum Hall effect [123, 124]. Furthermore, they are important from the fundamental perspective of many-body physics. By changing the size of a QD, a multi-electron system can be investigated over a wide range of states characterized by the coupling parameter $\lambda$ given by Eq. (5.4) below. The states range from a weakly correlated, free electron gas ($\lambda \ll 1$), to metallic systems ($\lambda \approx 1$), to the highly correlated, classical limit of Wigner crystallization ($\lambda \gg 1$).

Ab-initio modelling of few-body quantum dynamics has been made possible by the development and optimization of multi-configuration time-dependent Hartree (MCTDH) [125] for Bosons and multi-configuration time-dependent Hartree-Fock (MCTDHF) [42] for Fermions. Here, the numerical analysis is based on MCTDHF as outlined in chapter 4; calculations of the QBM are

performed for $N = 2-4$, 6 electrons in their ground state. The range between an ideal quantum gas and Wigner crystallization is covered and discussed. For $N = 4$ the QBM is also calculated for the first excited state in order to gain information about its temperature dependence. We discuss the onset of classical behavior and analyze the $\lambda$ dependence of the QBM, in particular during level crossings, where eigenstates undergo substantial changes. The QBM is found to be sensitive to changes of the total angular momentum resulting in characteristic signatures of its $\lambda$ dependence.

The numerical data allows us to develop and test approximate analytical expressions for the QBM frequency. Starting from the Heisenberg equation of motion for the harmonic trap, an expression is obtained that determines the breathing frequency as the expectation value of a time-independent two-body operator. The expression is derived for a general inverse power interaction law and verified for Coulomb interaction. Good agreement with MCTDHF is obtained over the whole range of $\lambda$-values, validating our operator approach. In combination with configuration interaction or quantum Monte-Carlo methods, the QBM dynamics for systems of up to a few tens of particles becomes accessible [93]. This opens a new route to investigate and analyze quantum collective behavior. Extension of this operator formalism to other collective modes will be investigated in future research.

## 5.2 Analytical approach

We begin by deriving the operator expression for the QBM frequency from the Heisenberg equation of motion. The derivation will be done for a general (possibly shielded) inverse power-law interaction and will be valid for bosonic and fermionic systems of any dimensionality. Units of energy, length and time are given by $\hbar\Omega$, $l_0$, and $\Omega^{-1}$ respectively, where $\Omega$ is the trap frequency and $l_0 = \sqrt{\hbar/m\Omega}$ is the oscillator length with $m$ being the mass of the trapped particles. These units are used throughout this chapter unless otherwise indicated. In the following we denote the operators in the Heisenberg picture as $\hat{\mathbf{O}}(t) = e^{i\hat{H}t}\mathbf{O}e^{-i\hat{H}t}$ and differences as $\hat{\mathbf{O}}_{\mathrm{ij}}(t) = \hat{\mathbf{O}}_{\mathrm{i}}(t) - \hat{\mathbf{O}}_{\mathrm{j}}(t)$. The $N$ particle Hamiltonian $\hat{H} = \hat{T} + \hat{U} + \hat{V}$ can be written in terms of center-of-mass (CM) and relative coordinates where

$$\hat{T}(t) = \hat{T}_{\mathrm{cm}}(t) + \hat{T}_{\mathrm{rel}}(t) = \frac{N}{2}\hat{P}^2(t) + \frac{1}{2N}\sum_{i<j}^{N}\hat{\mathbf{p}}_{\mathrm{ij}}^2(t) \tag{5.1}$$

is the kinetic energy, with $\hat{P}(t) = (1/N)\sum_i \hat{\mathbf{p}}_{\mathrm{i}}(t)$ and

$$\hat{U}(t) = \hat{U}_{\mathrm{cm}}(t) + \hat{U}_{\mathrm{rel}}(t) = \frac{N}{2}\hat{X}^2(t) + \frac{1}{2N}\sum_{i<j}^{N}\hat{\mathbf{x}}_{\mathrm{ij}}^2(t) \tag{5.2}$$

is the parabolic confining potential, with $\hat{X}(t) = (1/N)\sum_i \hat{\mathbf{x}}_{\mathrm{i}}(t)$. The interaction between particles is given by,

$$\hat{V}(t) = \sum_{\mathrm{i<j}}^{N} \frac{\lambda}{\left(\hat{\mathbf{x}}_{\mathrm{ij}}^2(t) + a^2\right)^{\alpha/2}} \tag{5.3}$$

where, for 2D QDs, the shielding parameter $a$ accounts for the fact that integration over the wavefunction of the third (transverse) dimension results in an effective shielding of the Coulomb

singularity. In Eq. (5.3), $\lambda$ is a general coupling parameter; in the Coulomb case ($\alpha = 1$) $\lambda$ is given by,

$$\lambda = \frac{e^2}{4\pi\hbar\epsilon_0 l_0 \Omega} \tag{5.4}$$

where $e$ is the electron charge and $\epsilon_0$ the permittivity of free space.

The operator $\hat{U}$ represents the radial distance squared of the multi-particle system from the origin. Its time evolution, subject to a radially symmetric initial distortion, is determined by the QBM. The starting point of our derivation is the equation of motion for $\hat{U}$; this is derived in a similar way to Ref. [126]. Here, we sketch the derivation for the shielded potential. We begin with the operator

$$\hat{S} = \frac{1}{2}\sum_{\mathrm{i}=1}^{N} (\hat{\mathbf{x}}_\mathrm{i} \cdot \hat{\mathbf{p}}_\mathrm{i} + \hat{\mathbf{p}}_\mathrm{i} \cdot \hat{\mathbf{x}}_\mathrm{i}) \tag{5.5}$$

that performs a radial displacement of each coordinate. Noting that $\hat{S} = d\hat{U}/dt$ we can then write,

$$\frac{d^2\hat{U}}{dt^2} = \frac{d\hat{S}}{dt} = i[\hat{H}, \hat{S}]. \tag{5.6}$$

It is then straightforward to show $i[\hat{U}, \hat{S}] = -2\hat{U}$, $i[\hat{T}, \hat{S}] = 2\hat{T} = 2\hat{H} - 2\hat{U} - 2\hat{V}$ and

$$i[\hat{V}, \hat{S}] = \alpha\hat{V} - \sum_{\mathrm{i}<\mathrm{j}}^{N} \frac{\alpha\lambda a^2}{\left(\hat{\mathbf{x}}_{\mathrm{ij}}^2(t) + a^2\right)^{\alpha/2+1}}. \tag{5.7}$$

Putting the above relations into Eq. 5.6 then yields,

$$\frac{d^2}{dt^2}\hat{U}_\mathrm{rel}(t) = -4\hat{U}_\mathrm{rel}(t) - (2-\alpha)\hat{V}(t) + \sum_{i<j}^{N} \frac{\alpha\lambda a^2}{\left(\hat{\mathbf{x}}_{\mathrm{ij}}^2(t) + a^2\right)^{\alpha/2+1}}. \tag{5.8}$$

The CM portion of the equation has been removed as it is straightforward to show that $\hat{U}_\mathrm{cm}$ will satisfy a simple harmonic oscillator equation with frequency $\omega_\mathrm{cm} = 2$ [118]. The Hamilton term is left out of Eq. (5.8) as it is a constant of motion and does not influence the time evolution. Since Eq. (5.8) depends on $\hat{U}_\mathrm{rel}$ and $\hat{V}$, it cannot be solved in general, except for the limits $\lambda \to 0, \infty$; in the Coulomb case these limits give $\omega_\mathrm{b} = 2, \sqrt{3}$, respectively [126].

In order to excite the breathing mode, an eigenstate of $\hat{H}$ is changed by a small perturbation to $|k'\rangle = e^{-i\beta\hat{S}_0}|k\rangle = |k + \Delta k\rangle$. Here, $\hat{S}_0 = \hat{S}(\hat{\mathbf{x}}(0), \hat{\mathbf{p}}(0))$ is some operator, such as the dilation operator [126], that excites the QBM at initial time $t = 0$ and $\beta$ is a small real parameter. Further, $\hat{\mathbf{x}}(t) = (\hat{\mathbf{x}}_1(t), \ldots, \hat{\mathbf{x}}_N(t))$ and $\hat{\mathbf{p}}(t)$ is defined in the same way. Using these definitions we can introduce the perturbed space and momentum operators $\hat{\boldsymbol{\xi}}_i$ and $\hat{\boldsymbol{\pi}}_i$, respectively. They are defined through the expectation values $\langle k'|\,\hat{\mathbf{x}}_i(t)\,|k'\rangle = \langle k|\,\hat{\boldsymbol{\xi}}_i(t)\,|k\rangle$ and $\langle k'|\,\hat{\mathbf{p}}_i(t)\,|k'\rangle = \langle k|\,\hat{\boldsymbol{\pi}}_i(t)\,|k\rangle$ with $\hat{\boldsymbol{\xi}}_i(t) = e^{i\beta\hat{S}_0}\hat{\mathbf{x}}_\mathrm{i}(t)e^{-i\beta\hat{S}_0} = \hat{\mathbf{x}}_i(t) + \Delta\hat{\mathbf{x}}_i(t)$ and $\hat{\boldsymbol{\pi}}_i(t) = e^{i\beta\hat{S}_0}\hat{\mathbf{p}}_\mathrm{i}(t)e^{-i\beta\hat{S}_0} = \hat{\mathbf{p}}_i(t) + \Delta\hat{\mathbf{p}}_i(t)$.

In order to extract the QBM frequency from Eq. (5.8) we take its expectation value with respect to the perturbed initial state $|k'\rangle$. We assume that all terms are well defined operator functions and can be Taylor expanded [127]. Then, together with $e^{-i\beta\hat{S}_0}e^{i\beta\hat{S}_0} = \mathbf{1}$, it follows for any term $\hat{\mathbf{O}}$ in Eq. (5.8) that $\langle k'|\,\hat{\mathbf{O}}(\hat{\mathbf{x}}(t), \hat{\mathbf{p}}(t))\,|k'\rangle = \langle k|\,\hat{\mathbf{O}}(\hat{\boldsymbol{\xi}}(t), \hat{\boldsymbol{\pi}}(t))\,|k\rangle$ with $\hat{\boldsymbol{\xi}}(t)$ and $\hat{\boldsymbol{\pi}}(t)$ defined like $\hat{\mathbf{x}}(t)$ and $\hat{\mathbf{p}}(t)$ above.

Equipped with this knowledge, it is now possible to rewrite the expectation value of Eq. (5.8) in terms of eigenstate $|k\rangle$ and operators $\hat{\boldsymbol{\xi}}_i(t)$ and to perform a first order Taylor expansion with regard to $\Delta\hat{\mathbf{x}}_i(t)$ which yields

$$\frac{d^2}{dt^2}\sum_{\mathrm{i<j}}^{N}\langle\{\hat{\mathbf{x}}_{\mathrm{ij}}(t),\Delta\hat{\mathbf{x}}_{\mathrm{ij}}(t)\}\rangle = -4\sum_{\mathrm{i<j}}^{N}\langle\{\hat{\mathbf{x}}_{\mathrm{ij}}(t),\Delta\hat{\mathbf{x}}_{\mathrm{ij}}(t)\}\rangle$$
$$+N\sum_{\mathrm{i<j}}^{N}\langle\{\hat{\mathbf{F}}^{\alpha}_{\mathrm{ij}}(t),\Delta\hat{\mathbf{x}}_{\mathrm{ij}}(t)\}\rangle + \langle\hat{\mathbf{O}}_{\mathrm{res}}\rangle \tag{5.9}$$

where all expectation values are taken with respect to $|k\rangle$, the $\{.,.\}$ denotes the anti-commutator and

$$\hat{\mathbf{F}}^{\alpha}_{\mathrm{ij}}(t) = \left[2-\alpha-\frac{(\alpha+2)a^2}{\hat{\mathbf{x}}^2_{\mathrm{ij}}(t)+a^2}\right]\frac{\alpha\lambda\hat{\mathbf{x}}_{\mathrm{ij}}(t)}{\left(\hat{\mathbf{x}}^2_{\mathrm{ij}}(t)+a^2\right)^{\alpha/2+1}}. \tag{5.10}$$

$\hat{\mathbf{O}}_{\mathrm{res}}$ is a residual term that arises from the non-commuting terms. As this will not play a role in the final result, it is not considered beyond this point.

In order to proceed further, an expression for $\Delta\hat{\mathbf{x}}_{\mathrm{ij}}(t)$ is needed. Since $\Delta\hat{\mathbf{x}}_{\mathrm{i}}(t)$ is a small perturbation, it is reasonable to assume a linear dependence on the $\hat{\mathbf{x}}_{\mathrm{i}}(t)$'s. Using the relation $e^{-i\hat{H}t}e^{i\hat{H}t} = \mathbf{1}$ along with the definition of $\hat{\boldsymbol{\xi}}_{\mathrm{i}}(t)$ above, it is possible to show that $\hat{\boldsymbol{\xi}}_{\mathrm{i}}(t)$ can be written as

$$\hat{\boldsymbol{\xi}}_{\mathrm{i}}(t) = e^{-i\hat{H}t}e^{i\beta\hat{S}(t)}e^{i\hat{H}t}\hat{\mathbf{x}}_i(t)e^{-i\hat{H}t}e^{-i\hat{S}(t)}e^{i\hat{H}t}, \tag{5.11}$$

where $\hat{S}(t)$ is now a function of the $\hat{\mathbf{x}}_{\mathrm{i}}(t)$'s and $\hat{\mathbf{p}}_{\mathrm{i}}(t)$'s. Eq. 5.11 highlights two important properties of $\hat{\boldsymbol{\xi}}_{\mathrm{i}}(t)$. First, it shows that $\hat{\boldsymbol{\xi}}_{\mathrm{i}}(t)$ is a function of the $\hat{\mathbf{x}}_{\mathrm{i}}(t)$'s and $\hat{\mathbf{p}}_{\mathrm{i}}(t)$'s; these enter through $\hat{S}(t)$. Second, $\hat{\boldsymbol{\xi}}_{\mathrm{i}}(t)$ is symmetric under the exchange of any $\hat{\mathbf{x}}_{\mathrm{l}}(t)$ and $\hat{\mathbf{x}}_{\mathrm{m}}(t)$ with $\mathrm{l},\mathrm{m}\neq\mathrm{i}$. The most general linear Ansatz for $\hat{\boldsymbol{\xi}}_{\mathrm{i}}(t)$ that maintains these properties is

$$\hat{\boldsymbol{\xi}}_{\mathrm{i}}(t) = f(t)\hat{\mathbf{x}}_{\mathrm{i}}(t) + g(t)\sum_{\mathrm{j}\neq\mathrm{i}}^{N}\hat{\mathbf{x}}_{\mathrm{j}}(t) + \mathcal{O}(\hat{\mathbf{p}},\hat{\mathbf{x}}^2) \tag{5.12}$$

with $f(t)\approx 1$ and $|g(t)|\ll 1$ being time dependent functions. Using the fact that $\Delta\hat{\mathbf{x}}_i(t) = \hat{\boldsymbol{\xi}}_i(t) - \hat{\mathbf{x}}_i(t)$, Eq. 5.12 can be rewritten as

$$\Delta\hat{\mathbf{x}}_{\mathrm{i}}(t) = \varepsilon(t)\hat{\mathbf{x}}_{\mathrm{i}}(t) + Ng(t)\hat{X}(t) \tag{5.13}$$

where $\varepsilon(t) = f(t) - g(t) - 1$ and $\hat{X}(t)$ is the CM operator defined above.

After inserting Eq. (5.13) into Eq. (5.9) all expectation values contain functions $h(\hat{\mathbf{x}}(t),\hat{\mathbf{p}}(t))$. By using the Taylor expansion in conjunction with the identity relation above, we find that $\langle h(\hat{\mathbf{x}}(t),\hat{\mathbf{p}}(t))\rangle = \langle h(\mathbf{x},\mathbf{p})\rangle$; all expectation values are constant in time and depend on the initial space and momentum operators. With this, Eq. (5.9) simplifies to

$$\sum_{\mathrm{i<j}}^{N}\langle\mathbf{x}^2_{\mathrm{ij}}\rangle\ddot{\varepsilon}(t) = \sum_{\mathrm{i<j}}^{N}\left[-4\langle\mathbf{x}^2_{\mathrm{ij}}\rangle + N\langle\hat{W}^{\alpha}_{\mathrm{ij}}\rangle\right]\varepsilon(t) \tag{5.14}$$

where $\hat{W}^{\alpha}_{\mathrm{ij}} = \hat{\mathbf{F}}^{\alpha}_{\mathrm{ij}}\cdot\hat{\mathbf{x}}_{\mathrm{ij}}(t)$ with $\hat{\mathbf{x}}_{\mathrm{ij}}(t)$ replaced by $\mathbf{x}_{\mathrm{ij}}$. The solution of Eq. (5.14) is a sinusoidal function with breathing frequency

$$\omega_\alpha = \left[4-\frac{\langle\hat{W}_\alpha\rangle}{2\langle\hat{U}_{\mathrm{rel}}\rangle}\right]^{1/2} \tag{5.15}$$

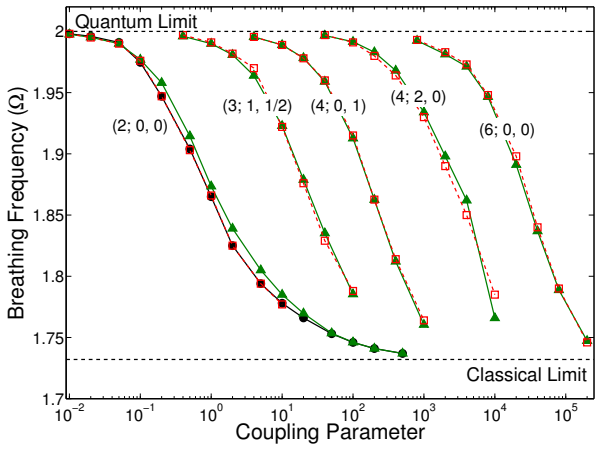


**Figure 5.1.** Breathing frequency versus electron correlation parameter $\lambda$, as determined by (i) difference coordinate solution of the TDSE (•), (ii) Eq. (5.15) (▲) and (iii) MCTDHF (□) for $N = 2$, 3, 4, 6. The origin of the curves have been shifted to make the plot clearer.

where $\hat{W}_\alpha = \sum_{i<j} \hat{W}_{ij}^\alpha$. Note that the expression in Eq. (5.15) is correlated and requires knowledge of the two-body density to evaluate the expectation value. The second term in Eq. (5.15) can be interpreted as the ratio of work done by the particle pairs to the relative coordinate contribution of the trap energy.

## 5.3 Numerical Results and Discussion

The derivation leading to Eq. (5.15) is based on a linear expansion and accurate to $\mathcal{O}(\hat{\mathbf{p}}, \hat{\mathbf{x}}^2)$. Its quality needs to be assessed by a comparison to exact solutions of the time dependent Schrödinger equation (TDSE); here this is done for a 2D QD. N electrons, interacting via the Coulomb potential ($\alpha = 1$), are confined by a harmonic trap with frequency $\Omega$. These systems are particularly challenging due to their long range interaction. The coupling parameter for this system is given by Eq (5.4). For $N = 2$ it is possible to obtain an exact solution by separating the TDSE into CM and difference coordinates [118]; however, for $N > 2$ a direct integration of the TDSE is not possible. As such, the calculations will proceed in the following manner: (i) For $N = 2$ a solution of the TDSE in difference coordinates and one using MCTDHF for $0.01 \leq \lambda \leq 10$ will be obtained. (ii) For $N = 3$, 4 and 6 the TDSE will be solved using MCTDHF for $0.02 \leq \lambda \leq 5$. All results for $N = 2-4$, 6 will be compared to those obtained from Eqn. (5.15). Upon assessing the validity of Eqn. (5.15), it will be used to extend the $N = 3$, 4, 6 calculations to $\lambda > 5$.

All calculations are performed using the Hamiltonian above with $a = 0.1$ and $\alpha = 1$. For MCTDHF, the $n$ spin orbitals are calculated on a 2D grid with 192 points in the range $\pm 15 l_0$ along each axis. The wavefunction is built from a sum over $\binom{n}{N}$ Slater determinants. The number of spin orbitals is increased with $\lambda$ to account for the stronger correlation. We let $n$ range from $n = 20$ for small $\lambda$ to $n = 42$ for the largest $\lambda$ values. Further, the initial wavefunction is determined by imaginary time propagation. Finally, the breathing mode is excited as in reference [118] and is calculated by examining the spectrum of $\langle \hat{U}(t) \rangle$. The uncertainty on all values is determined by the frequency spacing in the spectrum; these lie in the range $1-4\times10^{-3}$. The longest calculations

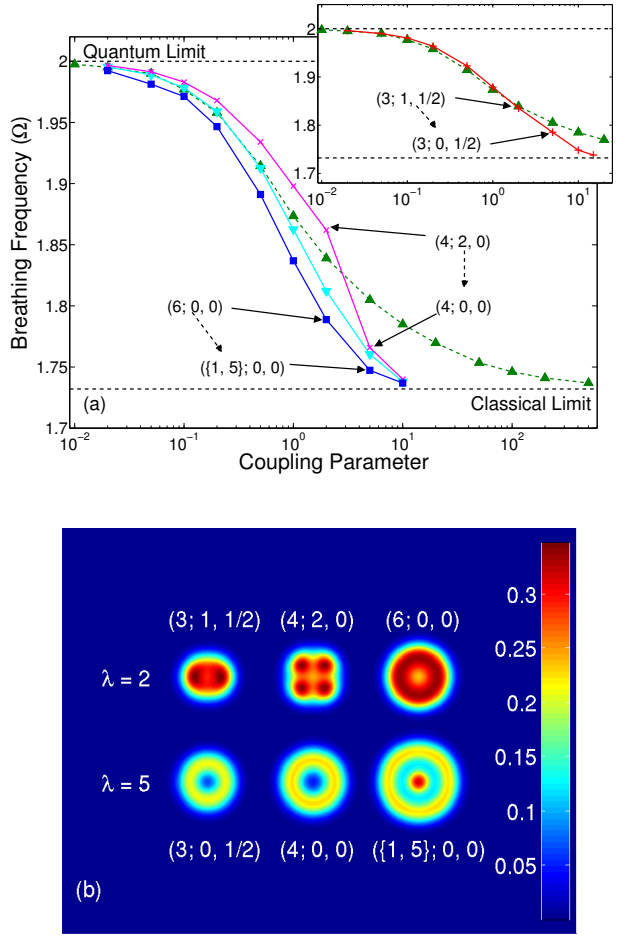


**Figure 5.2.** (a) Breathing frequency versus $\lambda$, as determined by Eqn. (5.15), for (2; 0, 0) (▲) , (4; 0, 1) (▼), (4; 2, 0) (×), (6; 0, 0) (■). The inset shows (3; 1, 1/2) (+) as compared to (2; 0, 0). (b) Densities for states undergoing transitions with increasing $\lambda$.

take up to four weeks running on a single Intel quad core processor.

In Figure 5.1, the breathing frequency is compared for the three approaches. The following notation is used. The electron density consists of different concentric rings; see Ref. [93]. When only a single ring is present, we use $(N; L, S)$ to characterize the eigenstate, where $N$, $L$, and $S$ refer to electron number, total angular momentum and total spin. In the case of two concentric rings the more detailed characterization $(\{N_1, N_2\}; L, S)$ will be used. Here, $N = N_1 + N_2$, with $N_1$, $N_2$ referring to the number of electrons in the inner and outermost rings, respectively. Higher concentric rings are not populated for the states investigated here. The states shown in Fig. 5.1 are characterized by $(2; 0, 0)$, $(3; 1, 1/2)$, $(4; 0, 1)$, $(4; 2, 0)$, and $(6; 0, 0)$ for small $\lambda$ and are consistent with those in Ref. [128]; the curves are staggered in plot for the sake of clarity. The selected states are a representative sample of the types of configurations that can be found in a QD. These include zero and non-zero $L$ and $S$ values, integer and half-integer $S$ values, as

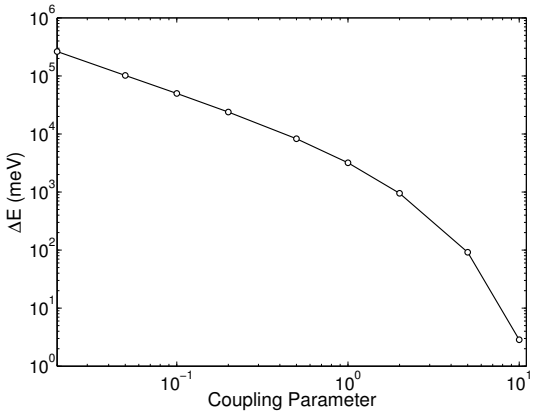


**Figure 5.3.** Difference in energy $\Delta E$ between (4; 2, 0) and (4; 0, 1) as a function of $\lambda$.

well as, filled and partially filled shells. In addition, some states go through level crossings and symmetry transformations as $\lambda$ increases.

The difference between the direct solution of the TDSE and MCTDHF is below the symbol resolution, validating MCTDHF. The operator approach is substantiated by the good agreement of Eq. (5.15) with MCTDHF for all investigated states and values of $\lambda$ used in Fig. 5.1. The validity of Eq. (5.15) for such a diverse range of configurations indicates that it will also be valid for $N > 6$.

Fig. 5.2(a) shows $\omega_1$, as determined by Eq. (5.15), plotted versus $\lambda$. Here Eq. (5.15) has been used to extend the $N = 4$, 6 calculations to $\lambda = 10$ and the $N = 3$ calculation to $\lambda = 15$. The transition to the classical limit is faster with increasing $N$; for $N = 2$ this limit is reached for significantly larger $\lambda$ than for $N > 2$. The manner by which these states approach the classical limit is different depending on the $L$-value. For states with $L = 0$ near the quantum limit, the curves for larger $N$ lie below those with smaller $N$. For states with $L \neq 0$ near the quantum limit, this is not the case. It can be seen from Fig. 5.2(a) (and its inset) that the curves for both (3; 1, 1/2) and (4; 2, 0) lie above the $N = 2$ curve for smaller $\lambda$. As $\lambda$ increases these curves eventually cross the $N = 2$ curve. The resulting change in the pitch of the curve presents diagnostic information about L-value transitions during level crossings. Since the rotational energy increases with $L$ as $\sim L^2/R^2$ [128], $R$ being the size of the dot, we posit that these crossings are indicative of a lowering of rotational energy as the system approaches crystallization. We also note that the $N = 6$ state undergoes the transition (6; 0, 0) $\rightarrow$ ({5, 1}; 0, 0) as it approaches the classical limit. The QBM does not appear to be sensitive to transitions between states with different radial density distributions. The densities for states undergoing transitions are shown in Fig. 5.2(b).

As a final point, although we have worked with a pure eigenstate so far, Eq. (5.15) is generalized to account for finite temperatures by evaluating the expectation values with regard to a sum over all eigenstates multiplied with a quantum statistical weighting factor. In Fig. 5.3, the energy difference between the $N = 4$ ground and excited states is plotted versus $\lambda$. From this plot we can infer when finite temperature effects in the breathing mode have to be expected. At room temperature, the thermal energy becomes equal to the energy spacing around $\lambda = 10$. However, in this range the breathing frequencies of ground and first excited state are close; therewith, $\omega_1$ will not exhibit much difference in the range between zero and room temperature.

An increasingly pronounced temperature dependence will manifest at higher temperatures.

# PART 2

# PROBLEMS IN STRONG-FIELD PHYSICS

# Chapter 6

# Signatures of bound-state assisted nonsequential double ionization

*S. Sukiasyan, C. McDonald, C. Van Vlack, C. Destefani, T. Fennel, M. Ivanov and T. Brabec, Phys. Rev. A **80**, 013412 (2009).*

## 6.1 Introduction

When atoms and molecules interact with intense laser fields, two electrons can be detached by a correlated mechanism known as nonsequential double ionization (NSDI). Once the first electron is liberated by the laser field via tunneling, it quivers in the field and can recollide with the parent ion. Energy exchange with the remaining bound electrons during recollision, assisted by the laser, causes ionization of a second and possibly further electrons. NSDI is a special case of intense field assisted electron impact ionization, with the difference that the rescattering electron is created by tunnel ionization, and therewith its trajectory is phase-locked to the laser field. This allows the use of sophisticated diagnostic tools [13, 25, 129–136] that are key to unravelling the dynamics driving NSDI and laser assisted electron impact ionization in general, a phenomenon that pervades many areas of physics, from atomic and molecular physics to plasma and condensed matter physics.

NSDI can occur by direct impact ionization to the continuum, or via intermediate ionic excited states. Correlated electron spectra can only be partially explained by direct impact ionization, pointing to the importance of excited states [13, 130]. While progress has been made on understanding the direct ionization channel [25,133–136], not much is known about the role of excited states. This lack of knowledge is mostly due to two theoretical challenges. First, modelling of the excited-sate collision dynamics requires numerical integration of the time-dependent few-electron Schrödinger equation in an intense IR field, which is currently beyond reach [25]. Second, there exist no tools to identify and analyze the signature of excited states in numerical and experimental data, such as in correlated spectra.

Here, progress is reported on both challenges. The first progress is of numerical nature. Calculation of correlated electron spectra requires knowledge of the complete wavefunction and therefore the required simulation volume expands with time, the resulting memory requirements make an expansion of the wavefunction in a lower dimensional basis indispensable [25]. This can be done efficiently by the multiconfiguration time-dependent Hartree (MCTDH) method [44] optimized for NSDI. The method is tested on a two-electron diatomic model molecule with one $(2 \times 1D)$ and two $(2 \times 2D)$ dimension per electron. Convergence to the exact integration of the Schrödinger equation is demonstrated. While existing approaches require large scale computers, even for $2D$ systems, this method is feasible on a single processor machine. This opens a promising new avenue for for the numerical integration of the time-dependent few-electron Schrödinger equation.

Second, a semiclassical NSDI model, in which the laser dressed ionic states (resonances) are determined by complex scaling [137], is developed. This method allows for the identification of of signatures of excited ionic states involved in the correlated electrons spectrum of the model molecule. It also allows for the retrieval of specific states involved in NSDI. Analysis demonstrates an interplay between the first two ionic excited states and weakly bound Rydberg states during NSDI. The laser field increases the binding energies of the highly excited states, turns them into quasi-continuum resonances, and brings some of them into the vicinity of the first two excited states. Due to coupling between these states an ionization channel is formed, where efficient impact excitation take place via tightly localized components of the first two excited states, while efficient ionization occurs via the quasi-continuum resonances.

## 6.2 Quantum mechanical theory

The TDSE is solved for the two-electron Hamiltonian

$$H = \sum_{i=1}^{2} [T_i + \mathbf{r}_i \cdot \mathbf{F} + V(\mathbf{r}_i)] + H_2(\mathbf{r}_1, \mathbf{r}_2), \tag{6.1}$$

where $\mathbf{r} = (x, y)$ is the 2D space vector, $T$ is the kinetic energy operator, $\mathbf{r} \cdot \mathbf{F}$ represents the laser electron dipole interaction, and $V = -1/\sqrt{(x \pm R/2)^2 + y^2 + a^2}$ is the potential of the nuclei positioned at $(\pm R/2, 0)$. The two-body part is given by

$$H_2 = 1/\sqrt{(\mathbf{r}_2 - \mathbf{r}_1)^2 + a^2}\,, \tag{6.2}$$

where $a$ is the Coulomb softening parameter. The softening parameter is chosen to make the one and two electron binding energies of the model system match the binding energies typical for diatomic molecules with a $\sigma^2$ configuration, such as $N_2$ and $H_2$.

The propagation is performed by the multi-configuration time-dependent Hartree (MCTDH) method, which uses the expansion of the wavefunction in variationally optimized time-dependent basis functions [44]. The efficiency of the analysis relies on the choice of one-dimensional basis functions, $\varphi_j^{(f)}(x_f, t)$, which for the 4D wavefunction $\Psi$ yields

$$\Psi(x_1, y_1; x_2, y_2, t) = \sum_{j_1=1}^{n_1} \cdots \sum_{j_4=1}^{n_4} B_J(t) \varphi_{j_1}^{(1)}(x_1, t)\, \varphi_{j_2}^{(2)}(y_1, t)\, \varphi_{j_3}^{(3)}(x_2, t)\, \varphi_{j_4}^{(4)}(y_2, t). \tag{6.3}$$

Here, $B_J(t)$ are the time dependent expansion coefficients, where $J = j_1, j_2, j_3, j_4$ labels the expansion functions; the number of expansion functions is set such that $n = n_1 = n_2 = n_3 = n_4$. This choice of basis avoids the necessity to deal with higher-dimensional functions; it trades the large number of grid points of higher-dimensional basis functions $\varphi_j$ against a large size of the configuration vector, $B_J(t)$. For the model system, this choice, combined with an efficient propagation algorithm (see [44]) and efficient treatment of the Hamiltonian (described below), leads to a computational performance that allows the calculation to be performed on a single processor machine.

The equations of motion for $B_J(t)$ and $\varphi_j^{(f)}(x_f, t)$ are derived from the variational principle, see sections 2.2 and 3.1 in Ref. [44]. The system begins in a singlet (ground) state, calculated by imaginary time propagation. The spin remains conserved and is factored out. Atomic units (a.u.) are used throughout.

The numerically most critical issue is the treatment of electron-electron interaction, particularly the calculation of the matrix elements in the bases of 1D functions. An efficient method to perform this task uses the expansion

$$H_2(x_1, y_1; x_2, y_2) = \sum_i v_i(x_1 - x_2)\, u_i(y_1 - y_2) \ , \tag{6.4}$$

in the basis of natural potentials $v_i(x_1 - x_2)$ and $u_i(y_1 - y_2)$ [138], [44] (Sec. 6.1). Usually only a few terms in Eq. (6.4) are needed to achieve high accuracy. This expansion yields matrix elements of the type

$$\langle \varphi^{(1)}_{j_1}(x_1)\varphi^{(2)}_{j_2}(x_2) \mid v_i(x_1 - x_2) \mid \varphi^{(1)}_{l_1}(x_1)\varphi^{(2)}_{l_2}(x_2)\rangle. \tag{6.5}$$

Even though these integrals are still 2D, their form allows an efficient evaluation. First the integral is calculated over one of the coordinates in Eq. (6.5) using the convolution theorem and fast Fourier transform. The remaining 1D integral is evaluated by regular integration. As a result, evaluation of the 4D integral is reduced to a numerical operation that scales almost linearly with the number of grid points in one space dimension.

The total simulation interval is $\pm x_b, \pm y_b$ with $x_b = y_b = 200$, the grid spacing is 0.7 (570 points in each dimension). To increase the efficiency of the calculation we reduce the range of the Coulomb potentials to $\pm 100$ for each coordinate. The cutting of the Coulomb potentials does not influence the final results. A grid spacing of 0.7 is sufficient to converge the simulation. This has been verified by a comparison to calculations with a smaller grid spacing of 0.33. The use of fairly coarse grids is possible because the Coulomb potentials are softened, and because a high numerical accuracy is achieved by the FFT based calculation of the kinetic energy operator and of the electron-electron interaction.

The laser electric field is linearly polarized, $\mathbf{F}(t) = \hat{x}F(t)$, with $F(t) = -\dot{A}(t)$ and with the vector potential $A(t) = F_0/\omega \sin^2(\pi t/T)\sin(\omega t)$ for $-T/2 \le t \le T/2$ and $A(t) = 0$ otherwise. The pulse duration is $T = 2T_0$, where $T_0 = 2\pi/\omega = 110.23$ ($T_0 = 2.6$fs, $\lambda = 0.8\mu$m) is the optical cycle. The simulation interval extends from $-T_0 \le t \le t_f = 140$, and $F_0 = 0.075$ ($I = 2 \times 10^{14}$W/cm$^2$).

To show convergence of our approach, we have first performed runs for a 2×1D diatomic molecule, for which the 2D Schrödinger equation can be integrated exactly. The parameters for this calculation are given in the caption of Fig. 6.1. In Fig. 6.1(a)-(c) the two electron wavefunction is shown for $n = 8, 15, 20$ basis functions. Figure 6.1(d) shows the wavefunction obtained from a split-step integration of the 2D Schrödinger equation. For $n = 20$, the exact wavefunction is well reproduced.

For the 2x2D model molecule we have also performed calculations for $n = 20, 26, 29$ basis functions. The difference between $n = 26$ and $n = 29$ is small, proving convergence. The calculations take $18, 72.8$ and $108.4$ hours on a Xeon 3.0 GHz single core (X5450), respectively. Convergence of the calculation with respect to the number of configurations is further corroborated by diagonalizing the reduced density matrix [44] (Sec. 3.3). Its eigenvalues are the populations of the so-called natural orbitals (the eigenstates of the reduced density matrix.) For $n = 29$ the lowest eigenvalue remains below $10^{-6}$ at all times.

In Fig. 6.2(a) the correlated two electron continuum spectrum is plotted as a function of the electron velocity components parallel to the laser polarization axis, $v_1, v_2$. The spectrum is obtained by removing one- and two-electron bound states by applying the filter $[1 - G(\mathbf{r}_1)][1 - G(\mathbf{r}_2)]$ on $\Psi$ with $G(\mathbf{r}) = \exp[-(\mathbf{r}/d)^6]$. In the range $5 \le d \le 14$, changes in 6.2(a) in the range $-1.1 \le v \le -0.3$ are found to be small. The spectrum for $v > -0.3$ changes due to cumulative damping of bound states with increasing $d$. After filtering, $\mid \Psi \mid^2$ is integrated over $y_1$ and $y_2$,

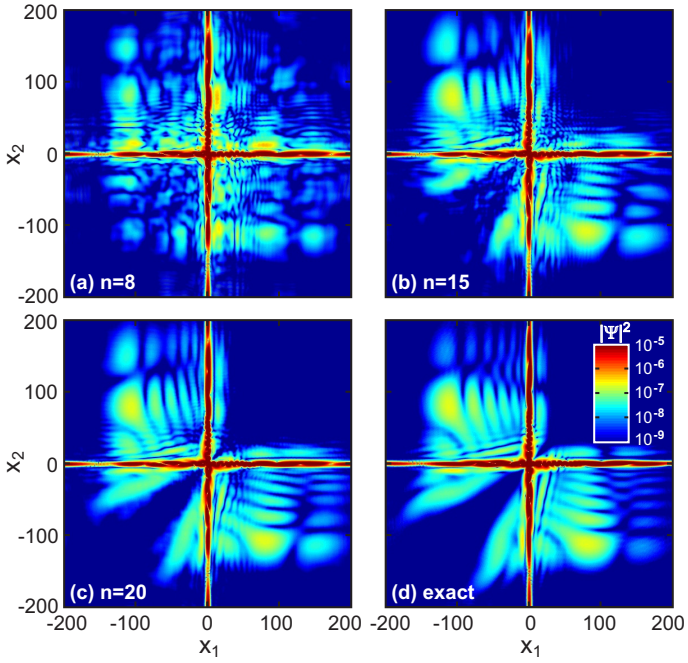


**Figure 6.1.** Wavefunction of a two electron model molecule in an intense laser field with one dimension per electron (2×1D). The Coulomb softening parameter $a = 1.12$ reproduces the $N_2$ ionization potential of 15.8 eV and the two-electron binding energy of 47.1 eV at the $N_2$ equilibrium internuclear distance of $R = 2.08$. Panels (a-d) show $|\Psi|^2$ after the laser pulse at $t = 115$; we chose the range of values for $|\Psi|^2$ to resolve the double ionization part. (a-c) MCTDH results with $n = 8, 15, 20$ basis functions per dimension, respectively; (d) exact numerical integration of the Schrödinger equation.

followed by a Fourier transform of the remaining coordinates, $x_{1,2} \to v_{1,2}$. To extract the physics underlying the modulated structures that appear for $-1.1 \leq v \leq -0.3$, we introduce a simple semi-classical model. The resulting spectrum is plotted in 6.2(b).

## 6.3 Semiclassical model

In the semi-classical model [133] first, the weakest bound electron is tunnel ionized. We tag this electron with index 1 and the remaining bound electron with index 2. At each birth time $t_b$, a trajectory weighted with the ionization probability is launched; the total number of trajectories launched is $M = 2T_0/\Delta t_b = 16000$, with $\Delta t_b$ the step size. The trajectories are propagated classically, by solving $\ddot{x}_1 = F(t)$ subject to the initial conditions $x_1(t_b) = 0$ and $v_1(t_b) = 0$. The time of recollision with the parent ion, $t_r(t_b)$, is obtained from the equation $x_1(t_r) = x_1(t_b) = 0$, and plotted as the full (blue) line in Fig. 6.3(b). For the ultrashort two-cycle pulse used here, only the first return contributes. The recollision velocity and energy of electron 1 are given by $v_1(t_r) = A(t_r) - A(t_b)$, and $E_1(t_r) = v_1^2(t_r)/2$, see the dashed (green) line in Fig. 6.3(b). The laser electric field and vector potential are the full (blue) and the dashed (green) line in 6.3(a), respectively.

Impact excitation occurs, when the recollision energy exceeds the ion excitation energy,

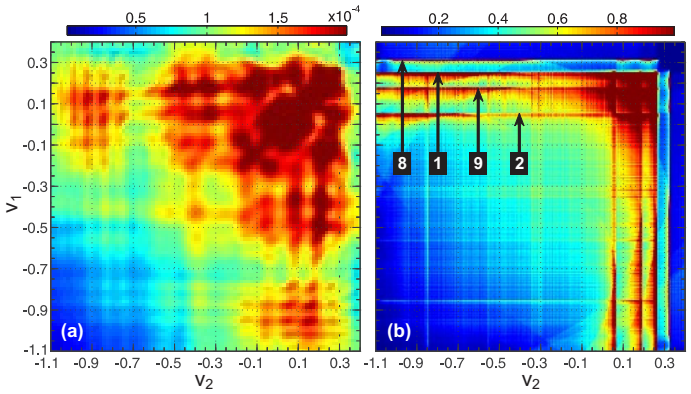


**Figure 6.2.** 2×2D model diatomic molecule; two-electron continuum spectrum integrated over perpendicular $v$-components versus velocities of electrons 1 and 2 parallel to the laser electric field (and molecular axis); for parameters, see text. (a) MCTDH calculation using $n$=26 basis functions; (b) semi–classical calculation. The numbers 1,2,8,9 indicate the spectral lines associated with the transitions from ionic ground state to corresponding excited states of the ion.

$E_1(t_r) \geq \Delta W_i(F(t_r))$. Here $\Delta W_i(F) = W_i(F) - W_0(F)$; $W_i(F)$ is the laser dressed binding energy of the $i$-th excited state, $\mid i\rangle$; $i = 0$ refers to the ground state; $W_i(F)$ for $i \leq 9$ have been calculated by smooth exterior complex scaling [137]. Similar calculations of laser dressed excited states have been done for $H_2^+$ [139] and $H_2$ [28]. The diabatic energy curves of $|0, 1, 2, 8, 9\rangle$ are depicted in Fig. 6.4 as a function of the electric field $F$. The field dependence of the individual states is traced by connecting the eigenvalues of two adjacent field values with the largest eigenfunction overlap. States $|0, 1, 2\rangle$ remain in the perturbative regime and exhibit the typical $F^2$ Stark shift dependence. Eigenfunctions $|i > 2\rangle$ show the close spacing typical of Rydberg states. For $F > 0.01$ the Rydberg states start to mix and cross, and most of them become quasi-continuum states due to a suppression of the Coulomb barrier. The Rydberg states cross and couple with the bound states $|0, 1, 2\rangle$ at various field strengths. Because of the high density of states we show here only $|8, 9\rangle$, which are of direct relevance to the analysis of Fig. 6.2(a).

There is mainly one time interval, $-50 \leq t_b \leq -40$ and $0 \leq t_r \leq 30$, where collisional excitation can happen, see 6.3(b). Further, the highest return energy, $E_1 = 1.04$ ($t_b = -47$, $t_r = 19$) is smaller than the ion ground state binding energy, $W_0 = -1.14$. As a result, direct double ionization to the continuum is negligible, so that efficient NSDI must rely on ionic excited states.

For each impact excitation event a sub-trajectory is spawned, weighted with unity probability. Impact excitation probability and subsequent ionization dynamics of electron 2 will be investigated below. During impact, the energy of electron 1 is reduced to $E_1(t_r) - \Delta W_i(F(t_r)) = u_1^2(t_r)/2$, with $u_1(t_r)$ the velocity after the energy exchange. Solution of the equation of motion for the initial condition $\dot{x}_1(t_r) = u_1(t_r)$ gives the final velocity $v_1(t_f) = u_1(t_r) - A(t_r)$. The final velocities of electron 1 for excitation of electron 2 to excited states $\mid 1, 2, 8, 9\rangle$ as a function of $t_b$ are plotted in Fig. 6.3(d). Their maximum is at $v_1(t_f) = 0.25, 0.05, 0.17, 0.31$, respectively. It has been verified that neglect of the ion Coulomb potential in the model does not notably shift the position of these peaks. Panel 6.3(c) shows $\Delta M/\Delta v_1$, the number of trajectories ending up in a velocity interval between $v_1(t = t_f, t_b)$ and $v_1(t = t_f, t_b) + \Delta v_1$. The plots in Fig. 6.3(c)

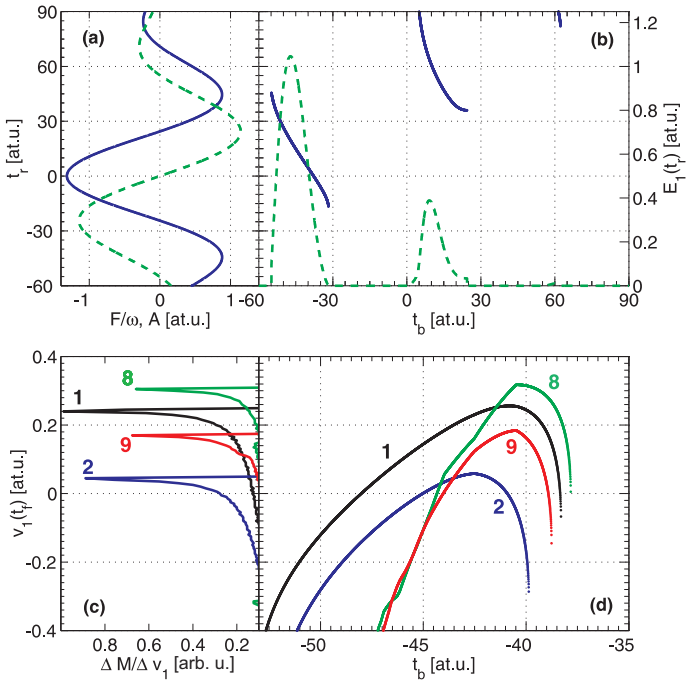


**Figure 6.3.** Panel (a), laser electric field divided by center frequency (full, blue line), and vector potential (green, dashed line) versus time. Panels (b)-(d) characterize the dynamics of the weakest bound electron 1. Panel (b), electron recollision time $t_r$ versus birth time $t_b$ (full, blue line); electron recollision energy versus birth time (dashed, green line). Panel (c), number of electron trajectories $\Delta M$ in the velocity interval between $v_1(t_f)$ and $v_1(t_f) + \Delta v_1$ at final time $t_f$ after the laser pulse. Panel (d), final velocity of electron 1, $v_1(t_f)$, versus birth time $t_b$.

show a pronounced peak around the maximum final velocity in Fig. 6.3(d).

The positions of the classical peaks agree well with the part of the quantum spectrum 6.2(a) with $v_1 > v_2$, which corresponds to labelling the recolliding and bound ionic electron as 1 and 2, respectively. Due to exchange symmetry, the other half of the spectrum ($v_1 < v_2$) is identical, with the roles of electrons 1 and 2 interchanged. The spectrum in Fig. 6.2(a) shows a modulated structure along $v_1$ and $v_2$. We focus on the modulation along $v_1$. The position of the modulation maxima remains constant for $-1.1 \leq v_2 \leq -0.7$ and agrees well with the peaks in Fig. 6.3(c). For $-0.5 \leq v_2 \leq -0.3$, some of the maxima become more washed out and exhibit a weak $v_2$ dependence. For $v_2 > -0.3$, the modulation is veiled by other contributions. Further, the quantum result exhibits additional maxima at $v_1 = -0.07, -0.15$, which comes from ion excited states $\mid i > 9\rangle$ not included in our analysis. In our semi- classical model, $|i = 3...7\rangle$ have peaks at $v_1(t_f) > 0.3$. Quantum mechanically these peaks do not appear; the reason will be discussed below. Finally, due to the quantum uncertainty, the modulation exhibited by the quantum calculation is shallower and broader than the classical widths.

The modulation observed in spectrum 6.2(a) and its assignment to ionic excited states presents an important step forward towards a complete understanding of NSDI. However, several questions remain still open. A full analysis of 6.2(a) requires modeling the excited state dynamics of electron 2 and its ionization. So far, this is impeded by a lack of theoretical tools. The

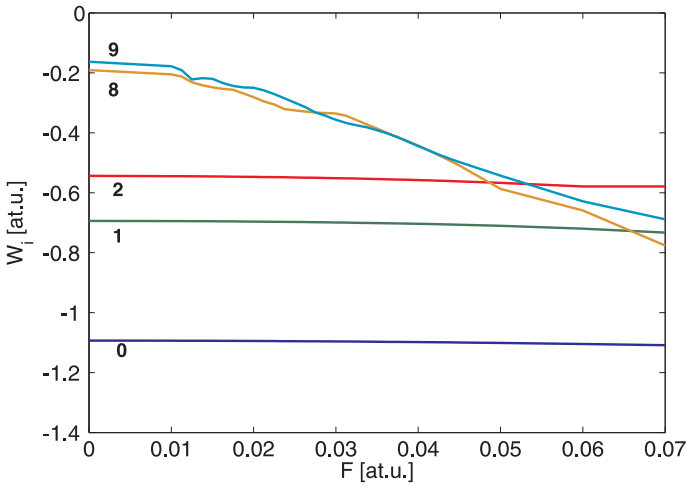


**Figure 6.4.** Real part of binding energy of the first three bound states $|0, 1, 2\rangle$ and of two of the higher excited states $|8, 9\rangle$ of our 2D model diatomic ion versus laser electric field $F$.

intense laser field turns an ionic excited state into a resonance by coupling it to the continuum. The resultant band of continuum states is grouped into a discrete resonance state with complex energy by complex scaling [137], whereby the hermitian Hamiltonian is transformed into a complex symmetric one [137]. The resulting complex norm makes it difficult to assign population probabilities to resonances. In the presence of an intense laser pulse, this is still an unsolved problem [140].

Therefore, only a few qualitative considerations about the ionization dynamics of electron 2 can be drawn here. Figures 6.3(c) and (d) show that collisional excitation is most likely for trajectories born around $t_b \approx -40$, which recollide at $t_r \approx 5$, at an electric field strength $F(t_r) \approx 0.07$, see 6.3(b) and (a). At this high $F$, efficient impact ionization only occurs to states with pronounced bound state components, which are $|1, 2\rangle$, and $|8, 9\rangle$ due to their coupling with $|1, 2\rangle$. States $|3...7\rangle$ are completely embedded in the continuum and are energetically too far away from $|1, 2\rangle$ at $F \approx 0.07$ for notable coupling to occur. This explains their absence in spectrum (a) of Fig. 6.2.

Ionization proceeds via a direct and an indirect channel. Direct ionization of $|8, 9\rangle$ occurs efficiently and practically instantaneously due to the large ionization rates, determined by two times the imaginary part of the resonance energy. Direct ionization from $|1, 2\rangle$ is weak and gives the wrong spectral signature in Fig. 6.2(b). Ionization from $|1, 2\rangle$ is dominated by the indirect channel, where population is first transferred to states $|8, 9\rangle$, as a result of the nonadiabatic intense field dynamics during and after impact excitation, and ionized from there. Note that the energy balance for the direct and indirect excitation channels is different. Whereas electron 1 has to bring up the energy $\Delta W_{8,9}$ for direct excitation, it contributes only the energy $\Delta W_{1,2}$ to the indirect ionization channel. The remaining energy difference is put up by the laser field. Consequently, the direct and indirect channels give a $v_1$-signature in 6.2(a) corresponding to peaks $8, 9$ and $1, 2$ in Fig. 6.3(c), respectively.

From the qualitative discussion we derive the following model assumptions for the dynamics of electron 2. We weight the direct and indirect excitation channels to states $|8, 9\rangle$ equally strong and assume that excitation occurs instantaneously at $t_r$, whenever energetically allowed.

Ionization occurs from states $|8, 9\rangle$ between the time of excitation and the end of the laser pulse, and is calculated from the imaginary part of the resonance energy; the ionization rate is given by two times the imaginary part of the resonance energy. Trajectories for electron 2 are launched with zero velocity at times $t_2 \geq t_r$, yielding the final velocity $v_2(t_f) = -A(t_2)$. Putting these assumptions into our semi-classical model yields the spectrum 6.2 (b). The basic features of the quantum spectrum are reproduced, corroborating our qualitative picture for electron 2.

## 6.4 Conclusion

Finally, this study relies on calculations for a 2x2D model system. It cannot be expected that these calculations predict quantitative features of experimental spectra. However, the principal mechanisms and the qualitative features identified here are of relevance for real world 3D systems. In this sense, this work presents a first step to a deeper understanding of NSDI in real atoms and molecules. The following will discuss how conclusions drawn from this model study apply to real world systems.

A model molecule has been chosen here, having in mind the richer physics than in atoms. For example, bound-state-assisted NSDI offers a possible explanation for the experimental observation that NSDI is different for laser polarizations parallel and perpendicular to the molecular axis [13]. This topic will be pursued in future research.

It should be emphasized that the processes involved in bound state assisted NSDI are universal and hence, are expected to play an important role in a broad range of atoms and molecules. It is expected that 2x2D model atom calculations will show spectral features similar to the one identified in this chapter. In difference to molecules, atoms will exhibit no laser polarization dependence. The specific manifestation of bound state assisted NSDI in individual systems, such as the position of the maxima of the modulated spectral structures observed here, is determined by three factors; (i) the polarizability of the parent ion, (ii) the symmetry of the field-free ionic bound states and (iii) the energy difference between them.

In the case of the present $2 \times 2D$ model molecule, the polarizability and symmetries are comparable to ($\sigma^2$) diatomic molecules, such as $H_2$ or $N_2$. Only the energy spacing between the ionic bound states is larger than in real diatomic molecules. As a result, the $2 \times 2D$ model underestimates the field-induced distortion of the ionic bound states and therefore gives a conservative estimate of the mechanisms identified here. Due to the different energy spacing of the ionic bound states, the model analysis presented here cannot predict the position of the modulated structures in the correlated spectrum of $H_2$ or $N_2$.

The current model cannot resolve differences among $N_2$, $H_2$, and related molecules. However, the quality of the model can be further improved by adding (frozen core) potential terms accounting for the presence of further (core) electrons. Such a model could distinguish between diatomic molecules such as $H_2$ and $O_2$, for which the ground state is fundamentally different. The symmetry and shape of the neutral and ionic bound states strongly influences the whole ionization dynamics. We believe that the improved model would also be capable of reproducing some of the more subtle differences between molecules of same symmetry, such as $N_2$ and $H_2$.

Our work presents a first step toward a complete retrieval of the attosecond electron dynamics involved in NSDI. Here is a road map of what is still missing. Theoretically, a way has to be found to assign population probabilities to complex scaled resonance states. Experimentally, these signatures have to be measured. They emerge for very short pulses and will be increasingly smeared out for longer pulses. Requirements on pulse duration, pulse energy, and carrier-envelope phase stability are stringent, making these experiments challenging [132].

# Chapter 7

# Multielectron correlation in high-harmonic generation: A 2D model analysis

*S. Sukiasyan, C. McDonald, C. Destefani, M. Yu. Ivanov and T. Brabec, Phys. Rev. Lett.* ***102****, 223002 (2009).*

High harmonic generation (HHG) takes place when a gas of atoms/molecules is exposed to an intense laser pulse, yielding harmonics of the incident field with orders up to several hundreds [141]. In addition to being the workhorse for modern attosecond pulse technology [142], HHG offers the potential for resolving fundamental microscopic processes with sub-Å spatial and sub-femtosecond temporal resolution [14, 143, 144].

Applications of HHG to attosecond dynamic imaging and molecular tomography typically rely on the three-step model [133]. An electron is (i) liberated from the highest occupied orbital, (ii) accelerated by the intense laser field, and (iii) emits a harmonic photon upon returning to the parent ion and recombining to the initial bound state of the neutral. This model relies on the single active electron (SAE) approximation, assuming that only the weakest bound electron interacts with the laser field.

The importance and the exact role of multi-electron effects in HHG remain unclear. Already at the coarse level of the frozen-core (FC) approximation, one finds that multi-electron effects are indispensable for the tomographic retrieval of wavefunctions [145–147]. It is clear that exchange and correlation should play a role in HHG [148]. However, little is known both about their importance and the specific ways in which correlation effects manifest themselves. This lack of qualitative and quantitative understanding is a serious bottleneck for applications of HHG to attosecond dynamic imaging [14, 143, 144].

This bottleneck exists even decades after the discovery of HHG due to fundamental difficulties in the analysis of intense field multi-electron dynamics. First, solution of the time-dependent multi-electron Schrödinger equation is beyond reach [29, 149, 150]. Approximate methods, such as the time-dependent Hartree-Fock (TDHF) [151], Frozen-Core (FC) [152], and time dependent density functional theory [153] neglect all or a part of the electron correlation; their accuracy is not controlled. Second, even if the Schrödinger equation is solved, extracting the underlying physical mechanisms from the multi-dimensional wavefunction is a formidable problem in its own right.

We report progress on both of these challenging directions. We solve the time-dependent Schrödinger equation for HHG in a two-electron model diatomic molecule with two spatial dimensions per electron. Our numerical analysis builds on the multi-configuration time-dependent Hartree (MCTDH) method [44]. Optimization of the multi-configuration expansion brings the computational costs down to a level comparable with conventional one-electron calculations and

opens the door to a systematic analysis of multi-electron effects in HHG. With regard to the second challenge, we develop an ionic eigenstate resolved (IER) expansion of the multi-dimensional wavefunction. This allows us to systematically identify and to quantify the physical mechanisms underlying multi-electron effects in HHG.

Multielectron effects arise from (i) electron exchange, (ii) polarization and excitation of the neutral by the laser field, and (iii) polarization and excitation of the ion in the field of the recolliding electron. While the second effect has been considered by [154], the last has been mostly disregarded. We show the interplay between recolliding electron and ion is essential for quantitative modelling of HHG. It may not only enhance [148], but also suppress HHG, depending on the constructive or destructive interference of the harmonic signals generated via channels associated with different ionic states.

Our analysis uses the MCTDH approach [44]. For two electrons in 2D each, we expand the full 4D wavefunction in sums over products of lower dimensional orbitals. In contrast to the conventional Hartree or HF methods, an MCTDH orbital is a mathematical object that does not necessarily represent a single particle. The choice of the orbitals crucially influences the efficiency of MCTDH. We have chosen the expansion orbitals to be 1D functions, $\varphi_j(x,t)$, yielding

$$\Psi(x_1,y_1;x_2,y_2,t) = \sum_{j_1=1}^{n_1}\cdots\sum_{j_4=1}^{n_4} A_{j_1j_2j_3j_4}(t)\varphi_{j_1}(x_1,t)\,\varphi_{j_2}(y_1,t)\,\varphi_{j_3}(x_2,t)\,\varphi_{j_4}(y_2,t) \qquad (7.1)$$

for the 4D wavefunction $\Psi$. Here, $A_{j_1j_2j_3j_4}(t)$ are the expansion coefficients, and $n_1$, $n_2$, $n_3$, $n_4$ represent the number of expansion functions along the coordinates $\mathbf{r}_1 = (x_1, y_1)$ and $\mathbf{r}_2 = (x_2, y_2)$, respectively.

The equations of motion for $A(t)$ and $\varphi_j(x,t)$ are derived from the variational principle, see e.g. [44]. Since our Hamiltonian does not contain spin mixing operators, the initial spin state is conserved and can be factored out. By comparison, in multi-configuration time dependent Hartree Fock (MCTDHF) [57], the spin is the part of the expansion orbitals and remains in the calculation. We start with the singlet state, for which the spatial part of the wavefunction $\Psi$ is symmetric. This symmetry is preserved during propagation. The initial (ground) state is calculated by imaginary time propagation [44].

Our model system uses soft-core Coulomb potentials for both nuclear-electron and electron-electron interactions, $V(x,y) \propto (x^2+y^2+a^2)^{-1/2}$. The soft-core parameter $a = 0.64$ is chosen to reproduce the $N_2$ ionization potential of 15.8 eV and the two-electron binding energy of 46.5 eV. Two nuclei (Z=1) are held fixed at the $N_2$ equilibrium internuclear distance of $R = 2.08$ a.u.. The laser field is linearly polarized, $E(t) = E_0 \sin^2(\pi t/T)\cos(\omega t)$, with a peak intensity of $10^{14}$ W/cm$^2$, a wavelength of 800 nm, and a pulse duration $T = 10T_0$, where $T_0 = 2\pi/\omega = 2.6$fs. A grid spacing of 0.4 a.u. is sufficient.

One of the critical issues is calculating the matrix elements of the electron-electron interaction. The expansion

$$\begin{aligned} V_{ee}(x_1,y_1;x_2,y_2) &= \frac{1}{\sqrt{(x_1-x_2)^2+(y_1-y_2)^2+a^2}} \\ &= \sum_{i=1}^{n} v_i(x_1-x_2)\,u_i(y_1-y_2) \end{aligned} \qquad (7.2)$$

in the basis of natural potentials $v_i$ and $u_i$ [44], yields matrix elements of the type $\langle\varphi_{j_1}(x_1)\varphi_{j_2}(x_2) \mid v_i(x_1-x_2) \mid \varphi_{l_1}(x_1)\varphi_{l_2}(x_2)\rangle$. Using the convolution theorem combined with the fast Fourier transform results in a nearly linear scaling with the number of grid points.

We use an absorbing potential of the form $W(x) = -i\eta(|x| - x_c)^3$ in each coordinate for $|x| \geq x_c$, with $\eta = 0.0005$. For our laser parameters, we use $x_c = 16$ au. to absorb the so-called "long" trajectories while keeping the short trajectories intact, which dominate experimental harmonic spectra [141]. Convergence of the calculation with respect to the number of configurations is determined by diagonalizing the reduced density matrix [44]. Its eigenvalues are the populations of the so-called natural orbitals (the eigenstates of the reduced density matrix.) For $n_1$=$n_2$=$n_3$=$n_4$=15 the lowest eigenvalue remains below $10^{-6}$ at all times. A HHG calculation takes below 4 hours on a single core Intel 3.0 GHz CPU.

To analyze the role of the multi-electron dynamics in HHG, we introduce the method of ionic eigenstate-resolved (IER) wavefunctions. The IER wavefunctions are determined by projecting the exact $\Psi(\mathbf{r}_1, \mathbf{r}_2, t)$ onto the complete set of the ionic eigenstates $\psi_k(\mathbf{r}_2)$, i.e.

$$\phi_k(\mathbf{r}_1, t) = \langle \psi_k(\mathbf{r}_2) \mid \Psi(\mathbf{r}_1, \mathbf{r}_2, t) \rangle. \tag{7.3}$$

After symmetrization with respect to the electrons we obtain

$$\Psi_M(\mathbf{r}_1, \mathbf{r}_2, t) = \sum_{k=1}^{M} \Big[ \phi_k(\mathbf{r}_1, t)\psi_k(\mathbf{r}_2) + \psi_k(\mathbf{r}_1)\phi_k(\mathbf{r}_2, t) \Big] \tag{7.4}$$

with $M$ the number of ionic eigenstates. The binding energies of the first four ionic states are -31eV, -20.4eV, -15eV, and -10.9eV, respectively. As the ionic eigenfunctions $\psi_j$ are contained in $\phi_k$, symmetrization leads to an overcomplete basis, i.e. the terms $\langle \psi_j | \phi_k \rangle \psi_k \psi_j$ with $j = 1, ..., M$ are counted twice. This can be remedied by substituting $\phi_k \to (1 - \hat{P})\phi_k$ in (7.4). The projector $\hat{P} = (1/2) \sum_{j=1}^{M} \mid \psi_j(\mathbf{r}) \rangle \langle \psi_j(\mathbf{r}) \mid$ removes the double counted contributions.

Harmonic spectra are calculated in the acceleration gauge as

$$I_M(\Omega) = 2 \left| \int \left\langle \Psi_M \middle| \frac{\partial V}{\partial x_1} + E(t) \middle| \Psi_M \right\rangle e^{i\Omega t} dt \right|^2 . \tag{7.5}$$

For a systematic analysis of different approximations, we also use

$$I_M^G(\Omega) = 2 \left| \int \left\langle a(t)\Psi_g \middle| \frac{\partial V}{\partial x_1} + E(t) \middle| \Psi_M \right\rangle e^{i\Omega t} dt \right|^2 . \tag{7.6}$$

Here, $a(t) =< \Psi_g \mid \Psi(t) >$, $\Psi_g$ is the two electron ground state, $V$ is the potential of the nuclei, $E(t)$ is the laser electric field, and the factor 2 arises from the electron exchange symmetry. Our analysis is restricted to emission along the laser polarization ($x$-axis). The IER Ansatz $\Psi_M$ describes well the part of the wavefunction with one electron bound and one in the continuum. Thus, it is well suited for analyzing harmonics with energies above $I_p$, i.e. $N > 11$ in our case. Finally replacing $\Psi_M$ with $\Psi$ in Eqs. (7.5) and (7.6) yields the exact spectra, $I$ and $I^G$, respectively.

The meaning of the IER expansion becomes clear when looking at the equations of motion for $\phi_k$. Inserting Eq.(7.4) into the Schrödinger equation and multiplying with $\langle \psi_j \mid$ on the left side yields

$$\begin{aligned} &i\partial_t \phi_j(\mathbf{r}_1, t) + i \sum_k \langle \psi_j \mid \partial_t \phi_k(t) \rangle \, \psi_k(\mathbf{r}_1) = \\ &\sum_k \left[ \langle \psi_j \mid \mathbf{H} \mid \psi_k \rangle \, \phi_k(\mathbf{r}_1, t) + \langle \psi_j \mid \mathbf{H} \mid \phi_k(t) \rangle \, \psi_k(\mathbf{r}_1) \right] . \end{aligned} \tag{7.7}$$

Here **H** is the total 2 electron Hamilton operator and the bracket denotes integration over $\mathbf{r}_2$. Equation (7.7) shows how to extract information on the multi-electron effects by looking at the role of different ionic eigenstates. For $M = 1$, Eq. (7.4) describes the part of the exact wavefunction, where one electron remains in the ionic ground state. It is the closest possible SAE approximation.

There exists no unique definition of correlation. Here we associate it with population exchange between the ground and excited ionic states. In this sense, results, $M = 1$ in Eq. 7.4 exclude correlation; only exchange is present. Note that Eq. (7.4) goes beyond the HF ansatz. Indeed, Eq. (7.7) for $\phi_{j=1}$ includes the coupling to all excites states. TDHF arises by restricting the sums in Eq. (7.7) to a single $k = 1$ term, thus losing any coupling between $\phi_1$ and other $\phi_k$.

Finally, the FC limit is obtained by neglecting the Pauli principle (symmetry) and by dropping the second terms on the left and the right hand sides of Eq.(7.7):

$$i\partial_t \phi_{\rm fc}(\mathbf{r}_1, t) = \langle \psi_1(\mathbf{r}_2) \mid \mathbf{H} \mid \psi_1(\mathbf{r}_2) \rangle \, \phi_{\rm fc}(\mathbf{r}_1, t) \; . \tag{7.8}$$

The harmonic spectra in the FC approximation, $I_{\rm fc}$ and $I^G_{\rm fc}$, are calculated using Eqs. (7.5) and (7.6) with $\phi_{\rm fc}(\mathbf{r}_1, t)$, instead of $\Psi_M$ and $\langle \phi_{\rm fc}(0) | \phi_{\rm fc}(t) \rangle \phi_{\rm fc}(0)$ instead of $a(t)\Psi_g$. The prefactor 2 in Eqs. (7.5) and (7.6) must be omitted.

Fig. 7.1 shows the harmonic spectrum (a, b), the ratio of the FC harmonic yield $I_{\rm fc}$ to the exact harmonic yield $I$ (c, d), and $I_M/I$ for $M$=1,2,4 (e, f). The molecular axis is aligned along the laser electric field, i.e. $\theta = 0°$. The left and right panel show the results for Eqs. (7.5) and (7.6), respectively. A notable qualitative difference between the two spectra (a, b) occurs for the harmonics between 19 and 23. The suppression in this range in Fig. 7.1(b) is due to the two-center interference [151]. In Fig. 7.1(a) the two center interference is masked by the polarization of the neutral ignored in Eq. (7.6). The difference of up to a factor of 30 between (a) and (b) clearly shows that laser induced polarization of the neutral molecule plays an important role in HHG.

For the FC calculation, $I_p$ has been adjusted to that of the two-electron system by adjusting the soft-core parameters of the Coulomb potentials. Nevertheless, the difference to the exact result is substantial. Close to the two-center interference minimum the difference is up to a factor of 3, 20 in Figs. 7.1(c) and (d), respectively.

The result is substantially improved for the eigenstate-resolved approach with $M$=1 mainly due to accounting for exchange. The maximum difference to the exact result is 1.8 and 4.2 in the range of the two-center interference minimum; see the squares in Figs 7.1(e) and (f), respectively. Similar to the FC limit, agreement is improved for the rest of the spectrum, with a difference between 20% and 40%. The expansion converges quickly with increasing $M$. In $I_2$ (circles), HHG from the first ionic excited state is added, which improves agreement to within 10% of the full result. The contribution of $\psi_3$ is negligible due to symmetry. Adding $\psi_4$ (diamonds) yields almost the full result.

We have also calculated $I_1/I$ and $I^G_1/I^G$ as a function of the alignment angle $\theta$. The maximum difference to the exact result remains in the area around the two-center interference minimum. However, the position of the two-center interference minimum moves to higher harmonics with increasing $\theta$ [151].

Thus, the FC model gives a very coarse approximation to HHG. The ionic state expansion allows us to analyze the key missing components. Starting with the FC limit, first the exchange is added for $M = 1$. Correlation is built in with increasing $M$. For our system, the accuracy of the ground state channel ($M = 1$) is sufficient for many purposes; the contribution of ionic excites states is suppressed by the large energy gap with the ionic ground state. However, for

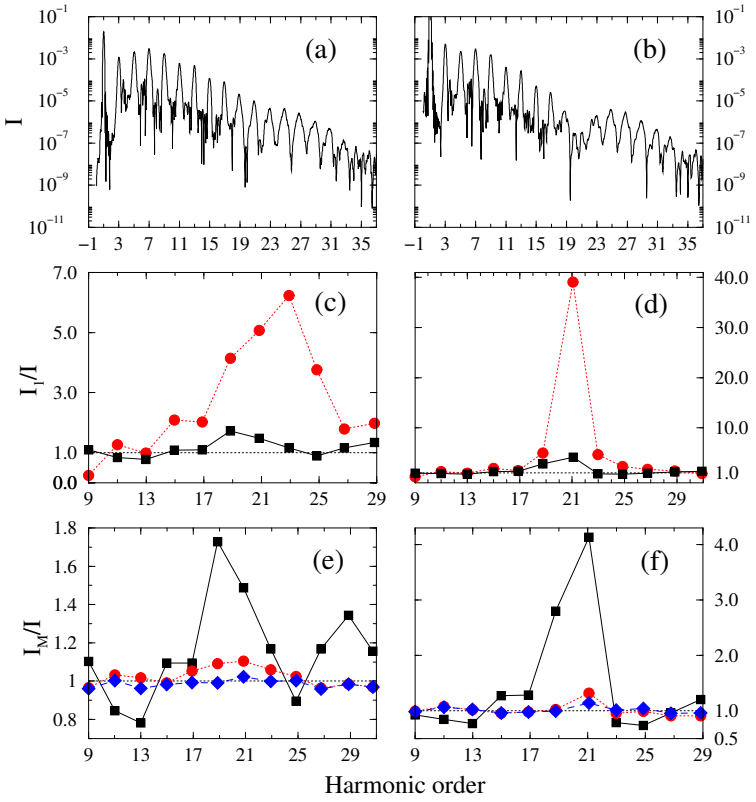


**Figure 7.1.** Converged full harmonic yields, $I$ and $I^G$, calculated by (a) Eq. (7.5), (b) Eq. (7.6); ratio of frozen core to exact harmonic yields, (c) $I_{\rm fc}/I$ and (d) $I^G_{\rm fc}/I^G$ (circles); in the FC calculation $I_p$ was adjusted to match the exact $I_p$; ratio of IER to exact harmonic yields, $I_1/I$ (squares) (e) $I_M/I$ and (f) $I^G_M/I^G$, for $M$=1 (squares), $M$=2 (circles) and $M$=4 (diamonds). The molecule is aligned along the field, $\theta = 0$. $M$ is the total number of ionic state included in the IER expansion 7.4. From FC to $M = 1$ mainly exchange is added. Correlation is systematically built in with increasing $M$.

applications such as HHG-based molecular tomography, which relies on the series of harmonic spectra as a function of $\theta$, an error of about a factor of $2 - 4$ in the region of the two-center interference is significant. This error comes from the part of the correlation ($M \geq 2$) that cannot be captured by the SAE analysis. In larger systems, where correlation and polarizability are usually more pronounced, more significant differences are expected. As a result, understanding of the physical origin of the ionic excited channels in imperative.

Population of the ionic excited states can be caused by the following two mechanisms: (i) laser driven population of two-electron excited states and subsequent decay to ionic ground and excited states during tunnel ionization; (ii) virtual and/or real population transfer from the IGS to the IES, driven by the laser field and/or by the recolliding electron.

The importance of (i) was assessed by projecting the full time-dependent wavefunction on the two-electron eigenstates, which were determined by diagonalization of field-free Hamiltonian. Although two-electron excited states are populated substantially en route to ionization, upon

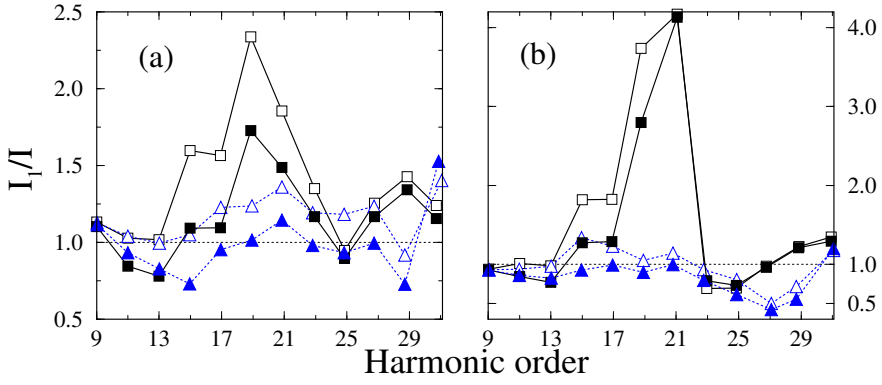


**Figure 7.2.** $I_1/I$ (a) and $I_1^G/I^G$ (b), determined by replacing the field free IGS $\psi_1$ in Eq. (7.4) with the adiabatic laser polarized ionic ground state $\psi_1(E(t))$ (empty squares); as a reference, $I_1/I, I_1^G/I^G$ from Fig. 7.1 (e,f) for the field free IGS is plotted (full squares). The results with corresponding empty and full triangles refer to $\theta = 30°$.

ionization they decay to the ionic ground state. This was verified by repeating the calculation for the above parameters with the individual excited states as initial state. No substantial population of the ionic excited states was found, ruling out mechanism (i) for our system.

Regarding the mechanism (ii), excitations by the laser field can be separated into adiabatic polarization (virtual) and nonadiabatic (real) excitations. Nonadiabatic population transfer occurs, when the energies of the polarized states change too fast for the electron to follow. Simulations of the dynamics in the two level system, consisting of the ionic ground and first excited states, yields the nonadiabatic excitation probability $P_1^+ \approx 9 \times 10^{-5}$. Hence, the nonadiabatic effects are negligible.

To gauge the effect of the adiabatic polarization, we have replaced the field-free ground state $\psi_1$ in the wavefunction (7.4) with the polarized one, $\psi_1(E(t))$, and calculated $I_1/I$ (see Fig. 7.2). While adiabatic polarization is important, it does not generally improve the agreement with the exact result and is not the dominant effect.

Thus, the differences between the laser dressed $I_1$ and $I$ spectra in Fig. 7.2 are due to the real and virtual excitations of the ion by the recolliding electron. Only in this case the harmonic cutoff is unshifted, in agreement with our simulations. The importance of recollision in our model system was further corroborated by calculating the final population of the ionic states after the laser pulse as a function of the laser polarization. The population of the ionic first excited state is a few percent for linear polarization, and drops to zero with increasing ellipticity.

Finally, in our analysis the importance of the various multi-electron effects in our model molecule can be quantified. Here is a summary. The difference between $I$ and $I^G$ in Figs. 7.1(a) and (b) shows that neglect of the polarizability of the neutral system causes a difference by a factor of up to 30. To determine the influence of the other effects we use Eq. 7.6, which does exclude polarization of the neutral groundstate. The difference between $I_{fc}^G$ and $I_1^G$ of up to a factor of 10 is mainly due to the exchange effect. The difference between $I_1^G$ and $I^G$ of up to a factor of 4 is due to correlation. The major fraction of this difference comes from the polarization of the ionic ground state by the returning electron. While the importance of collisional excitations

in double ionization has been understood for over a decade, it has been completely ignored so far in HHG. We expect our conclusions to hold in 3D, since the dimensionality scaling of the recombination and collision probabilities during the recollision are the same.

All of the multi-electron effects identified here will become even more pronounced in extended molecules having higher polarizabilities. This presents a serious challenge for attosecond dynamic imaging of wavefunctions by molecular tomography. Novel theoretical retrieval tools that can account for multi-electron effects are required. One potential path is revealed by our analysis. The fact that only two ionic states in Eq. (7.7) are important in the HHG in our system shows that one can account for essential multi-electron effects by solving several coupled one-electron Schrödinger equations for essential ionic states, leading to dramatic improvement in computational cost.

# Chapter 8

# Extending MCTDHF to nonuniform tensor product grids

The MCTDHF (and MCTDH) calculations have been limited so far to electrons moving in two dimensions using a uniform tensor product grid. The ultimate goal is to use MCTDHF to perform calculations on atoms and molecules with up to 10 electrons moving in three dimensions in the presence of a strong laser field. In order to accomplish this there are two main hurdles to overcome. First, for strongly correlated systems or systems ionizing more than two electrons, a large spin-orbital basis set is required. For number of electrons $f > 6$ the number of configurations becomes large and can overwhelm the calculation. Secondly, when performing calculations in 3D, the number of grid points $N$ needed to represent the spin-orbitals can add $2-3$ orders of magnitude to the computation time. In 2D $N = N_x N_y$ and assuming $N_{x,y} \sim \mathcal{O}(100)$, which is typical for these calculations, then $N \sim \mathcal{O}(10^4)$. However, in 3D we now have $N = N_x N_y N_z \sim \mathcal{O}(10^6)$ for a single spin-orbital function. Thus, a calculation with $n$ spin orbitals may require the solution of $\approx 10^7 - 10^8$ coupled nonlinear ordinary differential equations for the spin-orbital part of the wavefunction. Unfortunately, the former challenge cannot be avoided in systems involving strong correlation or those containing more than a single electron in the continuum. This needs to be handled by efficient parallelization of the calculation and will not be discussed here. The latter challenge can be handled by reducing the number of grid points used to represent the spin-orbitals. This applies to problems involving only a single electron in the continuum where the number of spin-orbitals required is not too large. The focus of this chapter will be in dealing with second challenge.

On a uniform grid, the smallest grid spacing $\Delta x$ required by the system is used on every region of the grid. Consider an atomic calculation. If a fine resolution is required near the core then that same resolution will be used at the far edges of the simulation box where it may not be necessary to have such fine resolution. As such, more grid points will be used than are required. On the other hand, if a larger step is used for the same simulation range, the required resolution near the atomic core will not be achieved. This challenge can be overcome by representing the spin-orbitals on a nonuniform tensor product grid. This allows for the grid to be tailored to have a fine resolution in regions where such resolution is required and to have a coarse resolution where a fine resolution is not required. In order to perform MCTDHF calculations on a nonuniform grid, accurate methods for differentiation and integration will be required. In addition, since the FFT algorithm is not applicable to nonuniform grids, a new method of calculating the two-body terms is needed.

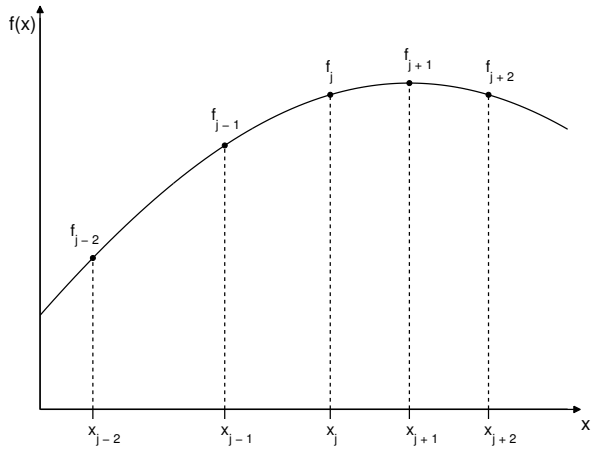


**Figure 8.1.** Schematic of differentiation on a nonuniform grid using $N_\mathrm{d} = 5$.

## 8.1 Differentiation on a nonuniform grid

As stated in Chap. 1, differentiation in the MCTDHF code is achieved through the use of the FFT and Eq. 1.39. When using a nonuniform grid the FFT can no longer be used to obtain an accurate derivative. As such, we resort to using finite difference methods. The standard finite difference formulas (and the less common higher order ones) are not suitable to this problem as they are derived for a uniform grid. Here a method is developed for computing formulas for the first and second derivatives based on a given grid. The points at the boundary of the grid will need to be handled by setting appropriate boundary conditions. A discussion of this is left until after the method is developed. Here the method is developed for a single grid line (one dimension); it is then straightforward to apply it to 2D or 3D calculations.

Let $x_j$ be the points along a single grid line and $f_j = f(x_j)$ where $\mathrm{j} = 1, \ldots, N$. In what follows we take $N_\mathrm{d}$ — the number of points used to approximate the derivative of f(x) at $x_\mathrm{j}$ — to be an odd integer and approximate $f^{(n)}(x_\mathrm{j})$ using $M$ points on either side of $x_\mathrm{j}$; see Fig. 8.1. We are searching for a formula for the $n^{th}$ derivative at $x_j$ of the form

$$f^{(n)}(x_\mathrm{j}) \approx \sum_{\mathrm{k}=1}^{N_d} a_{\mathrm{jk}}^{(n)} f(x_{\mathrm{j+k-M-1}}) \tag{8.1}$$

where $M = (N_\mathrm{d} - 1)/2$ and the $a_{\mathrm{jk}}^{(n)}$'s are the coefficients for the $n^{th}$ derivative formula at $x_\mathrm{j}$. Introducing the notation $h_{\mathrm{j+k}} = x_{\mathrm{j+k}} - x_\mathrm{j}$ and $f_{\mathrm{j+k}} = f(x_{\mathrm{j+k}})$ it is possible to write the system of equations

$$f(x_{\mathrm{j+k}}) \approx f(x_\mathrm{j}) + h_{\mathrm{j+k}} f'(x_\mathrm{j}) + \frac{h_{\mathrm{j+k}}^2}{2!} f''(x_\mathrm{j}) + \ldots + \frac{h_{\mathrm{j+k}}^{N_\mathrm{d}-1}}{(N_\mathrm{d}-1)!} f^{(N_\mathrm{d}-1)}(x_\mathrm{j}). \tag{8.2}$$

Thus, the set of equations centred at $x_\mathrm{j}$ is of the form $\mathbf{f}_\mathrm{j} = \mathbf{A}_\mathrm{j}\mathbf{F}_\mathrm{j}$ where

$$\mathbf{f}_\mathrm{j} = \begin{pmatrix} f(x_{\mathrm{j}-M}) \\ \vdots \\ f(x_\mathrm{j}) \\ \vdots \\ f(x_{\mathrm{j}+M}) \end{pmatrix} \tag{8.3}$$

and

$$\mathbf{F}_\mathrm{j} = \begin{pmatrix} f(x_\mathrm{j}) \\ f'(x_\mathrm{j}) \\ \vdots \\ f^{(N_\mathrm{d}-1)}(x_\mathrm{j}) \end{pmatrix} \tag{8.4}$$

and the non-singular matrix $\mathbf{A}_\mathrm{j}$ is given by

$$\mathbf{A}_\mathrm{j} = \begin{pmatrix} 1 & h_{\mathrm{j}-\mathrm{M}} & \frac{h_{\mathrm{j}-\mathrm{M}}^2}{2!} & \cdots & \frac{h_{\mathrm{j}-\mathrm{M}}^{N_\mathrm{d}-1}}{(N_\mathrm{d}-1)!} \\ 1 & h_{\mathrm{j}-\mathrm{M}+1} & \frac{h_{\mathrm{j}-\mathrm{M}+1}^2}{2!} & \cdots & \frac{h_{\mathrm{j}-\mathrm{M}+1}^{N_\mathrm{d}-1}}{(N_\mathrm{d}-1)!} \\ \vdots & \vdots & \vdots & \ddots & \vdots \\ 1 & h_{\mathrm{j}+\mathrm{M}} & \frac{h_{\mathrm{j}+\mathrm{M}}^2}{2!} & \cdots & \frac{h_{\mathrm{j}+\mathrm{M}}^{N_\mathrm{d}-1}}{(N_\mathrm{d}-1)!} \end{pmatrix}. \tag{8.5}$$

Inverting $\mathbf{A}_\mathrm{j}$ then gives the solution $\mathbf{F}_\mathrm{j} = \mathbf{A}_\mathrm{j}^{-1}\mathbf{f}_\mathrm{j}$. From this it is clear that the i$^{th}$ row of $\mathbf{A}_\mathrm{j}^{-1}$ gives the coefficients $a_{\mathrm{jk}}^{(i-1)}$. That is, the dot product of the first row with $\mathbf{f}_\mathrm{j}$ just reproduces $f(x_\mathrm{j})$, the dot product of the second row with $\mathbf{f}_\mathrm{j}$ gives $f'(x_\mathrm{j})$, the dot product of the third row with $\mathbf{f}_\mathrm{j}$ gives $f''(x_\mathrm{j})$ and so on. In fact, for $N_\mathrm{d}$ points, this method gives an approximate expression for the first $N_\mathrm{d} - 1$ derivatives; however, the quality of the approximation decreases with increasing order of the derivative.

As mentioned at the beginning of this section, the boundary points along each grid line will need to be treated by setting the appropriate boundary conditions. More specifically these points are the first and last $M$ points on the grid line. It is assumed that the behaviour of the function is known at the boundary in order for this method to be applied. For the MCTDHF calculations the value at these points is set to zero as we choose the simulation box large enough that the wavefunction never reaches the boundary.

To evaluate this method of numerical differentiation we calculate the first and second derivative of the normalized Gaussian

$$f(x) = \frac{1}{\sigma\sqrt{2\pi}} e^{-\frac{x^2}{2\sigma^2}} \tag{8.6}$$

with $\sigma = 0.4$, 2, 5. We use two different minimum grid spacings $\Delta x_\mathrm{min}$ with two different growth rates $\Gamma$ for a total of four test grids. For the minimum grid spacings $\Delta x_\mathrm{min} = 0.1$, 0.4 and for the growth rates $\Gamma = 1.05$, 1.1 (5% and 10% respectively). The grid is symmetric about $x = 0$. Derivatives are calculated using 3, 5, 7, 9, 11 and 13 points and the maximum error for the $n^{th}$ derivative is

$$\epsilon_\mathrm{max}^{(n)} = \max|f^{(n)}(x_\mathrm{j}) - \tilde{f}^{(n)}(x_\mathrm{j})| \tag{8.7}$$

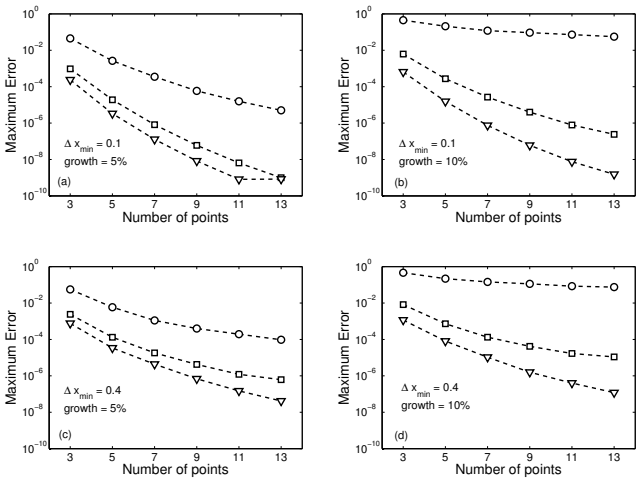


**Figure 8.2.** Maximum error for first derivative with $\sigma = 0.4$ ($\circ$), 2 ($\square$) and 5 ($\triangledown$).

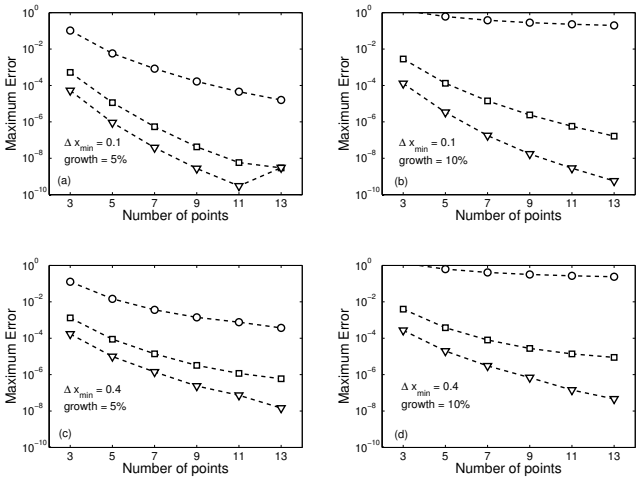


**Figure 8.3.** Maximum error for second derivative with $\sigma = 0.4$ ($\circ$), 2 ($\square$) and 5 ($\triangledown$).

where $\tilde{f}$ is the approximated $n^{th}$ derivative. Figs. 8.2 and 8.3 show the maximum errors for the first and second derivatives respectively.

Both Figs. 8.2 and 8.3 illustrate the effect that the choice of grid has on the calculation. If $\Delta x_{\min}$ is chosen too large — as is the case for the narrowest Gaussian ($\sigma = 0.4$) — sufficient accuracy will not be achieved. Accuracy will also be lost if the grid spacing is grown too fast. It is clear from Figs. 8.2 and 8.3 that the combination a poorly chosen $\Delta x_{\min}$ with a growth rate that is too fast will not yield viable results. However, an appropriately chosen grid allows for

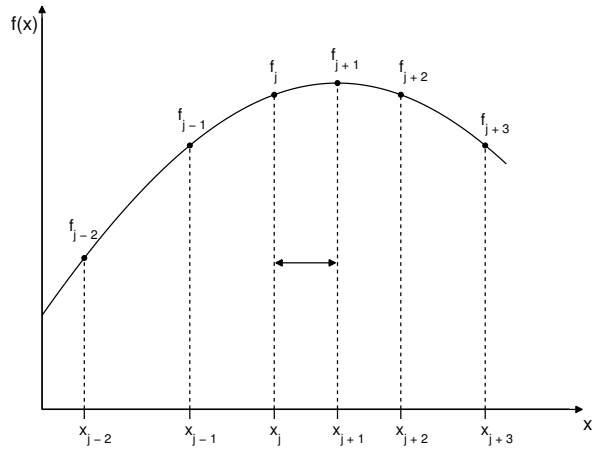


**Figure 8.4.** Schematic for integration on a nonuniform grid with $N_\mathrm{p} = 6$.

sufficient accuracy to be achieved.

## 8.2 Integration on nonuniform grids

On a uniform grid, integration is handled by the well known trapezoidal rule. For a grid spacing $h$ the error in this method is $\mathcal{O}(h^3)$. However, on a nonuniform grid the error is increased to $\mathcal{O}(h^2)$ and thus is not sufficient for accurate computation. As with the case of differentiation, consider the $N$ grid points $x_\mathrm{j}$, where $\mathrm{j} = 1, \ldots, \mathrm{N}$, along a single (1D) grid line and the values of a function $f(x_\mathrm{j})$ at these points. Let $N_\mathrm{p}$ be the even number of points used to calculate the integral for the interval $[x_\mathrm{j},\, x_{\mathrm{j}+1}]$. We wish to find an expression for the integral of the form

$$\int_{x_\mathrm{j}}^{x_{\mathrm{j}+1}} f(x)dx \;\approx \sum_{\mathrm{k}=1}^{N_\mathrm{p}} b_{\mathrm{jk}} f(x_{\mathrm{j}+\mathrm{k}-\mathrm{M}}) \tag{8.8}$$

where $M = N_\mathrm{p}/2$. Since $N_\mathrm{p}$ is even, there are $M-1$ points on each side of the interval $[x_\mathrm{j},\, x_{\mathrm{j}+1}]$; see Fig. 8.4. To determine the $b_{\mathrm{jk}}$'s we will apply the method of undetermined coefficients using a polynomial basis. Thus, it is important that the integration interval be $[x_\mathrm{j},\, x_{\mathrm{j}+1}]$ and not $[x_{\mathrm{j}-\mathrm{M}+1},\, x_{\mathrm{j}+\mathrm{M}}]$ for the following reason. The method of undetermined coefficients will yield a polynomial interpolation over the interval $[x_{\mathrm{j}-\mathrm{M}+1},\, x_{\mathrm{j}+\mathrm{M}}]$; however, the interpolating polynomial will not be accurate near the boundaries of the interval. For larger $N$ the interpolation in this range will get worse — the Runge effect. However, the polynomial will be accurate at the centre of the interval $[x_{\mathrm{j}-\mathrm{M}+1},\, x_{\mathrm{j}+\mathrm{M}}]$ and will allow for an accurate approximation of the integral over the range $[x_\mathrm{j},\, x_{\mathrm{j}+1}]$.

We begin by defining $h_{\mathrm{j}+\mathrm{k}} = x_{\mathrm{j}+\mathrm{k}} - x_\mathrm{j}$ and note the formula in Eq. 8.8 will be exact for

polynomials up to order $N-1$; that is,

$$\int_{x_\mathrm{j}}^{x_{\mathrm{j}+1}} (x-x_\mathrm{j})^n dx = \frac{1}{n+1}(x_{\mathrm{j}+1}-x_\mathrm{j}) = \frac{1}{n+1}h_{j+1}^{n+1} \tag{8.9}$$

for $n = 0, \ldots, N-1$. Using Eq. 8.8, this allows us to write the set of equations

$$b_{\mathrm{j}(-\mathrm{M}+1)}h_{\mathrm{j}-\mathrm{M}+1}^n + b_{\mathrm{j}(-\mathrm{M}+2)}h_{\mathrm{j}-\mathrm{M}+2}^n + \ldots + b_{\mathrm{j}(\mathrm{M}-1)}h_{\mathrm{j}+\mathrm{M}-1}^n + b_{\mathrm{j}\mathrm{M}}h_{\mathrm{j}+\mathrm{M}}^n = \frac{1}{n+1}h_{j+1}^{n+1} \tag{8.10}$$

where the polynomial basis is centred about $x_\mathrm{j}$ for numerical considerations. This system is in the form $\mathbf{A}_\mathrm{j}\mathbf{b}_\mathrm{j} = \mathbf{h}_\mathrm{j}$ where

$$\mathbf{b}_\mathrm{j} = \begin{pmatrix} b_{\mathrm{j}(-\mathrm{M}+1)} \\ b_{\mathrm{j}(-\mathrm{M}+2)} \\ \vdots \\ b_{\mathrm{j}\mathrm{M}} \end{pmatrix} \tag{8.11}$$

and

$$\mathbf{h}_\mathrm{j} = \begin{pmatrix} h_{\mathrm{j}+1} \\ \frac{1}{2}h_{\mathrm{j}+1}^2 \\ \vdots \\ \frac{1}{N}h_{\mathrm{j}+1}^N \end{pmatrix} \tag{8.12}$$

and $\mathbf{A}_\mathrm{j}$ is the non-singular matrix given by,

$$\mathbf{A}_\mathrm{j} = \begin{pmatrix} 1 & 1 & \cdots & 1 \\ h_{\mathrm{j}-\mathrm{M}+1} & h_{\mathrm{j}-\mathrm{M}+2} & \cdots & h_{j+M} \\ h_{\mathrm{j}-\mathrm{M}+1}^2 & h_{\mathrm{j}-\mathrm{M}+2}^2 & \cdots & h_{j+M}^2 \\ \vdots & \vdots & \ddots & \vdots \\ h_{\mathrm{j}-\mathrm{M}+1}^{N-1} & h_{\mathrm{j}-\mathrm{M}+2}^{N-1} & \cdots & h_{j+M}^{N-1} \end{pmatrix}. \tag{8.13}$$

The coefficients required in Eq. 8.8 can then be determined by $\mathbf{b}_\mathrm{j} = \mathbf{A}_\mathrm{j}^{-1}\mathbf{h}_\mathrm{j}$. When all grid points are uniformly spaced, the above method will yield the well known Newton-Coates formulas for integration [47].

To test the integration formulas we use the normalized Gaussian in Eq. (8.6) and use the same widths as were used when testing the formulas for differentiation. In addition, the same $\Delta x_{\min}$'s and growth rates for the grid are used. The results of these tests are shown in Fig. 8.5 where the error – absolute value of the calculated result minus the exact result — is plotted for $N_\mathrm{p} = 2$, 4, 6, 8, 10, 12, and 14. As with differentiation, if $\Delta x_{\min}$ is chosen to be too large, the calculation will not yield sufficient accuracy regardless of how the grid is grown; see Figs 8.5(a) and 8.5(c). This results from the fact that when $\Delta x_{\min}$ is chosen to be too large, the grid cannot adequately resolve the function that we wish to integrate. Furthermore, when the grid is grown too fast, even for an appropriately chosen $\Delta x_{\min}$, the end result will be a loss of a few orders of magnitude in accuracy; see Figs 8.5(a) and 8.5(c). When both $\Delta x_{\min}$ and the growth rate are chosen poorly, the results of the calculation are seriously degraded and may not be useful at all; see Fig. 8.5(d).

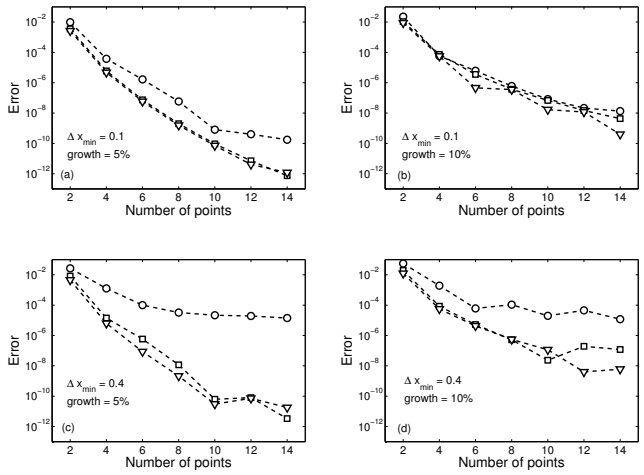


**Figure 8.5.** Error in integration with $\sigma = 0.4$ ($\circ$), 2 ($\square$) and 5 ($\triangledown$).

## 8.3 Treatment of the two-body terms

It was noted at the beginning of this chapter that the FFT is not suitable for nonuniform grids and hence the convolution theorem cannot be applied when solving integrals of the form

$$\phi(\mathbf{r}) = \int \frac{\rho(\mathbf{r}')}{|\mathbf{r} - \mathbf{r}'|} d\mathbf{r}'. \tag{8.14}$$

It is not feasible to directly integrate Eq. (8.14) because, for $N$ grid points, $N$ one-body integrations would need to be performed. For a $3D$ calculation this would completely consume the computation time. Fortunately, integrals of this form can still be evaluated in an efficient manner without the need to directly perform the integration. The Poisson equation,

$$\nabla^2 \Phi(\mathbf{r}) = -\rho(\mathbf{r}) \tag{8.15}$$

has the solution

$$\Phi(\mathbf{r}) = \frac{1}{4\pi} \int \frac{\rho(\mathbf{r}')}{|\mathbf{r} - \mathbf{r}'|} d\mathbf{r}' \tag{8.16}$$

which, apart from a constant, is the same form as in Eq. (8.14). To solve Poisson's equation we use the MOEVE package. MOEVE is a multigrid algorithm adapted for nonuniform tensor product grids. The speed of MOEVE is comparable to that of FFTW.

## 8.4 Selecting the grid

As previously alluded to in sections 8.1 and 8.2, an appropriate choice of grid is integral to achieving accurate results. To obtain optimal results the grid must be tailored to the system being investigated. For example, diatomic hydrogen would require a grid that has two dense regions near each of the atomic nuclei and is sparse further away from the atoms. An important

component of the grid is the choice of the minimum grid spacing $\Delta x_{\min}$. It is critical that this be chosen in such a manner that it is small enough to resolve the wavefunction but not so small as to force an extremely small time step on the propagator.

Once the dense regions of the grid are identified and a $\Delta x_{\min}$ is chosen the rest of the grid must be determined. In sections 8.1 and 8.2 calculations were performed with a grid that was grown at a constant rate in each direction about the point $x = 0$. While this is the simplest way to generate a grid it is not always optimal. Another way to generate a grid is to use an accelerated growth rate. That is, the grid in dense regions will grow slowly and the growth rate will increase for points further away from the dense regions.

One final thing to consider is the maximum grid spacing $\Delta x_{\max}$. If the allowable grid spacing is not capped, it is possible to have very large grid spacings in the calculation; these have the potential to produce large errors. However, more importantly, is the effect that a large grid spacing will have on problems involving ionization. For these problems $\Delta x_{\max}$ must be limited in such a way that the maximum momentum of the free electron can still be resolved. At the very least we should have

$$\frac{\pi}{\Delta x_{\min}} > \mathrm{k}_{\max} \tag{8.17}$$

where $\mathrm{k}_{\max}$ is the maximum momentum the ionized electron will reach.

## 8.5 Ground state of small sodium clusters

As a test of MCTDHF using nonuniform grids we will calculate the groundstates of two small sodium clusters in 3D by performing imaginary time propagation. A single sodium atom has 11 electrons which already pushes the limits of MCTDHF. When the system contains more than a single Na atom it is not feasible to model every electron. In order to overcome this hurdle we use a pseudopotential to account for the core electrons and only model those in the valence shell. Sodium has the electron configuration $1s^2 2s^2 2p^6 3s^1$, or [Ne]$3s^1$, and thus only the single electron in the $3s$ shell will be active. The remaining 10 electrons will be accounted for by the pseudopotential. The pseudopotential used for these calculations is the Topp-Hopfield potential [155] given by

$$U(r) = \begin{cases} 0.1790\cos(1.224r) - 0.179 & \text{for } r \leq 3 \\ -1/r & \text{for } r > 3 \end{cases} \tag{8.18}$$

where $r$ is the radial coordinate given by $r = \sqrt{x^2 + y^2 + z^2}$.

We will calculate the ground state of the sodium clusters $Na_4$-$D_{4h}$ and $Na_6$-$C_{5v}$ using the structures given in Ref. [156]. The geometry of $Na_4$-$D_{4h}$ is planar; the sodium atoms form the corners of square with sides of length 3.355Å. The geometry of the $Na_6$-$C_{5v}$ cluster is a pentagonal pyramid. The sides of the pentagon are of length 3.610Å and the height of the pyramid is 2.913Å. For our calculations the $Na_4$-$D_{4h}$ cluster lies in the $x$-$y$ plane with the centre of the square at the origin. For the $Na_6$-$C_{5v}$ cluster the pentagonal base of the pyramid lies in the $x$-$y$ plane and the peak of the pyramid is centred at the origin and extends up into the $z$-axis. In our calculations the $Na_4$-$D_{4h}$ and $Na_6$-$C_{5v}$ clusters contain four and six active electrons respectively.

For our calculations we use a nonuniform grid with $N_x = N_y = N_z = 120$ with a minimum grid spacing of $\Delta x_{\min} = 0.38$ around the origin. The $x$-axis is grown at a rate of 2% for $|x| \leq 10$; for $|x| > 10$ the grid is grown at a rate of 5% to a maximum step size $\Delta x_{\max} = 2$. The total range on the $x$-axis is then $\pm 106$. The $y$ and $z$ axes are chosen in the same manner. For comparison

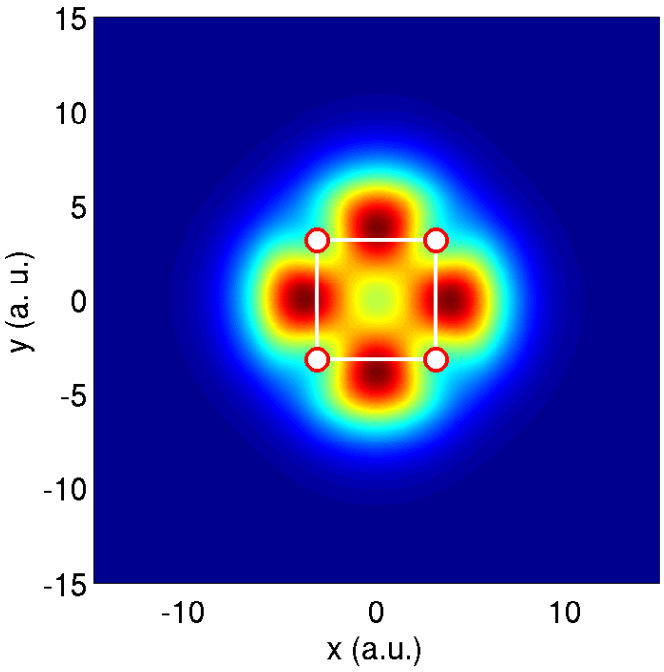


**Figure 8.6.** Ground state density of the $Na_4$-$D_{4h}$ cluster. The dots show the position of the Na atoms.

the calculations are also repeated using a uniform grid with a grid spacing equal to the minimum grid spacing used for the nonuniform grid. However, to make the calculations feasible, we do not use the same range for this grid. For the uniform grid we use $N_x = N_y = N_z = 230$ points giving a range of roughly $\pm 45$. Although, we don't perform ionization calculations here, it is important to note that in order to achieve the same range as the nonuniform grid, $N_x = N_y = N_z = 557$ would need to be used for the uniform grid. This makes the number of points on the uniform grid $N_u = 557^3$ as opposed to $N_{\rm nu} = 120^3$ for the nonuniform grid. This translates into $N_{\rm u} \approx 100 N_{\rm nu}$; that is, the number of points needed for the uniform grid is two orders of magnitude larger than required by the nonuniform grid.

For the $Na_4$-$D_{4h}$ cluster we perform the MCTDHF imaginary time calculation of the ground state using 12 spin-orbitals. The calculated ground state energy for this system is found to be $E_0(Na_4) = -1.692$. For the $Na_6$-$C_{5v}$ cluster the MCTDHF calculation is performed using 16 spin-orbitals and a ground state energy of $E_0(Na_6) = -3.316$ is calculated. The calculations on the uniform grid are performed using the same number of spin-orbitals as their nonuiform grid counterparts. The ground state energies found by these calculations are in agreement with those found by the nonunform grid calculations. Fig. 8.6 shows that the ground state density

$$\rho(x, y) = \int |\Psi_0(x, y, z)|^2 \, dz \tag{8.19}$$

for the $Na_4$-$D_{4h}$ cluster where $\Psi_0$ is the ground state wavefunction and integration is performed over the $z$-coordinate. Also shown is the cluster configuration. Fig. 8.7 shows the ground state density, with integration over the $z$-coordinate, of the $Na_6$-$C_{5v}$ cluster. A bird's eye view of the pentagonal pyramid structure is also shown.

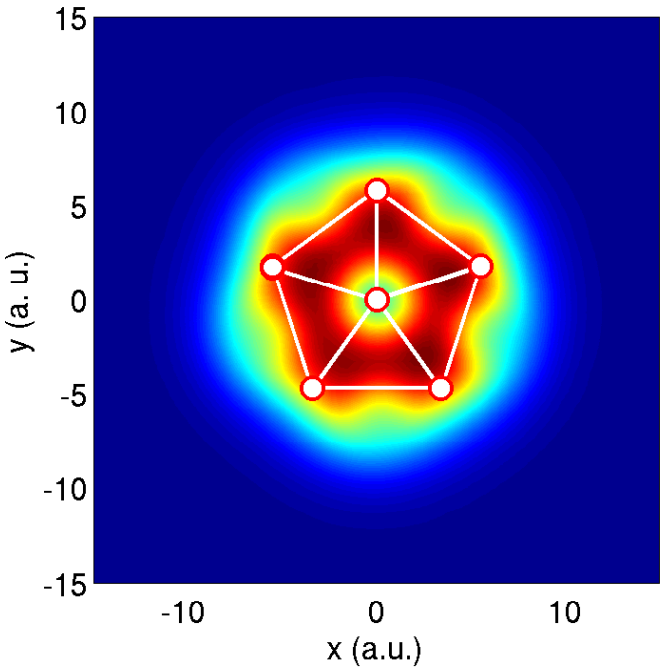


**Figure 8.7.** Ground state density of the $Na_6$-$C_{5v}$ cluster. The dots show a birds eye view of the position of the Na atoms.

## 8.6 Outlook

The calculations in the previous section were meant to demonstrate the benefits and viability of performing MCTDHF calculations on nonuniform Cartesian tensor product grids. Small sodium clusters were chosen for the calculations due to the availability of a simple local pseudopotential for the sodium atoms. The ultimate goal, however, is to perform calculations on atoms and molecules using up to 10 electrons. Most of the systems that we wish to investigate will contain more that 10 electrons so, as with the above calculations, we will need to use pseudopotentials to account for the non-active electrons in the system. Furthermore, these pseudopotentials will, in general, not be simple local potentials, similar to the one used in Sec. 8.5, but will contain non-local terms. These potentials are of the form

$$W(\mathbf{r}) = \sum_{l=0}^{l_{\max}} W_l(\mathbf{r}) \sum_{m=-l}^{l} |lm\rangle \langle lm| \tag{8.20}$$

where $l$ and $m$ are the angular momentum and magnetic quantum numbers respectively [157–159].

The combination of the nonuniform grid with appropriate pseudopotentials will allow us to investigate systems in strong laser fields that were previously inaccessible. First, it will be possible to investigate the tunnel ionization rates of noble gases — particularly Ne, Ar, Kr and Xe — as a function of laser intensity. These calculations can be done by ramping on the field over a quarter cycle and then leaving it constant at the peak value; the outgoing probability will be absorbed using a complex absorbing potential. The ionization rate can be determined when the outgoing flux reaches a constant rate.

The calculation of ionization rates is fairly straightforward and provides a simple way to apply our MCTDHF code; these calculations are currently in progress. However, a more important future objective of MCTDHF on nonuniform tensor product grids will be investigate complex ionization processes similar to those observed in Ref. [15]. In these experiments Ne and Xe atoms are excited by a subfemtosecond extreme ultraviolet (XUV) pulse. A few-cycle near-infrared (NIR) pulse is then used to probe or start the electron dynamics. The time delay between the two pulses is varied and the ion counts from the shake-up states then display sharp rises that cannot be predicted by current theories; as such new theories are required [15]. With our implementation of MCTDHF we will be able to investigate these complex ionization processes. In addition we will be able to investigate the nonlinear processes observed in XFEL experiments on neon atoms [20].

Another problem to be considered is the orbital rearrangement that occurs in a molecule as a result of ionization. As mentioned in at the beginning of Chap. 1, experiments conducted on $CH_4$ (methane) have shown an orbital rearrangement that occurs within a few femtoseconds of ionization [14]. By using four active electrons in the carbon atom, the system will contain a total of eight electrons. For these calculations we will ionize a single electrons and observe how the molecule rearranges its orbitals to compensate for the loss of the electron — a problem for which MCTDHF is ideally suited. In addition we will also be capable of performing high-harmonic generation calculations on the previously mentioned noble gas atoms and $CH_4$. Since it is possible to absorb the long trajectories, we will not need a large grid, hence making these calculations feasible in the near future.

Finally, 3D problems with a cylindrical symmetry can be treated efficiently by extending the above formalism to cylindrical coordinates.This is done by expanding the spin-orbitals as

$$\varphi_{\mathrm{j}}(r,\, z,\, \theta) = \frac{1}{\sqrt{2\pi}} \sum_{m=-m_{\max}}^{m_{\max}} f_{\mathrm{j}}^{m}(r,\, z)\mathrm{e}^{-im\theta}\,. \tag{8.21}$$

With the above expansion, the MCTDHF equations of motion for the spin-orbitals are reduced to two dimensions. Thus, if only a small number of $m$-values are needed, the 3D calculation has effectively been reduced to a 2D calculation. This will allow for problems requiring a larger simulation box to be treated. Currently, a cylindrical MCTDHF code is being developed with the aim of examining electron impact ionization cross-sections in strong fields. This is a problem that has been present since the birth of plasma physics almost 100 years ago.

Our MCTDHF code will be a powerful tool to investigate non-perturbative multielectron dynamics in atoms and molecules. The applications presented here are merely a small subset of the possible applications.

# Chapter 9

# Tunnel ionization dynamics of bound systems in laser fields: How long does it take for a bound electron to tunnel?

*C. R. McDonald, G. Orlando, G. Vampa and T. Brabec, Phys. Rev. Lett.* ***111****, 090405 (2013).*

The inception of quantum mechanics in the first part of the 1900's led to the discovery of many phenomena that possess no classical analogue. One of the most ubiquitous of these is tunneling [160] — the ability of waves (light or particles) to penetrate a potential barrier that would otherwise be insurmountable classically. Today, electron tunneling is used in many areas of science and technology, such as scanning tunneling microscopy [161], tunnel diodes [162], and more recently in attosecond science [14, 19, 163, 164].

For many decades the time involved in tunneling has been studied experimentally and theoretically by examining the scattering process of an incoming wave impinging on a potential barrier. This research has yielded a wealth of different interpretations; see Ref. [165] and references therein. Here, we focus on the tunnel time of bound particles escaping their binding potential in the presence of a perturbation. Such a half scattering event is conceptually different from scattering through a barrier. Comparatively little is known about the tunnel time of perturbed bound systems, mostly due to a lack of experimental methods.

Only recently, progress in attosecond technology has allowed for a deeper look into the process of tunnel ionization of atoms [15–17, 21, 166, 167]. Attosecond angular streaking experiments have indicated that the tunnelling delay time is non-existent [16]. Recent experiments seem to indicate a finite tunneling time [21]. These experimental investigations have raised the question of what tunnel time in the context of tunnel ionization of bound systems means.

In a seminal paper, Keldysh developed a dynamic theory of optical field ionization of atoms for time varying laser fields [168]. Ionization occurs predominantly as multi-photon or as tunnel ionization [169, 170] in the limits of $\gamma \gg 1$ and $\gamma \ll 1$, respectively. The Keldysh parameter $\gamma = 4\pi\tau_\mathrm{k}/T_0$ is defined as the ratio of the Keldysh tunnel time $\tau_\mathrm{k} = l/|v|$ and laser oscillation period $T_0 = 2\pi/\omega$ with $\omega$ the laser circular frequency. The tunnel time can be interpreted as the time it takes the bound electron having velocity $v = i\sqrt{2E_0}$ to cross the tunneling barrier with width $l = E_0/F$, where $F$ is the laser electric field and $E_0$ is the electron binding energy. As the electron is classically not allowed under the barrier, its velocity is imaginary. This makes a particle interpretation of a tunnel time unattractive.

Still, the Keldysh parameter displays the right characteristics one would expect from a tunnel time. It suggests that tunneling is discouraged, when the laser field changes too fast for the electron to find its way out through the barrier. However, neither the Keldysh theory nor any other work give a hint to a clean definition of the tunnel time by which the following fundamental

questions can be answered. How is the tunnel time connected to the wavefunction dynamics? What are the reference points between which the tunnel time is defined? How can the tunnel time be measured?

The aim here is to close this gap. We use 1D quantum dot (QD) and atomic model systems for our investigation. These systems are perturbed by a laser electric field with a step function switch-on from 0 to $F$. When the field is switched on, the ground state becomes a dynamic resonance state decaying with time-dependent ionization rate $\mathrm{w}(t)$, until it reaches a constant ionization rate $\mathrm{w}(F)$. This happens when the wavefunction in and close to the bound region approaches the static resonance determined by a solution of the time-independent Schrödinger equation (TISE) for constant field $F$ [169,170]. To associate a tunnel time with the step response dynamics of the wave function, a method is needed to extract the tunneling rate. For this two main obstacles must be overcome.

First, tunnel ionization is usually measured by calculating the outgoing current at some reference point. This method is unsuitable for measuring the tunnel time, as the temporal evolution of the ionization rate depends on the choice of reference point. We use a time-dependent generalization of Fano-resonance theory in which the imaginary part of the resonance determines the ionization rate. This method is reference point free. Both approaches give the same final static ionization rate $\mathrm{w}(F)$.

Secondly, the step response not only contains the tunneling signal from the ground state, but also a contribution due to the "sudden switch-on" resulting in population and ionization of excited states. This obstacle is overcome by pairing the generalized Fano approach with a spectral filtering method. From the resulting dynamic tunnel ionization rate the tunnel time can be evaluated.

Our analysis reveals the following definition for the tunnel time of bound particles. Assume a bound system in the presence of a general perturbation $P$, which turns the ground state into a resonance state decaying with constant ionization rate $\mathrm{w}(P)$, as determined by the TISE. Now assume that the perturbation is switched on by a step-function. The tunnel time is the response time it takes the part of the wavefunction tunneling directly from the ground state to establish $\mathrm{w}(P)$.

At the end, the step function definition of the tunnel time is generalized to time varying fields. We find that the tunnel time scales with $\tau_\mathrm{k}$ for step function and sinusoidal fields. Thus, the physical meaning of the tunnel time and its connection to $\tau_\mathrm{k}$ is established. Finally, in light of our definition, we propose a way to measure the tunnel time experimentally.

Consider the response of a system, initially in its ground state, subject to an instantaneous switch-on of a static electric field at time $t = 0$. In dipole approximation and length gauge, the Hamiltonian is given by,

$$H = \begin{cases} H_0 & \text{for } t < 0 \\ H_0 - Fx & \text{for } t \geq 0 \end{cases} \tag{9.1}$$

where $H_0 = T + V$ with $T$ the kinetic energy, $V$ the potential and $F$ the static electric field. Atomic units are used throughout. We express the wavefunction as

$$|\Psi(t)\rangle = \mathrm{a}(t)\,|0\rangle + |\phi(t)\rangle \tag{9.2}$$

where $|0\rangle$ is the unperturbed ground state and $\mathrm{a(t)} = \langle 0|\,\Psi(\mathrm{t})\rangle$. The last term in Eq. (9.2) is the part of the wavefunction that develops in response to the external field for which $\langle 0|\,\phi(t)\rangle = 0$ is enforced; it is zero in the absence of the external field. Inserting Eq. (9.2) into the time-dependent Schrödinger equation (TDSE) with the Hamiltonian given in Eq. (9.1) and projecting $\langle 0|$, yields

an equation of motion for $a(t)$,

$$i\dot{\mathrm{a}}(t) = E_0 \mathrm{a(t)} + \langle 0| H_0 - Fx |\phi(t)\rangle \,, \tag{9.3}$$

where $E_0 = \langle 0| H |0\rangle$. Choosing the *ansatz* $|\phi(t)\rangle = a(t)\,|\varphi(t)\rangle$ we arrive at the expression

$$\Delta E(t) = i\frac{\dot{\mathrm{a}}(t)}{\mathrm{a}(t)} - E_0 \tag{9.4}$$

where $\Delta E(t) \equiv \langle 0| H |\varphi(t)\rangle$; $\mathrm{w}(t) = -2\mathrm{Im}\{\Delta E(t)\}$ gives the rate at which probability leaves the ground state and escapes into the continuum. To completely determine $|\Psi\rangle$, a corresponding equation for the time evolution of $\phi(t)$ can be obtained by projecting $1 - |0\rangle\langle 0|$ on the TDSE. The resulting equation is not given, as it is not used here. Eq. (9.4) is the time-dependent generalization of Fano resonance theory [171]. By using the TISE instead of the TDSE in our derivation, the regular Fano resonance theory would be obtained yielding the static tunneling rate for $\Delta E$. Typically, tunneling is calculated by looking at the flux that flows past a certain point. As a result, the time to reach a steady state is dependent on the observation point; using $\Delta E(t)$ from the generalized Fano approach removes this ambiguity.

The above equations were developed for diagnostic purposes. To actually calculate $|\Psi(t)\rangle$, $\Delta E$ and the tunneling time, it is advantageous to use a spectral method. This method allows us to separate the tunneling contribution from the rest of the wavefunction, a prerequisite for determining the tunnel time. Time propagation is handled by expanding the total wavefunction on the eigenstates of the field-dressed Hamiltonian as,

$$|\Psi(t)\rangle = \sum_{\mathrm{j}} g_{\mathrm{j}} e^{-i\epsilon_j t} |\xi_{\mathrm{j}}\rangle \tag{9.5}$$

where $g_{\mathrm{j}} = g(\epsilon_{\mathrm{j}}) = \langle \xi_{\mathrm{j}}| 0\rangle$ and $|\xi_{\mathrm{j}}\rangle$, $\epsilon_{\mathrm{j}}$ are the continuum eigenvectors and eigenvalues for the field-dressed Hamiltonian in Eq. (9.1) respectively. Here we have chosen a discrete notation for the energy $\epsilon$ and the spectral probability amplitude $g(\epsilon)$ of the continuum states consistent with the finite box size used in the numerical simulations. From the expansion in Eq. (9.5) it is straightforward to obtain expressions for $\mathrm{a}(t)$ and $\dot{\mathrm{a}}(t)$. By using $\mathrm{a(t)} = \langle 0|\,\Psi(\mathrm{t})\rangle$ together with Eq. (9.4), $\Delta E(t)$ becomes

$$\Delta E(t) = \frac{\sum_{\mathrm{j}} \epsilon_{\mathrm{j}} \mid g_{\mathrm{j}} \mid^2 e^{-i\epsilon_{\mathrm{j}} t}}{\sum_{\mathrm{j}} \mid g_{\mathrm{j}} \mid^2 e^{-i\epsilon_{\mathrm{j}} t}} - E_0. \tag{9.6}$$

We begin by solving the TDSE for the QD potential

$$V(x) = \begin{cases} \frac{1}{2}\alpha^2 x^2 - \beta & \text{for } |x| < \sqrt{2\beta}/\alpha \\ 0 & \text{otherwise} \end{cases} \tag{9.7}$$

with $\alpha = 1/2$ and $\beta = 3/4$. This system contains only the ground state and a first excited state at the continuum threshold. Initially the system is in the state $|0\rangle$; at $t = 0$ the static field is switched on.

Fig. 9.1 shows the spectral density $\mid g_{\mathrm{j}} \mid^2$ as a function of energy for the system at $F = 0.08$; all other field strengths investigated display a similar behavior. Note that the laser field turns discrete bound states into mixed bound-continuum resonance states with a finite spectral width. The spectrum has a minimum at around an energy of $-0.35$, which separates two distinct features of the step response: (i) The sharp peak to the left represents tunnel ionization from the ground

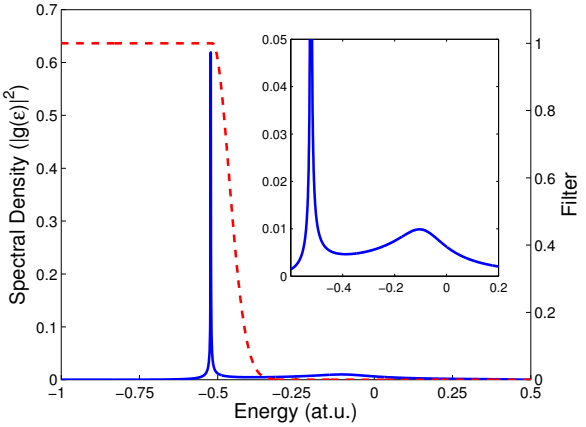


**Figure 9.1.** Spectral density (solid blue line) and filter (dashed red line) as a function of energy $\epsilon$; the inset shows a magnified section of the spectral density; 1D quantum dot potential for $F = 0.08$.

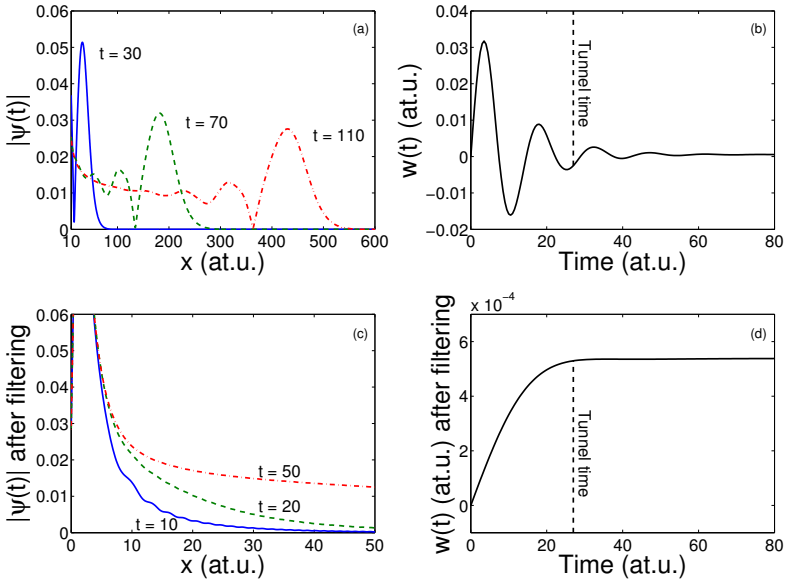


**Figure 9.2.** (a) Magnitude of $\Psi(x)$ for $t = 30$ (solid blue), $t = 70$ (dash green) and $t = 110$ (dash-dot red); to illustrate the outgoing wave, the bound region is not shown. (b) Ionization rate w($t$) corresponding to (a). (c) Magnitude of the filtered wavefunction (ground state resonance only) for $t = 10$ (solid blue), $t = 20$ (dash green) and $t = 50$ (dash-dot red); filter is given in Fig. 9.1. (d) w($t$) corresponding to (c). 1D quantum dot potential and $F = 0.08$ for (a)-(d).

state directly. (ii) The broad peak to the right corresponds to photon absorption and ionization via the excited state resonance. In a time varying laser pulse, features (i) and (ii) correspond to tunnel and multi-photon ionization respectively. As long as the minimum is outside the spectral widths of both features, tunneling and excited state channels can be separated by multiplying a spectral filter on the probability amplitudes $g(\varepsilon_\mathrm{j})$; see the (red) dashed line in Fig. 9.1. The choice of the filter function is discussed in appendix B.

The tunnel ionization peak in Fig. 9.1 reveals the spectral signature of the tunnel ionization dynamics. An exponential decay in time corresponds to a Lorentzian spectrum, the width of which determines the tunnel ionization rate. Our spectrum is Lorentzian with a small asymmetric distortion and a phase, which are responsible for the switch-on of the tunneling process. As the functional form of the spectral distortion is not known, extraction of the tunneling time is easier in the time domain.

Figures 9.2(a) and (c) show the total (unfiltered) and filtered wavefunction, respectively, as determined by Eq. (9.5), at three evolution times; different times are chosen for (a) and (c). Figures 9.2(b) and (d) show the corresponding unfiltered and filtered ionization rates, respectively; the ionization rate is calculated using Eq. (9.6) and the expression for $\mathrm{w}(t)$ above. In the filtered calculation, filter weighted coefficients $g_\mathrm{j}$ are used to isolate the part of the wavefunction tunneling via the ground state resonance.

In response to the step function switch-on of the laser field, the excited state ionization channel creates an outward propagating initial wave in Fig. 9.2(a). This causes strong oscillations of the ionization rate in 9.2(b), masking the tunneling signal. Once the initial wave has passed beyond the bound state region, the wavefunction reaches a steady state, see the (green) dashed and (red) dash-dotted lines close to the origin in 9.2(a). A steady flow of probability from the ground state into the continuum is established, representing the static resonance with constant tunneling rate, see Fig. 9.2(b).

After filtering, the initial outgoing wave signal is no longer present in Fig. 9.2(c). We see a wavefunction monotonically rising towards a steady-state. As a result, the tunneling rate rises monotonically and approaches a steady state value. We define this rise time as the electron tunneling time $\tau_\mathrm{t}$. For times much shorter than the tunneling time, the wavefunction components under the barrier that are necessary for tunneling cannot be developed and tunnel ionization does not occur. For all investigated field strengths, the tunnel time is considerably shorter than the time it takes for the excited state ionization signal to subside. Therefore, filtering is indispensable for extracting the tunnel time.

To calculate the tunnelling time $\tau_\mathrm{t}$ we use $\mathrm{w}(t)$ after filtering and determine the time at which it is within 1% of its steady state value; the results of this can be seen in Fig. 9.3. Results are shown for the QD and for a 1D softened Coulomb potential $V(x) = (x^2 + b^2)^{-1/2}$. The shielding parameter $b$ is chosen such that the ionization potential is $\approx 0.5$ (the same as the QD potential). The spectral features for the Coulomb potential are similar to the QD; however, the two peaks merge earlier, around $F = 0.07$. The results of our tunnel time calculations scale with the Keldysh time as $\tau_\mathrm{t} \approx 4.4\tau_\mathrm{k}$ for the QD and as $\tau_\mathrm{t} \approx 5.8\tau_\mathrm{k}$ for the 1D model atom.

We have defined the tunnel time for a step-function response. To define the duration of any physical process, an initial and final reference point is necessary. The step function has allowed us to define the ground state and static resonance as reference states between which the tunnel time can be defined and measured. The resulting tunnel time $\tau_\mathrm{t} \propto \tau_\mathrm{k}$ and has a physically intuitive interpretation; tunneling cannot manifest for $t \ll \tau_\mathrm{t}$ and maximum tunneling with the static ionization rate is reached for $t \gtrsim \tau_\mathrm{t}$.

In the remainder, the definition of the tunnel time will be generalized to time varying laser fields. To understand what happens in a sinusoidal laser field, let us decompose it into small

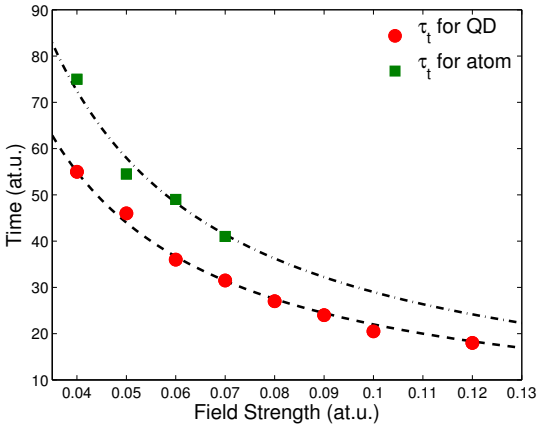


**Figure 9.3.** Calculated $\tau_t$ for the QD and atomic potentials. The lines in the plot represent the Keldysh time multiplied by a constant to match $\tau_t$.

step functions. The field changes from $F$ to $F + \Delta F$ and remains constant over a time $\Delta t$; the step size $\Delta F \propto \omega \Delta t$. In the tunneling regime, $\gamma \lesssim 1$, the initial state at $F$ is no longer the unperturbed ground state, but a state that has already developed tunneling components. The dynamics that takes place during $\Delta t$ is the wavefunction attempting to develop components to realize the static resonance state for $F + \Delta F$. The time needed for realizing the static resonance for one step can be viewed as a local tunnel response time that will vary throughout the laser cycle. However, a meaningful tunnel time cannot be defined, as both initial and final states are tunnel ionizing.

For a sinusoidal field with peak value $F_0$ and period $T_0$, a natural way to generalize the tunnel time is to use a quarter cycle; this resembles a softened switch-on function. In contrast to the step function the time of measurement is not free but determined by $T_0/4$; it can only be varied by changing $\omega$. Initial and final reference states are taken at the field minimum and its subsequent maximum. This applies to linearly as well as elliptically polarized fields. It is assumed that the initial state at the field minimum is close to the ground state where tunnel ionization is negligible compared to the field maximum. As a result, the tunnel time is determined by the quarter oscillation period for which the ground state transforms into the static resonance for $F_0$.

In agreement with the step function definition, tunneling cannot manifest for $T_0/4 \ll \tau_t$. For $T_0/4 \geq \tau_t$ the static ionization rate, and therewith maximum tunneling, is reached at and around the pulse peak. As tunnel ionization predominantly occurs close to the oscillation peak, maximum ionization is essentially reached for the whole half cycle. Therewith, the tunnel time $\tau_t$ represents the time it takes for tunneling to fully develop for each half cycle in a sinusoidal field. At the same time, when the static resonance and maximum tunneling are realized, the quasi-static regime is reached, where the static ionization rate follows adiabatically the laser field in the area around the oscillation peak. The onset of the quasi-static ionization regime is known to be determined by $\gamma = 2\omega\tau_k$ [168]. Therewith, $\tau_t \propto \tau_k$ for both the step function and the sinusoidal field, but the values of $\tau_t$ will differ.

Implicit in the above discussion is a method to measure the tunnel time. There exists a field with frequency $\omega$ such that its quarter cycle time $T_0/4$ will mark the onset of the quasi-static ionization rate $w(F_0)$. The measured tunneling signal will reach the quasi-static limit and

saturate for decreasing $\omega$. The quarter cycle time at which the difference between measured and quasi-static tunnel ionization lies below some prescribed accuracy will yield $\tau_t$. Extraction of the tunnel time requires removal of the multi-photon ionization components. Experimentally, this can be done by methods such as those used in references [16] and [21]. Theoretically, this can be achieved by applying the methods developed here for the step function to a sinusoidal field.

# PART 3

# CONCLUSION

# Chapter 10

# Conclusion and Outlook

A treatment of electron dynamics in finite quantum systems has been presented. MCTDHF and other numerical methods were used to investigate correlated multielectron dynamics. MCTDHF is a powerful tool for investigating multielectron dynamics in strong laser fields and opens the door to previously inaccessible calculations. We have developed an MCTDHF code that will allow us to handle many problems involving the multielectron dynamics of 3D atoms and molecules under the influence of a strong laser field. Throughout the development of this code, problems in lower dimensions were also treated.

It was shown how spin-based coded qubit operations in a 2D double quantum dot can be accelerated. The qubit subspace consisted of the lowest singlet and triplet state of a double Gaussian well. The speed-up of qubit operations is important for quantum computation because shorter manipulation times lead to less leakage into the environment. In addition, by manipulating a similar potential to that of the spin-based QD, it was shown how the transition matrix elements (TMEs) for the system can be controlled and thus the population of a two-level system can be frozen. For this two-level system the two lowest singlet states were used. These states have different charge configurations and thus present an opportunity for encoding a two-electron charge qubit. The control of the TME also presents the opportunity to control single-photon emission on demand.

Also investigated was the plasmon dynamics in a strongly driven QD containing four electrons. These calculations are unique in that they are the first non-perturbative calculations of electrons dynamics using more than two electrons for a system with more than a single dimension. In this case the system was tuned from the weakly correlated electron gas to the strongly correlated regime of Wigner crystallization. It was shown that the influence of correlation on the surface-induced plasmon decay is negligible. This implies that the Kohn theorem is extendible to finite QDs.

In addition, the quantum breathing mode (QBM) was investigate for QDs containing up to six electrons. An analytical expression for the QBM was derived. This expression was validated by comparison with MCTDHF calculations for the range from a weakly correlated electron gas to the limit of Wigner crystallization using QDs containing up to six electrons. It was shown that the behaviour of the QBM can provide a signature of a change in the angular momentum of the unperturbed ground state as the correlation is increased. Furthermore, the formalism developed to determine an expression for the QBM has the potential to be used to determine analytical expressions for higher order collective modes.

Nonsequential double ionization was also investigated for a 2D diatomic molecule. Distinct features in the two-electron momentum space were observed. With the help of a semiclassical

model, it was shown that these signatures correspond to specific ionic bound states involved in the ionization process. It was shown that specific higher excited ionic states provide an efficient channel for the second electron in the nonsequential double ionization process to escape. High harmonic generation was also studied for this system. The method of ionic eigenstate resolved wavefunctions was introduced and it was shown that a significant source of correlation is the polarization of the ion by the recombining electron.

A method for performing MCTDHF calculations in three dimensions using a nonuniform tensor product grid was developed. First tests of the nonuniform grid version of MCTDHF were done by performing relaxation calculations for small sodium clusters containing four and six electrons. This implementation of MCTDHF opens an avenue to investigate many problems that were previously inaccessible. Some problems to be considered include the complex ionization processes that occur in noble gas atoms, high harmonic generation in noble gas atoms and molecules, as well as, orbital rearrangement in molecules after ionization. Also to be investigated are the nonlinear effects observed by XFEL experiments on neon atoms.

Finally, an answer was provide for the time it takes for an electron to tunnel. The tunnel time was defined as the time it takes for the wavefunction to develop the under-barrier components necessary to reach the static ionization rate. This definition was then extended to a time varying field. It was shown that the tunnel time is proportional to the Keldysh time thus connecting the Keldysh time to the evolution of the wavefunction. Furthermore, an experimental method for measuring the tunnel time was proposed.

# Appendix A

# Density functional theory

Density functional theory (DFT) is built from the Hohenberg-Kohn (HK) theorem which states:

**Theorem A.0.1** (Hohenberg-Kohn Theorem)**.** *The external potential for a bound system of interacting electrons is uniquely determined, up to an additive constant, by the ground-state density [33].*

Since the kinetic energy $T$ and the Coulomb repulsion $V$ are universal, the Hamiltonian is uniquely determined by the external potential $U$. The HK theorem states that the density $\rho$ determines the Hamiltonian and hence implicitly determines all physical properties that can be obtained from it. The exact ground state density function is found using the HK variational principle which minimizes the energy functional,

$$E_U[\rho] = F[\rho] + \int U(\mathbf{r})\rho(\mathbf{r})d\mathbf{r} \tag{A.1}$$

with $F$ being the universal functional $F[\rho] = \langle\Psi|(T+V)|\Psi\rangle$. Minimization is done over all trial densities $\tilde{\rho}$, to determine the ground-state energy

$$E_g = \min_{\tilde{\rho}}\{E_U[\tilde{\rho}]\}. \tag{A.2}$$

In DFT a system of interacting particles takes on the form of a system of non-interacting particles in the presence of the effective potential

$$U_{\text{eff}} = U + \int \frac{\rho(\mathbf{r}')}{|\mathbf{r}-\mathbf{r}'|}d\mathbf{r}' + U_{\text{xc}} \tag{A.3}$$

where $U_{\text{xc}}$ is the local exchange-correlation potential. $U_{\text{xc}}$ is a functional of $\rho$ and takes account of exchange and correlation effects. The density can be determined by solving a set of one-body time-independent Schrödinger equations, known as the Kohn-Sham (KS) equations [172], given by

$$\left(-\frac{1}{2}\nabla^2 + U_{\text{eff}}\right)\varphi_i = E_i\varphi_i \tag{A.4}$$

where the density is determined from

$$\rho = \sum_i |\varphi_i|^2. \tag{A.5}$$

# Appendix B

# Filtering procedure for the tunnel time calculation

Here the filtering process used in Chap. 9 is discussed. The spectral filter $f(\epsilon)$ is given by,

$$f(\epsilon) = \begin{cases} 1 & \text{for } \epsilon < \epsilon_c \\ G(\epsilon) & \text{for } \epsilon \geq \epsilon_c \end{cases} \tag{B.1}$$

where $G(\epsilon)$ is a Gaussian centered at $\epsilon_c$ given by

$$G(\epsilon) = e^{(\epsilon-\epsilon_c)^2/2\sigma^2} \tag{B.2}$$

with $\sigma$ the width (standard deviation). This filter has two parameters that can be varied; $\sigma$ and $\epsilon_c$. We require $\epsilon_c$ to be a fixed distance $\delta$ from the peak $\epsilon_p$ of the spectral density for all field strengths; that is $\delta = \epsilon_c - \epsilon_p$. For the quantum dot we use $\delta = 0.005$; however, we note that $\delta$ can be chosen anywhere in the range $0 - 0.01$ and have little effect on the overall results. The atomic potential is treated in a similar manner.

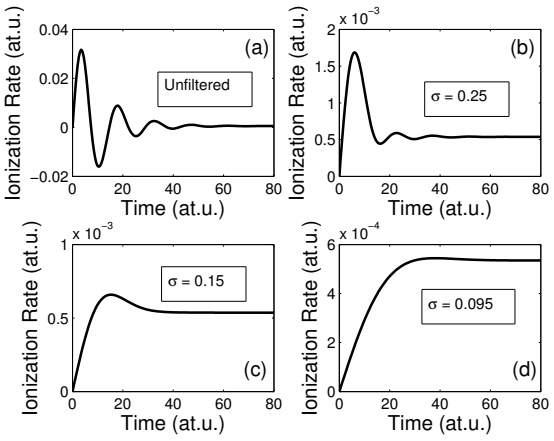


**Figure B.1.** Effect of the filter width on the ionization rate.

Fig. B.1 shows the effect of the varying the filter width $\sigma$ for $F = 0.08$; all other values of $F$ display a similar behaviour. In Fig. B.1(a) the unfiltered signal is shown; the oscillations result

from the excited state channel. As $\sigma$ is decreased the oscillations from the excited state channel signal begin to wane; see Figs. B.1(b) and (c). Once these oscillations disappear, the ionization rate monotonically approaches the static ionization rate $\mathrm{w}(F)$; only the tunneling signal remains (see Fig. B.1(d)).

The filter is then chosen by scanning the parameter space in order to find the $\sigma$ value for which the difference between the largest amplitude in the oscillation of the ionization rate and $\mathrm{w}(F)$ falls below a desired threshold — for our calculations we require the amplitude to be below 1% of $\mathrm{w}(F)$. The tunnel time is then taken to be the time at which the ionization rate is within 1% of $\mathrm{w}(F)$.

# Appendix C

# Glossary of Abbreviations

**BCH** — Bake-Campbell-Hausdorff

**CM** — Centre of mass

**DFT** — Density functional theory

**DQD** — Double quantum dot

**FC** — Frozen-core

**HHG** — High-harmonic generation

**HK** — Hohenberg-Kohn

**IER** — Ionic eigenstate resolved

**MCTDH** — Multiconfiguration time-dependent Hartree

**MCTDHF** — Multiconfiguration time-dependent Hartree-Fock

**NIR** — Near-infrared

**NSDI** — Nonsequential double ionization

**QBM** — Quantum breathing mode

**QD** — Quantum dot

**RG** — Runge-Gross

**SAE** — Single active electron

**SPO** — Split operator

**TDCI** — Time-dependent configuration interaction

**TDDFT** — Time-dependent density functional theory

**TDHF** — Time-dependent Hartree-Fock

**TDSE** — Time-dependent Schrödinger equation

**TISE** — Time-independent Schrödinger equation

**TME** — Transition matrix element

**XFEL** — X-ray free-electron laser

**XUV** — Extreme ultraviolet

# References


[1] F. H. L. Koppens *et al.* Driven coherent oscillations of a single electron spin in a quantum dot. *Nature*, 442:776, August 2006.

[2] T. D. Ladd, F. Jelezko, R. Laflamme, Y. Nakamura, C. Monroe, and J. L. OBrien. Quantum computers. *Nature*, 464:45–53, March 2010.

[3] H. Park. Nanomechanical oscillations in a single-C60 transistor. *Nature*, 407:57, 2000.

[4] J. Bylander, T. Duty, and P. Delsing. Current measurement by real-time counting of single electrons. *Nature*, 434:361, 2005.

[5] S. Tarucha, D. G. Austing, T. Honda, R. J. van der Hage, and L. P. Kouwenhoven. Shell filling and spin effects in a few electron quantum dot. *Phys. Rev. Lett.*, 77:3613–3616, Oct 1996.

[6] R. C. Ashoori. Electrons in artificial atoms. *Nature*, 46:413, Feb 1996.

[7] S. M. Reimann and M. Manninen. Electronic structure of quantum dots. *Rev. Mod. Phys.*, 74:1283–1342, Nov 2002.

[8] M. Hentschel *et al.* Attosecond metrology. *Nature*, 414:509, 2001.

[9] R. Kienberger *et al.* Steering attosecond electron wave packets with light. *Science*, 297:1144, 2002.

[10] M. Drescher *et al.* Time-resolved atomic inner-shell spectroscopy. *Nature*, 419:783, 2002.

[11] R. Kienberger *et al.* Atomic transient recorder. *Nature*, 427:817, 2004.

[12] E. Gouliemakis *et al. Science*, 305:1267, 2004.

[13] D. Zeidler, A. Staudte, A. B. Bardon, D. M. Villeneuve, R. Dörner, and P. B. Corkum. Controlling attosecond double ionization dynamics via molecular alignment. *Phys. Rev. Lett.*, 95:203003, Nov 2005.

[14] S. Baker *et al.* Probing proton dynamics in molecules on an attosecond time scale. *Science*, 312:424, 2006.

[15] M. Uiberacker *et al.* Attosecon real-time observation of electron tunnelling in atoms. *Nature*, 446:627, 2007.

[16] P. Eckle *et al.* Attosecond angular streaking. *Nat. Phys.*, 4:565, 2008.

[17] P. Eckle *et al.* Attosecond ionization and tunneling delay time measurements in helium. *Science*, 322:1525, 2008.

[18] C. I. Blaga. Strong-field photoionization revisited. *Nat. Phys.*, 5:335, 2012.

[19] H. J. Wörner, J. B. Bertrand, D. V. Kartashov, P. B. Corkum, and D. M. Villeneuve. Following a chemical reation using high-harmonic interferometry. *Nature*, 466:604, 2010.

[20] G. Doumy *et al.* Nonlinear atomic response to intense ultrashort x rays. *Phys. Rev. Lett.*, 106:083002, Feb 2011.

[21] D. Shafir *et al.* Resolving the time when an electron exits a tunnelling barrier. *Nature*, 484:343, 2012.

[22] K. C. Kulander. Time-dependent Hartree-Fock theory of multiphoton ionization: Helium. *Phys. Rev. A*, 36:2726–2738, Sep 1987.

[23] M. Horbatsch, H. J. Ludde, and R. M. Dreizler. Time-dependent variational approach for two-particle systems: photoionization of He ($1s^2$). *J. Phys. B*, 25:3315, 1992.

[24] J. Parker, K .T. Taylor, C. W. Clark, and S. Blodgett-Ford. Intense-field multiphoton ionization of a two-electron atom. *J. Phys. B*, 29:L33, 1996.

[25] K. J. Meharg J. S. Parker, B. J. S. Doherty and K. T. Taylor. Time delay between singly and doubly ionizing wavepackets in laser-driven helium. *J. Phys. B*, 36:L393, 2003.

[26] A. Saenz. Behavior of molecular hydrogen exposed to strong dc, ac, or low-frequency laser fields. I. Bond softening and enhanced ionization. *Phys. Rev. A*, 66:063407, Dec 2002.

[27] A. Saenz. Behavior of molecular hydrogen exposed to strong dc, ac, or low-frequency laser fields. II. Comparison of *ab initio* and Ammosov-Delone-Krainov rates. *Phys. Rev. A*, 66:063408, Dec 2002.

[28] A. Saenz. Electronically excited states of molecular hydrogen exposed to strong direct current, alternative current, or low-frequency laser fields. *J. Phys. B*, 35:4829, 2002.

[29] K. Harumiya, H. Kono, Y. Fujimura, I. Kawata, and A. D. Bandrauk. Intense laser-field ionization of $H_2$ enhanced by two-electron dynamics. *Phys. Rev. A*, 66:043403, Oct 2002.

[30] M. Awasthi and A. Saenz. Internuclear-distance dependence of ionization of $H_2$ in strong laser fields. *J. Phys. B*, 39:S389, 2006.

[31] E. Dehghanian, A. D. Bandrauk, and G. Lagmago Kamta. Enhanced ionization of the $H_2$ molecule driven by intense ultrashort laser pulses. *Phys. Rev. A*, 81:061403, Jun 2010.

[32] K. Gottfried and T. Yan. *Quantum Mechanics: Fundamentals*. Springer, 2nd edition, 2003.

[33] P. Hohenberg and W. Kohn. Inhomogeneous electron gas. *Phys. Rev.*, 136:B864–B871, Nov 1964.

[34] E. Runge and E. K. U. Gross. Density-functional theory for time-dependent systems. *Phys. Rev. Lett.*, 52:997–1000, Mar 1984.

[35] R. van Leeuwen. Mapping from densities to potentials in time-dependent density-functional theory. *Phys. Rev. Lett.*, 82:3863–3866, May 1999.

[36] A. Görling and M. Levy. Exact Kohn-Sham scheme based on perturbation theory. *Phys. Rev. A*, 50:196–204, Jul 1994.

[37] M. Seidl, J. P. Perdew, and S. Kurth. Simulation of all-order density-functional perturbation theory, using the second order and the strong-correlation limit. *Phys. Rev. Lett.*, 84:5070–5073, May 2000.

[38] M. Lein and S. Kümmel. Exact time-dependent exchange-correlation potentials for strong-field electron dynamics. *Phys. Rev. Lett.*, 94:143003, Apr 2005.

[39] P. Decleva M. Stener and A. Görling. The role of exchange and correlation in time-dependent density-functional theory for photoionization. *J. Chem. Phys.*, 114:7816, 2001.

[40] Z.-L. Cai, K. Sendt, and J. R. Reimers. Failure of density-functional theory and time-dependent density-functional theory for large extended $\pi$ systems. *J. Chem. Phys.*, 117:5543, 2002.

[41] N. T. Maitra, K. Burke, and C. Woodward. Memory in time-dependent density functional theory. *Phys. Rev. Lett.*, 89:023002, Jun 2002.

[42] J. Caillat, J. Zanghellini, M. Kitzler, O. Koch, W. Kreuzer, and A. Scrinzi. Correlated multielectron systems in strong laser fields: A multiconfiguration time-dependent Hartree-Fock approach. *Phys. Rev. A*, 71:012712, January 2005.

[43] A. D. McLachlan. A variational solution of the time-dependent Schrödinger equation. *Mol. Phys.*, 8:39–44, 1964.

[44] M.H. Beck, A. Jäckle, G.A. Worth, and H.-D. Meyer. The multiconfiguration time-dependent hartree (MCTDH) method: a highly efficient algorithm for propagating wavepackets. *Physics Reports*, 324(1):1 – 105, 2000.

[45] C. McDonald. *Master's Thesis: Quantum Dynamics of Multi-Electron Systems in Strong Laser Fields*. 2007.

[46] M. Frigo and S. G. Johnson. FFTW. `http://www.fftw.org/`.

[47] D. Kincaid and W. Cheney. *Numerical Analysis: Mathematics of Scientific Computing*. Brooks/Cole, 3rd edition, 2002.

[48] M. Beck *et al.* The Heidelberg MCTDH Package. `http://www.pci.uni-heidelberg.de/tc/usr/mctdh/doc/index.html`.

[49] M. H. Beck and H. D. Meyer. An efficient and robust integration scheme for the equations of motion of the multiconfiguration time-dependent Hartree (MCTDH) method. *Z. Phys. D*, 42:113, 1997.

[50] G. Burkard, D. Loss, and D. P. DiVincenzo. Coupled quantum dots as quantum gates. *Phys. Rev.*

*B*, 59:2070–2078, Jan 1999.

[51] I. A. Merkulov, A. L. Efros, and M. Rosen. Electron spin relaxation by nuclei in semiconductor quantum dots. *Phys. Rev. B*, 65:205309, Apr 2002.

[52] S. E. Sklarz and D. J. Tannor. Loading a Bose-Einstein condensate onto an optical lattice: An application of optimal control theory to the nonlinear Schrödinger equation. *Phys. Rev. A*, 66:053619, Nov 2002.

[53] J. Schliemann, D. Loss, and A. H. MacDonald. Double-occupancy errors, adiabaticity, and entanglement of spin qubits in quantum dots. *Phys. Rev. B*, 63:085311, Feb 2001.

[54] X. Hu and S. Das Sarma. Gate errors in solid-state quantum-computer architectures. *Phys. Rev. A*, 66:012312, Jul 2002.

[55] G. E. Murgida, D. A. Wisniacki, and P. I. Tamborenea. Coherent control of interacting electrons in quantum dots via navigation in the energy spectrum. *Phys. Rev. Lett.*, 99:036806, Jul 2007.

[56] J. H. Jefferson, M. Fearn, D. L. J. Tipton, T. P., and Spiller. Two-electron quantum dots as scalable qubits. *Phys. Rev. A*, 66:042328, Oct 2002.

[57] J. Zanhellini, M. Kitzler, T. Brabec, and A. Scrinzi. Testing the multi-configuration time-dependent Hartree-Fock method. *J. Phys. B: At. Mol. Opt. Phys.*, 37:763, January 2004.

[58] L. Sælen, R. Nepstad, I. Degani, and J. P. Hansen. Optical control in coupled two-electron quantum dots. *Phys. Rev. Lett.*, 100:046805, Feb 2008.

[59] D. Loss and D. P. DiVincenzo. Quantum computation with quantum dots. *Phys. Rev. A*, 57:120–126, Jan 1998.

[60] D. P. DiVincenzo, D. Bacon, J. Kempe, G. Burkard, and K. B. Whaley. Universal quantum computation with the exchange interaction. *Nature*, 408:339, November 2000.

[61] J. Levy. Universal quantum computation with spin-1/2 pairs and heisenberg exchange. *Phys. Rev. Lett.*, 89:147902, Sep 2002.

[62] M. Pioro-Ladrière, M. Ciorga, J. Lapointe, P. Zawadzki, M. Korkusi ński P., Hawrylak, and A. S. Sachrajda. Spin-blockade spectroscopy of a two-level artificial molecule. *Phys. Rev. Lett.*, 91:026803, Jul 2003.

[63] J. R. Petta, A. C. Johnson, J. M. Taylor, E. A. Laird, A. Yacoby, M. D. Lukin, C. M. Marcus, M. P. Hanson, and A. C. Gossard. Coherent manipulation of coupled electron spins in semiconductor quantum dots. *Science*, 309:2180, September 2005.

[64] L. Gaudreau, S. A. Studenikin, A. S. Sachrajda, P. Zawadzki, A. Kam, J. Lapointe, M. Korkusinski, and P. Hawrylak. Stability diagram of a few-electron triple dot. *Phys. Rev. Lett.*, 97:036807, Jul 2006.

[65] R. Hanson and G. Burkard. Universal set of quantum gates for double-dot spin qubits with fixed interdot coupling. *Phys. Rev. Lett.*, 98:050502, Jan 2007.

[66] A. D. Bandrauk and H. Shen. High-order split-step exponential methods for solving coupled nonlinear Schrödinger equations. *J. Phys. A: Math. Gen.*, 27:7147, July 1994.

[67] K. Saito and Y. Kayanuma. Nonadiabatic electron manipulation in quantum dot arrays. *Phys. Rev. B*, 70:201304(R), Nov 2004.

[68] A. Mitra, T. S. Mahesh, and A. Kumar. NMR implementation of adiabatic SAT algorithm using strongly modulated pulses. *J. Chem. Phys.*, 128:2180, March 2008.

[69] R. Hanson, L. P. Kouwenhoven, J. R. Petta, S. Tarucha, and L. M. K. Vandersypen. Spins in few-electron quantum dots. *Rev. Mod. Phys.*, 79:1217–1265, Oct 2007.

[70] T. Fujisawa, T. Hayashi, and S. Sasaki. Time-dependent single-electron transport through quantum dots. *Rep. Prog. Phys/*, 69:759, 2006.

[71] F. H. L. Koppens *et al.* Control and detection of singlet-triplet mixing in a random nuclear field. *Science*, 309:1346, August 2005.

[72] T. Hayashi, T. Fujisawa, H. D. Cheong, Y. H. Jeong, and Y. Hirayama. Coherent manipulation of electronic states in a double quantum dot. *Phys. Rev. Lett.*, 91:226804, Nov 2003.

[73] R. M. Abolfath, W. Dybalski, and P. Hawrylak. Theory of a two-level artificial molecule in laterally coupled quantum hall droplets. *Phys. Rev. B*, 73:075314, Feb 2006.

[74] D. V. Melnikov and J.-P. Leburton. Single-particle state mixing in two-electron double quantum

dots. *Phys. Rev. B*, 73:155301, Apr 2006.

[75] U. Bockelmann and G. Bastard. Phonon scattering and energy relaxation in two-, one-, and zero-dimensional electron gases. *Phys. Rev. B*, 42:8947–8951, Nov 1990.

[76] C. F. Destefani and Sergio E. Ulloa. Oscillatory spin relaxation rates in quantum dots. *Phys. Rev. B*, 72:115326, Sep 2005.

[77] J. I. Climente, A. Bertoni, G. Goldoni, and E. Molinari. Phonon-induced electron relaxation in weakly confined single and coupled quantum dots. *Phys. Rev. B*, 74:035313, Jul 2006.

[78] A. Bertoni, M. Rontani, G. Goldoni, F. Troiani, and E. Molinari. Field-controlled suppression of phonon-induced transitions in coupled quantum dots. *Appl. Phys. Lett.*, 85:4729, November 2004.

[79] P. Stano and J. Fabian. Theory of phonon-induced spin relaxation in laterally coupled quantum dots. *Phys. Rev. Lett.*, 96:186602, May 2006.

[80] L. Fedichkin and A. Fedorov. Error rate of a charge qubit coupled to an acoustic phonon reservoir. *Phys. Rev. A*, 69:032311, Mar 2004.

[81] A. Thränhardt, C. Ell, G. Khitrova, and H. M. Gibbs. Relation between dipole moment and radiative lifetime in interface fluctuation quantum dots. *Phys. Rev. B*, 65:035327, Jan 2002.

[82] U. Hohenester. Optimal quantum gates for semiconductor qubits. *Phys. Rev. B*, 74:161307(R), Oct 2006.

[83] J. Gorman, D. G. Hasko, and D. A. Williams. Charge-qubit operation of an isolated double quantum dot. *Phys. Rev. Lett.*, 95:090502, Aug 2005.

[84] V. N. Stavrou and X. Hu. Charge decoherence in laterally coupled quantum dots due to electron-phonon interactions. *Phys. Rev. B*, 72:075362, Aug 2005.

[85] D. Bacon, J. Kempe, D. A. Lidar, and K. B. Whaley. Universal fault-tolerant quantum computation on decoherence-free subspaces. *Phys. Rev. Lett.*, 85:1758–1761, Aug 2000.

[86] S. Debald, T. Brandes, and B. Kramer. Control of dephasing and phonon emission in coupled quantum dots. *Phys. Rev. B*, 66:041301, Jul 2002.

[87] Y. Takane and T. Murakami. Pulse control of dephasing in two-level quantum systems. *Journal of the Physical Society of Japan*, 74(8):2243–2248, 2005.

[88] M. Hentschel, D. C. B. Valente, E. R. Mucciolo, and H. U. Baranger. Improving intrinsic decoherence in multiple-quantum-dot charge qubits. *Phys. Rev. B*, 76:235309, Dec 2007.

[89] B. Lounis and M. Orrit. Single-photon sources. *Rep. Prog. Phys/*, 68:1129, 2005.

[90] Full configuration interaction approach to the few-electron problem in artificial atoms.

[91] R. M. Abolfath and P. Hawrylak. Real space Hartree-Fock configuration interaction method for complex lateral quantum dot molecules. *J. Chem. Phys.*, 125:034707, 2006.

[92] M. Koskinen, M. Manninen, and P. O. Lipas. Configuration-interaction calculations of jellium clusters by the nuclear shell model. *Phys. Rev. B*, 49:8418–8436, Mar 1994.

[93] A. V. Filinov, M. Bonitz, and Yu. E. Lozovik. Wigner crystallization in mesoscopic 2D electron systems. *Phys. Rev. Lett.*, 86:3851–3854, Apr 2001.

[94] A. D. Güçlü, Amit Ghosal, C. J. Umrigar, and Harold U. Baranger. Interaction-induced strong localization in quantum dots. *Phys. Rev. B*, 77:041301, Jan 2008.

[95] Spin-projected unrestricted hartree-fock ground states for harmonic quantum dots.

[96] B. Reusch and H. Grabert. Unrestricted Hartree-Fock for quantum dots. *Phys. Rev. B*, 68:045309, Jul 2003.

[97] C. Yannouleas and U. Landman. Group theoretical analysis of symmetry breaking in two-dimensional quantum dots. *Phys. Rev. B*, 68:035325, Jul 2003.

[98] M. Brack. The physics of simple metal clusters: self-consistent jellium model and semiclassical approaches. *Rev. Mod. Phys.*, 65:677–732, Jul 1993.

[99] C. F. Destefani, C. McDonald, S. Sukiasyan, and T. Brabec. Controlling transition matrix elements and relaxation in a two-electron double quantum dot. *Phys. Rev. B*, 79:155322, Apr 2009.

[100] C. F. Destefani, C. McDonald, R. M. Abolfath, P. Hawrylak, and T. Brabec. *Ab initio* approach to the optimization of qubit manipulation. *Phys. Rev. B*, 78:165331, Oct 2008.

[101] M. Santer, B. Mehlig, and M. Moseler. Optical response of two-dimensional electron fluids beyond

the Kohn regime: Strong nonparabolic confinement and intense laser light. *Phys. Rev. Lett.*, 89:286801, Dec 2002.

[102] S. Kalliakos *et al.* A molecular state of correlated electrons in a quantum dot. *Nat. Phys.*, 4:467, 2008.

[103] P. A. Maksym and Tapash Chakraborty. Quantum dots in a magnetic field: Role of electron-electron interactions. *Phys. Rev. Lett.*, 65:108–111, Jul 1990.

[104] P. Hawrylak, P. A. Schulz, and J. J. Palacios. *Solid State Commun.*, 93:909, 1995.

[105] H. Reinholz., R. Redmer, G. Röpke, and A. Wierling. Long-wavelength limit of the dynamical local-field factor and dynamical conductivity of a two-component plasma. *Phys. Rev. E*, 62:5648–5666, Oct 2000.

[106] H. Moritz, T. Stöferle, M. Köhl, and T. Esslinger. Exciting collective oscillations in a trapped 1D gas. *Phys. Rev. Lett.*, 91:250402, Dec 2003.

[107] S. Giorgini, L. P. Pitaevskii, and S. Stringari. Theory of ultracold atomic Fermi gases. *Rev. Mod. Phys.*, 80:1215–1274, Oct 2008.

[108] M. Bonitz, K. Balzer, and R. van Leeuwen. Invariance of the Kohn center-of-mass mode in a conserving theory. *Phys. Rev. B*, 76:045341, Jul 2007.

[109] Sh. Amiranashvili, M. Y. Yu, and L. Stenflo. Nonuniform non-neutral plasma in a trap. *Phys. Rev. E*, 67:016408, Jan 2003.

[110] V. A. Schweigert and F. M. Peeters. Spectral properties of classical two-dimensional clusters. *Phys. Rev. B*, 51:7700–7713, Mar 1995.

[111] S. A. Tatarkova, A. E. Carruthers, and K. Dholakia. One-dimensional optically bound arrays of microscopic particles. *Phys. Rev. Lett.*, 89:283901, Dec 2002.

[112] C. Henning, K. Fujioka, P. Ludwig, A. Piel, A. Melzer, and M. Bonitz. Existence and vanishing of the breathing mode in strongly correlated finite systems. *Phys. Rev. Lett.*, 101:045002, Jul 2008.

[113] A. Olivetti, J. Barré, B. Marcos, F. Bouchet, and R. Kaiser. Breathing mode for systems of interacting particles. *Phys. Rev. Lett.*, 103:224301, Nov 2009.

[114] I. Bloch. Ultracold quantum gases in optical lattices. *Nat. Phys.*, 1:23, 2005.

[115] D. Jaksch, C. Bruder, J. I. Cirac, C. W. Gardiner, and P. Zoller. Cold bosonic atoms in optical lattices. *Phys. Rev. Lett.*, 81:3108–3111, Oct 1998.

[116] A. Görlitz *et al.* Realization of Bose-Einstein condensates in lower dimensions. *Phys. Rev. Lett.*, 87:130402, Sep 2001.

[117] D. Rychtarik, B. Engeser, H.-C Nägerl, and R. Grimm. Two-dimensional bose-einstein condensate in an optical surface trap. *Phys. Rev. Lett.*, 92:173003, Apr 2004.

[118] S. Bauch, K. Balzer, C. Henning, and M. Bonitz. Quantum breathing mode of trapped bosons and fermions at arbitrary coupling. *Phys. Rev. B*, 80:054515, Aug 2009.

[119] J. W. Abraham, K. Balzer, D. Hochstuhl, and M. Bonitz. Quantum breathing mode of interacting particles in a one-dimensional harmonic trap. *Phys. Rev. B*, 86:125112, Sep 2012.

[120] A. L. Fetter and J. D. Walecka. *Quantum Theory of Many-Particle Systems.* Dover Publ., 2003.

[121] S. Stringari. Collective excitations of a trapped Bose-condensed gas. *Phys. Rev. Lett.*, 77:2360–2363, Sep 1996.

[122] C. Menotti and S. Stringari. Collective oscillations of a one-dimensional trapped Bose-Einstein gas. *Phys. Rev. A*, 66:043610, Oct 2002.

[123] B. L. Johnson, C. Barnes, and G. Kirczenow. Theory of the Hall effect in two-dimensional quantum-dot arrays. *Phys. Rev. B*, 46:15302–15308, Dec 1992.

[124] B. L. Johnson. Understanding the Laughlin wave function for the fractional quantum Hall effect. *Am. J. Phys.*, 70:401, 2002.

[125] H.-D. Meyer, U. Manthe, and L. S. Cederbaum. The multi-configurational time-dependent Hartree approach. *Chem. Phys. Lett.*, 165:73, 1990.

[126] M. R. Geller and G. Vignale. Quantum breathing mode for electrons with $1/r^2$ interaction. *Phys. Rev. B*, 53:6979–6980, Mar 1996.

[127] I. Strurzu. Taylor expansion for an operator function. 2004.

[128] L. Zeng, W. Geist, W. Y. Ruan, C. J. Umrigar, and M. Y. Chou. Path to Wigner localization in

circular quantum dots. *Phys. Rev. B*, 79:235334, Jun 2009.

[129] Th. Weber *et al.* Correlated electron emission in multiphoton double ionization. *Nature*, 405:658, 2000.

[130] A. Rudenko, K. Zrost, B. Feuerstein, V. L. B. de Jesus, C. D. Schröter, R. Moshammer, and J. Ullrich. Correlated multielectron dynamics in ultrafast laser pulse interactions with atoms. *Phys. Rev. Lett.*, 93:253001, Dec 2004.

[131] B. Walker, B. Sheehy, L. F. DiMauro, P. Agostini, K. J. Schafer, and K. C. Kulander. Precision measurement of strong field double ionization of helium. *Phys. Rev. Lett.*, 73:1227–1230, Aug 1994.

[132] X. Liu *et al.* Nonsequential double ionization at the single-optical-cycle limit. *Phys. Rev. Lett.*, 93:263001, Dec 2004.

[133] P. B. Corkum. Plasma perspective on strong field multiphoton ionization. *Phys. Rev. Lett.*, 71:1994–1997, Sep 1993.

[134] G. L. Yudin and M. Yu. Ivanov. Physics of correlated double ionization of atoms in intense laser fields: Quasistatic tunneling limit. *Phys. Rev. A*, 63:033404, Feb 2001.

[135] A. Becker and F. H. M. Faisal. Interpretation of momentum distribution of recoil ions from laser induced nonsequential double ionization. *Phys. Rev. Lett.*, 84:3546–3549, Apr 2000.

[136] C. Ruiz, L. Plaja, L. Roso, and A. Becker. *Ab initio* calculation of the double ionization of helium in a few-cycle laser pulse beyond the one-dimensional approximation. *Phys. Rev. Lett.*, 96:053001, Feb 2006.

[137] T. N. Rescigno, M. Baertschy, D. Byrum, and C. W. McCurdy. Making complex scaling work for long-range potentials. *Phys. Rev. A*, 55:4253–4262, Jun 1997.

[138] E. Schmidt. *Math. Ann.*, 63, 1907.

[139] M. Plummer and J. F. McCann. Field-ionization rates of the hydrogen molecular ion. *J. Phys. B*, 26:4625, 1996.

[140] H. C. Day, B. Piraux, and R. M. Potvliege. Multistate non-hermitian floquet dynamics in short laser pulses. *Phys. Rev. A*, 61:031402, Feb 2000.

[141] P. Agostini and L. F. DiMauro. The physics of attosecond light pulses. *Rep. Prog. Phys.*, 67:813, 2004.

[142] P. B. Corkum and F. Krauz. Attosecond science. *Nat. Phys.*, 3:381, Sep 2007.

[143] J. Itatani *et al. Nature*, 432:867, 2004.

[144] N. L. Wagner *et al.* Monitoring molecular dynamics using coherent electrons from high harmonic generation. *Proceedings of the National Academy of Sciences*, 103(36):13279–13285, 2006.

[145] S. Patchkovskii, Z. Zhao, T. Brabec, and D. M. Villeneuve. High harmonic generation and molecular orbital tomography in multielectron systems: Beyond the single active electron approximation. *Phys. Rev. Lett.*, 97:123003, Sep 2006.

[146] R. Santra and A. Gordon. Three-step model for high-harmonic generation in many-electron systems. *Phys. Rev. Lett.*, 96:073906, Feb 2006.

[147] Z. Zhao, J. Yuan, and T. Brabec. Multielectron signatures in the polarization of high-order harmonic radiation. *Phys. Rev. A*, 76:031404, Sep 2007.

[148] A. Gordon, F. X. Kärtner, N. Rohringer, and R. Santra. Role of many-electron dynamics in high harmonic generation. *Phys. Rev. Lett.*, 96:223902, Jun 2006.

[149] M. Plummer and C. J. Noble. Resonant enhancement of harmonic generation in argon at 248 nm. *J. Phys. B*, 35:L51, 2002.

[150] L. R. Moore J. S. Parker, D. H. Glass, E. S. Smyth, K. T. Taylor, and P. G. Burke. Time-dependent and time-independent methods applied to multiphoton ionization of helium. *J. Phys. B*, 36:L393, 2003.

[151] M. Lein *et al.* Role of the intramolecular phase in high-harmonic generation. *Phys. Rev. Lett.*, 88:183903, Apr 2002.

[152] K. C. Kulander and B. W. Shore. Calculations of multiple-harmonic conversion of 1064-nm radiation in Xe. *Phys. Rev. Lett.*, 62:524–526, Jan 1989.

[153] X. Chu and S. Chu. Time-dependent density-functional theory for molecular processes in strong

fields: Study of multiphoton processes and dynamical response of individual valence electrons of $N_2$ in intense laser fields. *Phys. Rev. A*, 64:063404, Nov 2001.

[154] G. Jordan and A. Scrinzi. Core-polarization effects in molecular high harmonic generation. *New J. Phys.*, 10:025035, 2008.

[155] W. C. Topp and J. J. Hopfield. Chemically motivated pseudopotential for sodium. *Phys. Rev. B*, 7:1295–1303, Feb 1973.

[156] I. A. Solov'yov, A. V. Solov'yov, and W. Greiner. Structure and properties of small sodium clusters. *Phys. Rev. A*, 65:053203, Apr 2002.

[157] I. Ovcharenko, A. Aspuru-Guzik, and Jr. W. A. Lester. Soft pseudopotentials for efficient quantum Monte Carlo calculations: From Be to Ne and Al to Ar. *The Journal of Chemical Physics*, 114(18):7790–7794, 2001.

[158] J. R. Trail and R. J. Needs. Norm-conserving Hartree–Fock pseudopotentials and their asymptotic behavior. *The Journal of Chemical Physics*, 122(1):014112, 2005.

[159] J. R. Trail and R. J. Needs. Smooth relativistic hartree–fock pseudopotentials for h to ba and lu to hg. *The Journal of Chemical Physics*, 122(17):174109, 2005.

[160] E. Merzbacher. The early history of quantum tunneling. *Physics Today*, 55(8):44–49, 2002.

[161] G. Binnig, H. Rohrer, Ch. Gerber, and E. Weibel. Surface studies by scanning tunneling microscopy. *Phys. Rev. Lett.*, 49:57–61, Jul 1982.

[162] L. Esaki. New phenomenon in narrow germanium $p - n$ junctions. *Phys. Rev.*, 109:603–604, Jan 1958.

[163] M. Meckel *et al.* Laser-induced electron tunneling and diffraction. *Science*, 320:1478, 2008.

[164] X. M. Tong, Z. X. Zhao, and C. D. Lin. Probing molecular dynamics at attosecond resolution with femtosecond laser pulses. *Phys. Rev. Lett.*, 91:233203, Dec 2003.

[165] R. Landauer and Th. Martin. Barrier interaction time in tunneling. *Rev. Mod. Phys.*, 66:217–228, Jan 1994.

[166] L. Arissian *et al.* Direct test of laser tunneling with electron momentum imaging. *Phys. Rev. Lett.*, 105:133002, Sep 2010.

[167] Y. Ban, E. Ya. Sherman, J. G. Muga, and M. Büttiker. Time scales of tunneling decay of a localized state. *Phys. Rev. A*, 82:062121, Dec 2010.

[168] L. V. Keldysh. Ionization in the field of a strong electromagnetic wave. *Sov. Phys. JETP*, 20:1307, 1965.

[169] V. S. Popov A. M. Perelomov and M. V. Terent'ev. Ionization of atoms in an alternating electric field. *Sov. Phys. JETP*, 23:924, 1966.

[170] M. V. Ammosov, N. B. Delone, and V. P. Krainov. Tunnel ionization of complex atoms and of atomic ions in an alternating electromagnetic field. *Sov. Phys. JETP*, 64:1191, 1986.

[171] U. Fano. Effects of configuration interaction on intensities and phase shifts. *Phys. Rev.*, 124:1866–1878, Dec 1961.

[172] W. Kohn and L. J. Sham. Self-consistent equations including exchange and correlation effects. *Phys. Rev.*, 140:A1133–A1138, Nov 1965.